Higher-Order Integral Equation Methods in Computational Electromagnetics

Jørgensen, Erik

Publication date:
2003

Document Version
Publisher's PDF, also known as Version of record

Higher-Order Integral Equation Methods in Computational Electromagnetics

Erik Jørgensen

May 2003

The present work was carried out at Ørsted-DTU in partial fulfillment of the requirements for the Ph.D. degree from the Technical University of Denmark.

Supervisors: Associate Professor Olav Breinbjerg, Ph.D.
Associate Professor Peter Meincke, Ph.D.

ISBN: 87-91184-21-5

Abstract

Higher-Order Integral Equation Methods in Computational Electromagnetics

Higher-order integral equation methods have been investigated. The study has focused on improving the accuracy and efficiency of the Method of Moments (MoM) applied to electromagnetic problems.

A new set of hierarchical Legendre basis functions of arbitrary order is developed. The new basis functions provide much better accuracy than low-order basis functions for a fixed number of functions. The hierarchical feature of the new basis functions combines the advantages of low- and higher-order basis functions into a single flexible set of functions. In comparison to existing higher-order basis functions, the new basis functions result in a much lower matrix condition number which is accomplished by focusing on the orthogonality of the basis functions. Numerical results confirm that higher-order convergence and very favorable condition numbers are achieved.

The low matrix condition number obtained with the new basis functions enables an efficient iterative solution of higher-order MoM systems. Iterative solution methods incorporate a matrix preconditioner and four preconditioners are presented here; two of these are found in existing works and the other two are adaptations of existing preconditioners to the higher-order case. Numerical experiments verify that the combination of the new basis functions, a good preconditioner, and a robust iterative algorithm lead to fast convergence even for very high-order basis functions, e.g. 10th order.

The new Legendre basis functions are further developed to incorporate edge singularities. Previous works in this area have shown the necessity of singular basis functions and three existing formulations are adapted to the new Legendre basis functions. Numerical experiments show that one formulation is the most accurate as well as the fastest to compute. Using this formulation, the accuracy of surface currents in the vicinity of edges is greatly improved and smaller improvements are obtained for the far field.

The hybrid Physical Optics (PO) - MoM is an efficient technique for treating objects that are too large in terms of wavelengths to be analyzed with MoM. The existing hybrid technique employs low-order basis functions and flat patches. This technique is extended here to the case of higher-order hierarchical Legendre basis functions and curved patches. The required memory and the computation time of the new higher-order hybrid PO-MoM are typically reduced by a factor of 10 in comparison to the existing technique. The hybrid technique includes the coupling between the MoM and PO regions and numerical results are presented to illustrate the accuracy.

The hierarchical feature of the new higher-order Legendre basis functions allows a flexible selection of the expansion order. This is demonstrated by numerical examples involving patches of non-uniform size. The expansion order is adapted to the electrical size of each patch which results in a very efficient solution.

Resumé (in Danish)
Højere-ordens integralligningsmetoder i numerisk feltteori

Højere-ordens integralligningsmetoder er blevet undersøgt. Studiet har fokuseret på at forbedre nøjagtigheden og effektiviteten af momentmetoden anvendt på elektromagnetiske feltberegninger.

Et nyt sæt af hierarkiske Legendre-basisfunktioner af vilkårlig orden udvikles. De nye basisfunktioner giver langt større nøjagtighed end basisfunktioner af lav orden for et fastholdt antal funktioner. Den hierarkiske opbygning af de nye basisfunktioner kombinerer fordelene ved lav- og højere-ordens funktioner i et enkelt fleksibelt sæt af basisfunktioner. I sammenligning med andre højere-ordens basisfunktioner resulterer de nye basisfunktioner i et langt lavere konditionstal af momentmatricen, hvilket er opnået ved at fokusere på basisfunktionernes ortogonalitet. Numeriske resultater bekræfter, at der opnås højere-ordens konvergens og meget favorable konditionstal.

Det lave konditionstal af matricen gør det muligt at løse højere-ordens momentmetode-systemer med en effektiv iterativ ligningsløser. Iterative løsningsmetoder involverer prækonditionering af matricen og der præsenteres fire metoder til prækonditionering; to af disse metoder kan findes i eksisterende litteratur mens de to andre er eksisterende metoder der tilpasses specielt til højere-ordens basisfunktioner. Numeriske resultater bekræfter at kombinationen af de nye basisfunktioner, en god metode til prækonditionering, samt en robust iterativ algoritme fører til hurtig konvergens, selv når basisfunktioner af meget høj orden anvendes, f.eks. 10.

De nye Legendre basisfunktioner udvikles yderligere for at tage hensyn til kantsingulariteter. Tidligere arbejde på dette område har påvist nødvendigheden af singulære basisfunktioner og tre eksisterende formuleringer tilpasses de nye Legendre-basisfunktioner. Eksperimenter viser, at en af disse formuleringer både er den mest nøjagtige og den hurtigste at beregne. Når denne formulering anvendes, forbedres nøjagtigheden af overfladestrømme i omegnen af kanter betragteligt og mindre forbedringer opnås for fjernfelter.

Den hybride fysisk optik/momentmetode er en effektiv teknik til objekter, der er så store i forhold til bølgelængden, at de ikke kan behandles med momentmetoden. Den eksisterende teknik anvender basisfunktioner af lav orden og plane overfladeelementer. Denne teknik udvides her til højere-ordens hierarkiske basisfunktioner og krumme overfladeelementer. Den nødvendige computerhukommelse og beregningstid reduceres typisk med en faktor 10 i forhold til den eksisterende teknik. Den hybride teknik medtager koblingen imellem områderne der behandles med momentmetoden og fysisk optik, og numeriske resultater præsenteres for at illustrere nøjagtigheden.

Den hierarkiske opbygning af de nye Legendre-basisfunktioner muliggør et fleksibelt valg af udviklingsorden. Dette demonstreres med numeriske eksempler der omfatter overfladeelementer af meget uens størrelse. Udviklingsordenen tilpasses til den elektriske størrelse af hvert overfladeelement, hvilket resulterer i en meget effektiv løsning.

Preface

The work presented in this thesis was carried out at Section for Electromagnetic Systems, Ørsted·DTU, Technical University of Denmark (DTU). The study was initiated in April 2000 and finalized in March 2003. Starting from July 2001, I spent 7th months as a visiting scholar at the Radiation Laboratory, University of Michigan, Ann Arbor, Michigan.

There is a number of people to whom I wish to extend my gratitude. First and foremost, my supervisors at DTU, Olav Breinbjerg and Peter Meincke, deserve as much credit for this work as I do. My interest in electromagnetics was created by Olav's inspiring attitude seven years ago and the continuous support and encouragement from both Peter and Olav have been an important source of motivation ever since. Next, the numerous discussions I have enjoyed with Oleksiy S. Kim, DTU, have been invaluable. Our corporation proves that the outcome of two people working together can be greater than the individual contributions. A number of other people have contributed to this work by providing reference results or valuable feedback. From DTU, Giacomo Benelli, Mirza Karamehmedovic, Hans-Rudolph Lenler-Eriksen, and Sergey Pivnenko, and from TICRA, Aksel Frandsen and Hans-Henrik Viskum.

I thank professor John Volakis for inviting me to Ann Arbor, Michigan, and giving me the chance to work with him and his large group of gifted people at the Radiation Laboratory. Professor Volakis received me with great hospitality and has certainly pushed me towards new goals. I wish to thank all the people working at the VCC in the fall of 2001 for making my stay a very pleasant experience. On the electromagnetic level, my discussions with Michael Carr and Kubilay Sertel were particularly awarding.

The work presented in this thesis was funded by DTU. However, I have received travel support from the Valdemar Selmer Trane Foundation, the TICRA foundation, and the Knud Højgaard foundation. Their generous support allowed me to travel frequently and exchange information with other researchers. And equally important, it made everything a little more fun.

Finally, I thank my friends and family for constantly reminding me that there is a life beyond electromagnetics.

Erik Jørgensen, May 2003.

Contents

Chapter 1
Introduction

Computational electromagnetics (CEM) is aimed at solving Maxwell's equations on a computer. Such solutions are required in many engineering applications, including but not limited to antenna analysis and synthesis, analysis of electromagnetic interference and compatibility, and design of high-frequency circuitry. Despite the rapid growth in computer speed there is a demand for more efficient and accurate methods providing solutions to problems that are beyond our present capabilities. One very popular method is the Method of Moments (MoM) which constitutes the core of many commercially available software packages. The MoM is essentially a discretization scheme for frequency-domain integral equations and during the last decade higher-order discretization schemes have attracted much attention since they have the potential of increasing both solution accuracy and efficiency. This ph.d. thesis presents improvements and new developments in this area.

The MoM gained widespread acceptance in the CEM community through the work of Harrington [1]. He described how to expand an unknown quantity appearing inside an integral in terms of N known basis functions and how to obtain a matrix equation by forcing the inner products of a residual function and N testing functions to be zero. The solution to the matrix equation provides weight coefficients for the basis functions which yield an approximation of the unknown quantity. The $N \times N$ system matrix represents the mutual interactions of all basis functions and is generally a full matrix with all non-zero elements. The size of this matrix is governed by the electrical size of the object under consideration, the desired accuracy, and the choice of basis functions. This latter choice is therefore a crucial factor in the MoM.

Basis functions that provide a piecewise linear expansion of a vector quantity were presented for quadrilateral domains by Glisson and Wilton [2] and for triangular domains by Rao *et al.* [3]. These basis functions have been quite successful and today, more than 20 years after their introduction, they are still the most commonly encountered basis functions in the MoM for three-dimensional (3-D) electromagnetic problems. However, the piecewise linear expansion generally requires many basis functions to achieve the desired accuracy. This has motivated the development of vector basis functions based on piecewise polynomial expansions of orders higher than one. Although the idea of piecewise polynomial expansions was devised much earlier, e.g. in the work of Harrington [1], higher-order vector basis functions were first applied in the Finite Element Method (FEM) in the early eighties [4] and made their way

into MoM applications during the early nineties. Significant works from this period include those of Wandzura [5], Kolundžija and Popović [6], Graglia *et al.* [7], and several other authors [8]-[14]. The various higher-order basis functions proposed in those works were all successful in the sense that they required significantly fewer unknowns to achieve a certain accuracy than the low-order piecewise linear basis functions.

Despite the reduced number of unknowns enabled by higher-order basis functions, conventional low-order basis function are still preferred in many applications. Three key problems can be identified to explain this. First, higher-order basis functions are often hard to implement and involve complicated expressions that are time-consuming to evaluate, e.g. those of [5]. Secondly, higher-order basis functions are often limited to a fixed expansion order on all subdomains in the computational region, e.g. those of [7]. This lack of flexibility is a significant drawback if the problem at hand comprises small geometrical features. Thirdly, higher-order basis functions often lead to a dense MoM matrix with a poor condition number, e.g. those of [6]. This proves to be a major disadvantage if an iterative solution of the matrix system is pursued. The higher-order basis functions presented in [5]-[13] suffer from at least one of these three key problems. For this reason, the majority of works on higher-order basis functions only apply basis functions up to third order and do not fully exploit the potential of the higher-order expansion.

The series of works by Kolundžija, Popović, Notaroš, and coworkers [6], [8], [11], [13], [15]-[18], applied basis functions of orders higher than three but the matrix equations were always solved by a direct method. The computation time involved in a direct solution method is proportional to N^3 which becomes prohibitively large when N is large. For comparison, the computation time of iterative methods or accelerated iterative methods [19] is proportional to N^2 or $N\log(N)$, respectively. Consequently, there appears to be a gap between the use of basis functions of orders higher than three and the use of an efficient iterative solution method. The difficulties arising for such cases were demonstrated by Kolundžija and Sarkar [20] that found little or no advantage by using an iterative solver with higher-order MoM systems. On the other hand, iterative solution methods have been used extensively with low-order basis functions. Early works applied conjugate-gradient type solvers, e.g. those of Sarkar *et al.* [21, 22] and Peterson and Mittra [23]. During the nineties, more robust iterative solvers of the Krylov subspace type [24] were developed and found their way into MoM applications. Also, the use of preconditioning techniques [24] has become an essential part of MoM implementations. Nevertheless, there is a lack of works dealing specifically with preconditioners and iterative solvers in conjunction with higher-order basis functions.

A particular challenging problem in the MoM is the treatment of objects with edges. The electromagnetic fields and currents can be singular in the vicinity of edges which has been discussed by many authors, e.g. Van Bladel [25]. This has motivated development of singular basis functions for MoM that include the edge effects. Significant works in this area include those of Andersson [26, 27], and Wilton and Govind [28]. Two types of singular higher-order basis functions were considered by Kolundžija [29] but the first type did not include the full edge behaviour and the second

type was apparently not implemented. Graglia and Lombardi [30] formulated singular higher-order basis functions for both FEM and MoM but they were not applied to MoM problems.

For electrically large objects the MoM imposes prohibitively heavy computational requirements. On the other hand, approximate high-frequency methods, such as physical optics (PO), are characterized by low computational requirements and improve their accuracy as the electrical size of the object increases. This has motivated several authors to consider hybrid PO-MoM techniques that combine the desirable features of both methods into a single powerful method. The most successful of these hybrid PO-MoM techniques was proposed by Jakobus and Landstorfer [31, 32]. The crucial step in their approach was to expand both MoM and PO currents in terms of MoM basis functions. The basis functions applied in [31, 32] and several subsequent works were the low-order basis functions proposed by Rao *et al.* [3]. To the knowledge of the author, the extension of the hybrid PO-MoM technique to the more efficient higher-order basis functions cannot be found in the literature.

The primary objective of this work is to formulate new higher-order basis functions for MoM that have all the advantages of the existing higher-order basis functions and none of their disadvantages. This will facilitate the use of high expansion orders, e.g. 10, in conjunction with iterative solvers. Next, the existing iterative solvers and preconditioning techniques should be investigated, and possibly extended, to allow an efficient solution of higher-order MoM systems. Further, the edge singularity problem should be investigated and the edge behaviour incorporated into the new basis functions. The existing hybrid PO-MoM method must be extended to the higher-order case to allow treatment of electrically large objects that cannot be treated with MoM alone. Finally, the developed techniques should be applicable to practical problems involving small geometrical features as well as large smooth regions, curved surfaces and curved wires, wire-surface junctions, and complex media.

This thesis is organized as follows. Chapter 2 presents an overview of various methods used in CEM. Further, the derivation of integral equations and their basic properties are discussed. An introduction to MoM is given and two special cases, the method of least squares and the Galerkin method, are considered. The choice of basis functions is discussed and the important role played by the matrix condition number is emphasized. This also involves a discussion on orthogonality of basis functions. The Chapters 3-6 constitute the main body of this work. Each of these four chapters contains a survey of existing works, some new developments or adaptation of existing techniques, and numerical results. Chapter 3 presents the development of a new set of higher-order basis functions. These functions are of the so-called hierarchical type which implies that a flexible selection of the expansion order is possible. The basis functions are based on orthogonal Legendre polynomials that are modified to allow the normal continuity of currents to be enforced while maintaining almost perfect orthogonality. This is accomplished without sacrificing the basic simplicity, thus leaving the basis functions easy to implement for arbitrary orders. Numerical comparisons with existing formulations are presented to demonstrate that improved condition numbers are obtained with the new basis functions. Chapter 4 deals with iterative solution of

higher-order MoM systems. Four different preconditioners and two iterative solvers are considered. The preconditioners are tailored to the higher-order basis functions and their performance evaluated for various expansion orders. Chapter 5 addresses the edge singularity problem by adapting three existing kinds of singular higher-order basis functions to the new basis functions developed in Chapter 3. The performance of these three types of singular basis functions is evaluated by considering the accuracy of surface currents and far fields. Chapter 6 extends the existing hybrid PO-MoM technique to the case of higher-order basis functions. Specifically, this extension involves the derivation of a projection operator which is particularly simple when the basis functions developed in Chapter 3 are used. The numerical results presented in Chapters 3-6 involve simple geometrical objects that are well-suited to illustrate various aspects of the methods. In contrast, Chapter 7 presents two more complicated applications where the expansion order is selected adaptively. The first example involves both large smooth regions and small geometrical features and the second example involves an object protruding the interface between two dielectric half spaces. Finally, Chapter 8 presents the conclusions of the thesis. It is noted that some of the work presented here has been or will be published in [33]-[42].

Chapter 2
Basic Theory of Integral Equations in Computational Electromagnetics

2.1 Overview of Computational Electromagnetics

There is a variety of methods aimed at obtaining numerical solutions to Maxwell's equations and the following discussion is not attempting to be complete. It is merely intended to place integral equation techniques and the MoM in a bigger framework. Sections 2.1.1 and 2.1.2 outline techniques based on differential and integral equations, respectively. Section 2.1.3 then deals with techniques that fall outside these two categories.

2.1.1 Differential Equation Techniques

The differential form of Maxwell's equations are point relations that must be satisfied by the electromagnetic field at every point in space. The first step of a numerical technique based on these equations is therefore to divide the configuration and the surrounding space into a number of small pieces or cells.

One of the most common frequency-domain techniques is the finite element method (FEM) [43] where each cell is referred to as an element. The electric or magnetic field is expanded in terms of N basis functions and a matrix equation is derived by minimizing a quadratic functional or introducing a set of testing function and forcing the residual to be orthogonal to the testing functions. Each basis function interacts only with its immediate neighbors which produces a sparse matrix with few non-zero elements outside the diagonal. The memory needed to store the matrix scales with the problem size as $O(N)$ and the solution to the matrix system is usually obtained with an iterative method.

A very popular technique for time-domain problems is the finite-difference time domain (FDTD) [44] method in which a finite-difference approximation of the space- and time-derivatives appearing in Maxwell's differential equations is employed directly. The field is then found by stepping in time and space until the steady state solution is obtained or until the desired time interval has passed. The method is matrix-free and meshless since only the field values at a regular grid need to be stored. This fact and its simple implementation are the primary reasons for its popularity. The transmission line method (TLM) [45] is similar to the FDTD method except that Maxwell's

equations are not used directly. Instead, the nodes of a regular grid are connected by virtual transmission lines. The fields then propagate through these transmission lines at each time step.

The main advantage of FEM, FDTD, TLM, and other differential-equation based methods is their ability to handle arbitrary, inhomogeneous, and non-linear materials. This ability stems from the fact that every point in space needs to be discretized which at the same time constitutes the main drawback of these methods. If the configuration includes homogeneous regions, or even worse an open region, these methods may require excessive memory and computation time. Open region problems can be treated with absorbing boundary conditions or perfectly matched layers which terminate the computational region but might also be a source of errors. Other important issues are numerical dispersion and stability since the field propagates from cell to cell and solutions may diverge.

2.1.2 Integral Equation Techniques

Integral equation techniques solve for the sources of an electromagnetic field rather than the field itself. The starting point is therefore to obtain a source-field relationship in the form of an integro-differential operator working on the source terms. The integral equation is then obtained by enforcing the appropriate boundary conditions and a discretization scheme is invoked to solve the equation.

The MoM [1] is the most popular discretization scheme. The unknown source term is expanded in terms of N known basis function. A matrix system is then obtained by choosing N testing functions and forcing the residual to be orthogonal to the testing functions. All basis functions interacts with all other basis functions and the matrix produced by MoM is therefore a full matrix. The memory needed to store this matrix scales as $O(N^2)$ and the CPU time as $O(N^3)$ or $O(N^2)$ with a direct or an iterative equation solver, respectively. The MoM is particularly advantageous for configurations involving homogeneous regions and open regions since only the boundaries need to be discretized. However, MoM is also used to solve volume integral equations for inhomogeneous regions.

The Nyström method is another discretization scheme for integral equations [46]. It does not require any basis function but employs a quadrature rule (see Appendix C.4) to approximate all integrals directly. The basic Nyström method cannot handle singular integral kernels as those encountered in electromagnetics which is remedied by locally correcting the quadrature rule to incorporate the singular nature of the kernel [47]. The memory and CPU time scale as that of MoM. A further discussion of the Nyström method will be given in Section 2.3.4

In recent years, the multilevel fast multipole method (MLFMM) [19] has been introduced to enhance the MoM or Nyström schemes. These latter schemes allow all source terms to interact with all other source terms. In the MLFMM the far-zone interactions are gathered in groups and computed on a group-group level. Once these group interactions are determined the contributions to the individual source terms can be found. The memory requirement and CPU time scale as $O(N \log(N))$ which has

given MLFMM and similar methods the name *fast methods*. However, computing the interactions on a group-group level is an approximation, albeit an acceptable and error-controlable one. Also, the lower computational complexity of $O(N\log(N))$ does not guarantee that the method requires less memory and CPU time than required by a conventional MoM scheme. There is a certain overhead associated with MLFMM and the configuration needs to be large before this overhead is worth while. An example of this will be given in Section 7.2.

2.1.3 Other Techniques

Many techniques cannot be categorized as differential- or integral-equation based. A few of these are mentioned below.

The generalized multipole technique (GMT) [48] is based on the method of weighted residuals (like the MoM). The unknown field is expanded in terms of a set of analytical field solutions originating from sources located away from the boundary of an object. These analytical solutions act as basis functions for the field and yield a smooth representation on the boundary of the object. GMT is similar to the method of auxiliary sources (MAS) [49] and these two techniques share advantages as well as weaknesses. They are easy to implement and the matrix fill time is short since no integrations are required. However, singular fields in vicinity of edges cause problems, the number of unknowns is usually larger than required by MoM, and the matrix equation might be ill-conditioned. These techniques are not as mature as MoM, FEM, and FDTD and the above-mentioned problems are hopefully addressed in the future.

A whole family of techniques is based on asymptotic solutions to Maxwell's equations in the high-frequency limit [50]. Physical optics (PO) yields an approximate induced current by using a tangent-plane approximation. The field is then found by using these currents in a radiation integral. The stationary-phase evaluation of this radiation integral yields the geometrical optics (GO) field. The field diffracted from edges can be included by using the physical theory of diffraction (PTD) which requires a line integration along the edges of the object. The stationary-phase evaluation of this line integral, together with the end-point contribution of the PO radiation integral, yield the field provided by the geometrical theory of diffraction (GTD). PTD and GTD require that the solution to a suitable canonical problem can be found. The advantage of the asymptotic methods is their ability to handle electrically large objects. However, they are approximate techniques and less general than differential- or integral-equation based methods.

Many researchers have considered hybrid methods combining the salient features of two methods into a single powerful method. A typical example is the finite element - boundary integral (FE-BI) [43] method that combines differential- and integral-equation based methods. The hybrid surface-volume integral equation method has essentially the same capability of modeling both inhomogeneous media and open region problems. A recent study found that the MoM applied to a volume integral equation is more accurate and more efficient than the FE-BI method for this type of problems [51]. For electrically large objects, asymptotic techniques can be hybridized with

differential- or integral-equation based methods (e.g., the hybrid PO-MoM presented in Chapter 6).

2.1.4 Discussion

It is clear from the discussion above that there is no ultimate method capable of solving all electromagnetic problems. The optimal choice of method for a given problem is governed by many factors such as accuracy requirements, ease of implementation, and available computer resources. In the opinion of this author, integral-equation based techniques are always preferable over differential-equation based techniques. However, if the geometry is too complicated to be handled by the integral-equation method, one may resort to a differential-equation based method. Asymptotic methods can be invoked if the object is too large in terms of wavelengths. If asymptotic methods are not accurate enough or cannot be applied to some specific parts of the object, an integral-equation based method can be included to form a hybrid method.

2.2 Integral Equations

Integral equations for electromagnetic problems can be derived in many ways and there are often more than one equation governing the same problem. The following treatment is therefore not a complete treatment but rather an illustration of some basic principles and some often encountered integral equations. The material presented below can be found in many works, e.g., that of Peterson *et al.* [52].

2.2.1 Source - Field Relationships

Integral equations are derived by establishing a relationship between a source term and the field radiated by this source. In this context the source is not necessarily a physical source but may be a mathematically equivalent source. The fields radiated by the electric current density $\mathbf{J}$ and the magnetic current density $\mathbf{M}$ in a homogeneous medium are conveniently described by the magnetic vector potential $\mathbf{A}$ and the electric vector potential $\mathbf{F}$. These are expressed as[1]

$$\mathbf{A}(\mathbf{r}) = \mu \int_V \mathbf{J}(\mathbf{r}')G(\mathbf{r},\mathbf{r}')\,dV', \tag{2.1a}$$

$$\mathbf{F}(\mathbf{r}) = \epsilon \int_V \mathbf{M}(\mathbf{r}')G(\mathbf{r},\mathbf{r}')\,dV', \tag{2.1b}$$

where V is a given volume, ϵ and μ are the permittivity and permeability of the homogeneous medium, and $G(\mathbf{r},\mathbf{r}')$ is the 3-dimensional scalar Green's function

$$G(\mathbf{r},\mathbf{r}') = \frac{e^{-jk|\mathbf{r}-\mathbf{r}'|}}{4\pi|\mathbf{r}-\mathbf{r}'|} \tag{2.2}$$

[1]Here and throughout the thesis, vectors are written in boldface, e.g. $\mathbf{a}$, and unit vectors as $\hat{\mathbf{a}} = \mathbf{a}/|\mathbf{a}|$. Matrices are written in boldface with a bar, e.g. $\bar{\mathbf{b}}$.

where $k = \omega\sqrt{\mu\epsilon}$ is the wavenumber and ω is the fixed angular frequency of the problem. An $e^{j\omega t}$ time-dependence is assumed and suppressed here and throughout the thesis. Primed coordinates are used for points in the source region, $\mathbf{r}'$, and unprimed coordinates for the point of observation, $\mathbf{r}$. If $\mathbf{J}$ and $\mathbf{M}$ are confined to a surface S, the magnetic and electric vector potentials are

$$\mathbf{A}(\mathbf{r}) = \mu \int_S \mathbf{J}_s(\mathbf{r}')G(\mathbf{r},\mathbf{r}')\,dS', \tag{2.3a}$$

$$\mathbf{F}(\mathbf{r}) = \epsilon \int_S \mathbf{M}_s(\mathbf{r}')G(\mathbf{r},\mathbf{r}')\,dS', \tag{2.3b}$$

where $\mathbf{J}_s$ and $\mathbf{M}_s$ are the electric and magnetic surface current densities, respectively. The electric and magnetic fields are then expressed as

$$\mathbf{E}^s = -j\omega\mathbf{A} - \frac{j\omega}{k^2}\nabla(\nabla\cdot\mathbf{A}) - \frac{1}{\epsilon}\nabla\times\mathbf{F} \tag{2.4a}$$

$$\mathbf{H}^s = -j\omega\mathbf{F} - \frac{j\omega}{k^2}\nabla(\nabla\cdot\mathbf{F}) + \frac{1}{\mu}\nabla\times\mathbf{A}\,. \tag{2.4b}$$

Another useful representation is the mixed-potential form in which both vector and scalar potentials are used. The electric field can be written as

$$\mathbf{E}^s = -j\omega\mathbf{A} - \nabla\Phi - \frac{1}{\epsilon}\nabla\times\mathbf{F} \tag{2.5}$$

where the scalar potential Φ is

$$\Phi(\mathbf{r}) = \frac{1}{\epsilon}\int_S \rho_s(\mathbf{r}')G(\mathbf{r},\mathbf{r}')\,dS', \tag{2.6}$$

in which ρ_s is the electric surface charge density.

2.2.2 Establishing an Integral Equation

The source-field relationships given in the previous section are valid in a homogeneous medium. This requirement is not satisfied for a practical problem where a physical object is present. The derivation of an integral equation therefore begins with the application of an appropriate equivalence principle. This allows the problem to be reduced to that of sources radiating in a homogeneous medium and the integral equation is then derived by enforcing the appropriate boundary conditions. Two distinct cases are given below to illustrate this general principle.

First, assume that an inhomogeneous dielectric object is present in free space and excited by an incident field $\mathbf{E}^i$. The object is characterized by the relative permittivity $\epsilon = \epsilon_r\epsilon_0$ and the relative permeability $\mu = \mu_0$. The object can then be replaced by the equivalent induced polarization currents

$$\mathbf{J} = j\omega\epsilon_0(\epsilon_r - 1)\mathbf{E}\,, \qquad \mathbf{M} = 0. \tag{2.7}$$

This is known as the volumetric equivalence principle. The sources $\mathbf{J}$ and $\mathbf{M}$ radiate in a homogeneous medium and the expressions in Section 2.2.1 are valid. Note that the term "source" should be interpreted in a general way. The source in (2.7) is actually the electric field. An integral equation can now be derived by requiring the total electric field to equal the sum of $\mathbf{E}^i$ and the field radiated by the equivalent sources given in (2.7). This leads to

$$\begin{aligned}\mathbf{E}(\mathbf{r}) = \mathbf{E}^i(\mathbf{r}) + k_0^2 \int_V (\epsilon_r - 1)\mathbf{E}(\mathbf{r}')G(\mathbf{r},\mathbf{r}')\,dV' \\ + \nabla\left(\nabla\cdot\int_V (\epsilon_r - 1)\mathbf{E}(\mathbf{r}')G(\mathbf{r},\mathbf{r}')\,dV'\right),\end{aligned} \tag{2.8}$$

where $k_0 = \omega\sqrt{\epsilon_0\mu_0}$. This equation is the volumetric EFIE with $\mathbf{E}$ as the only unknown. The discretization scheme employed to solve (2.8) should impose tangential continuity of $\mathbf{E}$ between adjacent cells. However, it often leads to a simpler implementation if (2.8) is formulated in terms of the electric flux density $\mathbf{D} = \epsilon\mathbf{E}$ which allows normal continuity to be imposed. Also, Volakis [53] formulated an alternative EFIE for the more general case of both non-trivial permittivity and permeability. Nevertheless, the electric field was still the only unknown.

Next, assume that a homogeneous object is present in free space and excited by the incident field $\mathbf{E}^i$. The permittivity and permeability of the object are ϵ_1 and μ_1, respectively. The total unknown fields are $\mathbf{E}$ and $\mathbf{H}$. The surface equivalence principle can then be used to establish an equivalent problem where $\mathbf{E}$ and $\mathbf{H}$ are unchanged outside the object but zero inside. The discontinuity of the fields must then be offset by placing equivalent electric and magnetic surface currents on the surface of the object. These equivalent surface currents are

$$\mathbf{J}_s = \hat{\mathbf{n}}\times\mathbf{H}\,, \qquad \mathbf{M}_s = -\hat{\mathbf{n}}\times\mathbf{E}\,, \tag{2.9}$$

where $\hat{\mathbf{n}}$ is an outward unit normal. Since the fields are zero inside the object, the object can be removed and replaced by free space. The sources in (2.9) then radiate in a homogeneous medium and the expressions in Section 2.2.1 are valid. The situation is then reversed and an equivalent problem with the total unknown fields $\mathbf{E}$ and $\mathbf{H}$ inside and zero field outside is established. This again requires equivalent surface currents to be placed on the surface of the object. These currents are the same as those in (2.9) except that the inward normal is used. Since the field is zero outside, the free-space region can be filled with a material characterized by ϵ_1 and μ_1. The equivalent currents then radiate in a homogeneous medium and the expressions in Section 2.2.1 are valid. The two equivalent problems can be combined by requiring tangential continuity of $\mathbf{E}$ and $\mathbf{H}$ on the surface of the object which yields two coupled integral equations with the unknowns $\mathbf{J}_s$ and $\mathbf{M}_s$.

2.2.3 EFIE for PEC Objects

An EFIE for closed PEC objects in free space is easily derived by following the principle given in the previous section. The surface equivalence principle is used to remove the PEC object leaving only an electric surface current $\mathbf{J}_s$ radiating in free space ($\mathbf{M}_s$ is zero to satisfy $\hat{\mathbf{n}} \times \mathbf{E} = 0$). The surface of the object is denoted by S. The tangential electric field must vanish on S, i.e,

$$\hat{\mathbf{n}} \times \mathbf{E} = \hat{\mathbf{n}} \times \left(\mathbf{E}^i + \mathbf{E}^s\right) = 0\,, \quad \mathbf{r} \in S. \tag{2.10}$$

A particularly useful form of the EFIE for a PEC object can be derived by using (2.3a) and (2.6) in (2.5) which leads to

$$\begin{aligned} \hat{\mathbf{n}} \times \mathbf{E}^i(\mathbf{r}) = \hat{\mathbf{n}} \times \Bigg(& j\omega\mu \int_S \mathbf{J}_s(\mathbf{r}') G(\mathbf{r}, \mathbf{r}')\, dS' \\ & - \frac{1}{j\omega\epsilon} \nabla \int_S \nabla'_s \cdot \mathbf{J}_s(\mathbf{r}') G(\mathbf{r}, \mathbf{r}')\, dS' \Bigg)\,, \quad \mathbf{r} \in S\,, \end{aligned} \tag{2.11}$$

where $\nabla'_s \cdot$ denotes the surface divergence with respect to the primed coordinates and the equation of continuity $j\omega\rho_s = -\nabla_s \cdot \mathbf{J}_s$ was used to eliminate ρ_s. This form of the EFIE is known as the mixed-potential formulation since both scalar and vector potentials are involved in the derivation. The advantage of this form is that the divergence operator is acting on the source term in the last integral in (2.11). The gradient operator appearing outside this integral can also be handled in an elegant way which will be described in Section 3.2.3. In this way, the integrals appearing in the EFIE are only weakly singular[2]. Other forms of the EFIE involve both strongly singular and hypersingular integrals.

The EFIE in (2.11) can be written in the shorter notation as

$$\mathcal{T}\mathbf{J}_s = \hat{\mathbf{n}} \times \mathbf{E}^i\,, \tag{2.12}$$

where $\mathcal{T}$ is a linear operator. The inner product space used here and some basic properties of linear operators are defined in Appendix C.1. The unknown $\mathbf{J}_s$ belongs to the domain D of $\mathcal{T}$ and $\hat{\mathbf{n}} \times \mathbf{E}^i$ belongs to the range R of $\mathcal{T}$. The operator $\mathcal{T}$ for the EFIE is the sum of a compact operator and an unbounded operator [52]. An unbounded operator implies that the eigenvalues may be infinite which will be discussed further in Section 2.4.1. Also, the EFIE operator is neither self-adjoint nor positive definite [52]. The adjoint operator is in fact an operator similar to $\mathcal{T}$ but with G replaced by $G^\dagger$ where † denotes complex conjugation [55]. Hsiao and Kleinman [56] found that the domain and range of $\mathcal{T}$ are the same function spaces. Integral equations in the form of (2.12) are referred to as Fredholm integral equations of the first kind since the unknown quantity only appears inside the integral [57]. Integral equations of the first

[2]The integrals encountered in many physical problems are classified as weakly singular, strongly singular, or hypersingular [54]. For $R \to 0$ the integrands in these three classes behave as R^{-1}, R^{-2}, and R^{-3}, respectively.

kind are often illconditioned which leads to difficulties when attempting a numerical solution [46]. This will be further discussed in Section 2.4.1.

The EFIE was derived above for a closed PEC object. However, it is applicable also to an open PEC object such as an infinitely thin plate. This can be seen by taking the limit as a closed object with finite thickness collapses into an infinitely thin object. The electric surface current in the new equation is then the average of the currents on the two sides of the infinitely thin object. The current component orthogonal to the edge of a thin object must vanish at the edge. This condition can be imposed on the functions in the domain of $\mathcal{T}$ and in this situation the domain and range of $\mathcal{T}$ differ [52]. The outward normal $\hat{\mathbf{n}}$ in (2.11) is not uniquely defined for an infinitely thin object but can be chosen as either of the two normals to the surface S.

2.2.4 MFIE for PEC Objects

The MFIE for PEC objects is usually attributed to Maue [58] and derived in a way similar to the EFIE. The surface equivalence principle is used to remove the PEC object which leaves only electric surface currents radiating in free space. These electric currents maintain the correct field outside S and zero field inside S. The MFIE derived below is therefore referred to as the exterior MFIE. The boundary condition for the magnetic field on a PEC surface is

$$\hat{\mathbf{n}} \times \mathbf{H}(\mathbf{r}) = \hat{\mathbf{n}} \times \left(\mathbf{H}^i(\mathbf{r}) + \mathbf{H}^s(\mathbf{r})\right) = \mathbf{J}_s(\mathbf{r})\,, \quad \mathbf{r} \in S\,. \tag{2.13}$$

Using (2.3a) and (2.4b) in this equation yields

$$\hat{\mathbf{n}} \times \mathbf{H}^i(\mathbf{r}) = \mathbf{J}_s(\mathbf{r}) - \hat{\mathbf{n}} \times \left(\nabla \times \int_S \mathbf{J}_s(\mathbf{r}')G(\mathbf{r},\mathbf{r}')\,dS'\right)\,, \quad \mathbf{r} \in S. \tag{2.14}$$

The curl operator can be moved inside the integral by using the results of Appendix A.2. This leads to

$$\hat{\mathbf{n}} \times \mathbf{H}^i(\mathbf{r}) = \frac{\mathbf{J}_s(\mathbf{r})}{2} + \hat{\mathbf{n}} \times \int_S \mathbf{J}_s(\mathbf{r}') \times \nabla G(\mathbf{r},\mathbf{r}')\,dS'\,, \quad \mathbf{r} \in S\,, \tag{2.15}$$

where the bar on the integral sign indicates that the point $\mathbf{r}' = \mathbf{r}$ is excluded from the integration. The expression in (2.15) is the most common form of the exterior MFIE and is valid for a smooth surface. For more general surfaces the term $\frac{1}{2}\mathbf{J}_s(\mathbf{r})$ should be replaced by $\frac{\Omega}{4\pi}\mathbf{J}_s(\mathbf{r})$ where Ω is the exterior solid angle at $\mathbf{r}$ [59]. It is noted that the interior MFIE differs from (2.15) by a sign on the term $\frac{\mathbf{J}_s(\mathbf{r})}{2}$. When implementing the MFIE it is advantageous to use the identity

$$\begin{aligned}&\hat{\mathbf{n}} \times (\mathbf{J}_s(\mathbf{r}') \times \nabla G(\mathbf{r},\mathbf{r}')) = \\ &\frac{G(\mathbf{r},\mathbf{r}')}{|\mathbf{r}-\mathbf{r}'|}\left(\frac{1}{|\mathbf{r}-\mathbf{r}'|} + jk\right)\left[\hat{\mathbf{n}} \cdot (\mathbf{r}'-\mathbf{r})\mathbf{J}_s(\mathbf{r}') - (\hat{\mathbf{n}} \cdot \mathbf{J}_s(\mathbf{r}'))\,(\mathbf{r}'-\mathbf{r})\right].\end{aligned} \tag{2.16}$$

This expression is only weakly singular whereas the integrand in (2.15) is strongly singular. Note also that (2.16) is zero if the observation point $\mathbf{r}$ is located in the plane of the surface current.

The MFIE may be written in the shorter notation

$$\left(\frac{1}{2}\mathcal{I} + \mathcal{K}\right)\mathbf{J}_s = \hat{\mathbf{n}} \times \mathbf{H}^i, \tag{2.17}$$

where $\mathcal{I}$ is the identity operator and $\mathcal{K}$ is a compact operator [52]. This type of operator has much nicer properties than the unbounded EFIE operator. Most importantly, the eigenvalues of the MFIE operator are always finite. The MFIE operator is neither self-adjoint nor positive definite [52]. The adjoint of the MFIE operator was found by Marin [60]. As for the EFIE, the domain and range of the MFIE operator are the same functions spaces [56]. Integral equations that can be written as in (2.17) are known as Fredholm integral equations of the second kind and are much more amenable for a stable numerical solution than integral equations of the first kind [46]. This will be discussed further in Section 2.4.2.

The MFIE above was derived for closed objects. Unfortunately, it is not applicable to open surfaces unless the currents on each side of the open surface are left as independent unknowns. This will lead to a more complicated numerical solution and double the number of unknowns in comparison to the EFIE.

2.2.5 Uniqueness of Solutions

When applied to a closed object the EFIE and MFIE fail to provide a unique solution for all frequencies. The non-uniqueness is caused by homogeneous solutions, i.e., solutions that fulfill the boundary conditions with zero incident field. The homogeneous solutions are also known as spurious solutions. They correspond to eigenvalues with zero magnitude and belong to the so-called null-space of the operators. Physically, the spurious solutions of the EFIE are the resonant modes of a PEC cavity. These modes radiate zero field outside the object but their existence compromises a numerical solution. A cavity made of a perfect magnetic conductor supports similar resonant magnetic surface currents. The spurious solutions of the MFIE can be interpreted as the electric currents induced by the resonant magnetic currents, if those latter currents are placed on the surface of the corresponding PEC cavity [61]. These solutions are non-physical and radiate a non-zero field outside the object. Peterson [62] considered the numerical consequences of spurious solutions and conducted a survey of remedies, a few of which are mentioned below.

The most common way to avoid homogeneous solutions is by solving the combined field integral equation (CFIE) [63]. The CFIE is obtained as a linear combination of the EFIE and MFIE which in operator form leads to

$$\alpha\mathcal{T}\mathbf{J}_s + (1-\alpha)\eta\left(\frac{1}{2}\mathcal{I} + \mathcal{K}\right)\mathbf{J}_s = \alpha\hat{\mathbf{n}} \times \mathbf{E}^i + (1-\alpha)\eta\hat{\mathbf{n}} \times \mathbf{H}^i\,, \tag{2.18}$$

where α is a real number between 0 and 1 and $\eta = \sqrt{\mu_0/\epsilon_0}$ is the intrinsic impedance of free space. Usually, $0.2 < \alpha < 0.8$ is a good choice [64]. The EFIE and MFIE have the same resonance frequencies but their null spaces differ. The null space of the combined equation is empty and the CFIE has no spurious solutions, except at

complex frequencies corresponding to the resonance frequencies of a cavity with resistive walls [64, p. 643]. The CFIE is a second kind integral equation but involves an unbounded operator that may lead to infinite eigenvalues.

Mautz and Harrington [65] proposed a combined-source formulation in which electric surface currents are supplemented by fictitious magnetic surface currents. The resulting equation is very similar to the CFIE but the actually induced currents are not available. Yaghjian [61] formulated augmented integral equations by enforcing the boundary conditions on the normal as well as the tangential field components. These augmented equations are free of spurious solutions for almost any practical object but require the solution of an overdetermined linear system. Woodworth and Yaghjian [66] formulated dual-surface integral equations by adding observation points on a secondary surface slightly displaced from the actual surface. The contributions from the secondary surface are added with complex weights. The dual-surface MFIE is particularly interesting since its operator is bounded and at the same time free of eigenvalues with zero magnitude (due to the absence of spurious solutions). This implies that the matrix condition number of the dual-surface MFIE is bounded which will also be discussed in Section 2.4.2.

The CFIE and the dual-surface MFIE are the most suitable candidates for avoiding spurious solutions. The CFIE usually leads to the shortest matrix fill time since the field is only calculated on the actual surface. The EFIE and MFIE parts can be computed simultaneously since they both contain the terms $\mathbf{r}'$, $G(\mathbf{r}, \mathbf{r}')$, and $\mathbf{J}(\mathbf{r}')$. In addition, the CFIE is easy to implement if the EFIE and MFIE solutions are already available. On the other hand, the CFIE operator is unbounded which might lead to eigenvalues with large magnitude. In contrast, the dual-surface MFIE operator is bounded which is a strong argument for this formulation. Nevertheless, the CFIE was employed in this work due to its shorter matrix fill time.

2.3 The Method of Moments

The MoM is a discretization scheme for equations of the form

$$\mathcal{L}\mathbf{f} = \mathbf{g}\,, \tag{2.19}$$

where $\mathcal{L}$ is a linear integro-differential operator, $\mathbf{g}$ is a known function, and $\mathbf{f}$ is the unknown function to be determined. Typical examples of such equations are the EFIE and MFIE in (2.12) and (2.17), respectively. The MoM gained its popularity in the electromagnetic community through the work of Harrington [1] but can be traced back to the Ritz-Galerkin procedure applied much earlier [46]. The first step in the MoM is to approximate the unknown function $\mathbf{f}$ by a linear combination of known functions $\mathbf{B}_n$, $n = 1, 2, ..., N$. The approximation is

$$\mathbf{f} \approx \mathbf{f}^N = \sum_{n=1}^{N} I_n \mathbf{B}_n\,, \tag{2.20}$$

where I_n are unknown coefficients to be determined. The functions $\mathbf{B}_n$ are known as basis functions or expansion functions and their form will be discussed later. In

practical problems it is always required to use a finite N such that $\mathbf{f}$ is approximated in the finite-dimensional subspace spanned by the basis functions. The residual is defined as

$$\mathbf{r}^N = \mathbf{g} - \mathcal{L}\mathbf{f}^N = \mathbf{g} - \sum_{n=1}^{N} I_n \mathcal{L}\mathbf{B}_n \,, \tag{2.21}$$

where the linearity of the operator was used. The residual is forced to be orthogonal to another N-dimensional subspace spanned by a set of functions $\mathbf{T}_m$, $m = 1, 2, ..., N$. This condition is expressed as

$$\langle \mathbf{T}_m, \mathbf{r}^N \rangle = 0, \quad m = 1, 2, \ldots, N \,, \tag{2.22}$$

where the inner product $\langle \cdot, \cdot \rangle$ is defined in Appendix C.1. The functions $\mathbf{T}_m$ are known as testing or weighting functions. The MoM is sometimes referred to as the method of weighted residuals which is clear from the expression above. Inserting (2.21) in (2.22) leads to the matrix equation

$$\bar{\mathbf{Z}}\mathbf{I} = \mathbf{V} \,, \tag{2.23}$$

where $\bar{\mathbf{Z}}$ and $\mathbf{V}$ have the elements

$$Z_{mn} = \langle \mathbf{T}_m, \mathcal{L}\mathbf{B}_n \rangle \,, \tag{2.24a}$$

$$V_m = \langle \mathbf{T}_m, \mathbf{g} \rangle. \tag{2.24b}$$

The elements I_n of $\mathbf{I}$ are the desired coefficients in (2.20). The matrix $\bar{\mathbf{Z}}$ is often referred to as the MoM matrix of the impedance matrix and $\mathbf{V}$ is referred to as the excitation vector.

The MoM is a projection method since it projects an unknown function onto the N-dimensional subspace spanned by the basis functions. The coefficients in the projection are chosen to ensure that the residual is orthogonal to the N-dimensional subspace spanned by the testing functions. For a general $\mathcal{L}$ it is not possible to say anything about the convergence of $\mathbf{f}^N$ to $\mathbf{f}$ [67]. In fact, the MoM does not guarantee that the coefficients I_n are optimal. If the testing functions are poorly chosen the residual might have large components outside the space spanned by the testing functions. In general, this is avoided if the testing functions can accurately represent both $\mathbf{g}$ and $\mathcal{L}\mathbf{f}^N$. This requires that $\mathbf{T}_m$ is in the range of $\mathcal{L}$ [55].

2.3.1 Method of Least Squares

The error $\|\mathbf{f} - \mathbf{f}^N\|$ is minimized if

$$\langle \mathbf{B}_m, \mathbf{f} - \mathbf{f}^N \rangle = 0, \quad m = 1, 2, \ldots, N \tag{2.25}$$

This condition ensures that $\mathbf{f}^N$ is as close as possible to $\mathbf{f}$ for the given choice of $\mathbf{B}_m$. The condition differs from that of (2.22) which can be seen by applying the operator $\mathcal{L}$ to (2.25). This leads to

$$\begin{aligned} &\langle \mathcal{L}\mathbf{B}_m, \mathcal{L}\mathbf{f} - \mathcal{L}\mathbf{f}^N \rangle = \\ &\langle \mathcal{L}\mathbf{B}_m, \mathbf{g} - \mathcal{L}\mathbf{f}^N \rangle = \\ &\qquad \langle \mathcal{L}\mathbf{B}_m, \mathbf{r}^N \rangle = 0, \quad m = 1, 2, \ldots, N. \end{aligned} \tag{2.26}$$

Comparing this expression with (2.22) implies that the error $\|\mathbf{f} - \mathbf{f}^N\|$ is minimized if

$$\mathbf{T}_m = \mathcal{L}\mathbf{B}_m. \tag{2.27}$$

This condition ensures that the testing functions belong to the range of the operator. This is desirable since $\mathbf{r}^N$ also belong to the range of the operator and $\mathbf{T}_m$ must be a good approximation of $\mathbf{r}^N$. This special case of MoM is known as the method of least squares. However, the testing functions in (2.27) are not practical.

2.3.2 Galerkin Method

The EFIE and MFIE operators presented in sections 2.2.3 and 2.2.4 have the same domain and range [56]. In other words, if $\mathbf{B}_m$ is a good basis for the domain of $\mathcal{L}$ it is also a good basis for the range of $\mathcal{L}$. This suggests that the choice

$$\mathbf{T}_m = \mathbf{B}_m \tag{2.28}$$

might be as good as (2.27) since both conditions ensure that $\mathbf{T}_m$ is in the range of $\mathcal{L}$. The orthogonality condition in (2.22) then becomes

$$\langle \mathbf{B}_m, \mathbf{r}^N \rangle = 0, \quad m = 1, 2, \ldots, N. \tag{2.29}$$

This special case of MoM is known as Galerkin's method or MoM with Galerkin testing. Many authors have said that there is nothing special about Galerkin's method and that basis and testing functions can be chosen independently, e.g. Harrington [68]. However, based on the reaction concept by Rumsey [69] it was shown by Wandzura [70] that Galerkin's method results in so-called superconvergence for scattering computations. By assuming that the surface current error is $\Delta\mathbf{f}$ such that $\mathbf{f} = \mathbf{f}^N + \Delta\mathbf{f}$, Wandzura found that the error of the backscattered field is proportional to

$$\Delta\mathbf{E} \propto \langle (\mathbf{f}^N)^\dagger, \mathbf{r}^N \rangle + O(\Delta\mathbf{f}^2) = \sum_{m=1}^{N} I_m \langle \mathbf{B}_m^\dagger, \mathbf{r}^N \rangle + O(\Delta\mathbf{f}^2)\,, \tag{2.30}$$

where † denotes complex conjugation. By comparison with the Galerkin condition in (2.29) it is observed that the first term cancels if $\mathbf{B}_m$ is real and the resulting error is then second-order in $\Delta\mathbf{f}$. Consequently, Galerkin testing does not lead to the smallest possible surface current error but it leads to the smallest possible far field error. This conclusion fits well with the observations of Warnick and Chew [71] that employed Galerkin testing and found that *the scattering amplitude is more accurate than the surface current*. A typical example of this is considered in Chapter 5 of this thesis. The primary objective in CEM applications is often an accurate value of the far field which is obtained by Galerkin testing. If an accurate value of the surface current is needed the method of least squares in Section 2.3.1 is better.

Although Galerkin testing is optimal for far fields, other testing schemes might perform equally well. This was shown by Peterson *et al.* [72] for a MoM scheme using polynomial basis and testing functions. They found that the surface current error depends on the choice of basis functions and is largely independent of the testing functions. The far field error, however, depends on both the basis and testing functions. For a fixed number of basis and testing functions, it was demonstrated that the combined polynomial order of the basis and testing functions determined the error. As an example, 1st-order basis functions and 3rd-order testing functions yield the same far field accuracy as 2nd-order basis functions and 2nd-order testing functions. Consequently, Galerkin testing is admittedly optimal for far fields but non-Galerkin testing can be equally good.

2.3.3 Basis Functions

The previous sections discussed two particular testing schemes that relate the testing functions to the basis functions. That discussion was general and nothing was said about the specific choice of basis functions. This section discusses a few fundamentally different kinds of basis functions and their properties.

Basis functions can be categorized as entire-domain or subsectional. Entire-domain basis functions are defined on the entire computational domain, e.g., the surface S in (2.11). This is generally not practical for 3-D problems and entire-domain basis functions are rarely used. An exception is a wire antenna where the domain is one-dimensional and a Fourier expansion of the current has proved efficient [73]. Subsectional basis functions are defined on a subdomain of the object and for surfaces the subdomains are usually taken as triangles or quadrilaterals. Well-known examples of such subsectional basis functions are the RWG functions for triangles by Rao *et al.* [3] and the rooftop functions for quadrilaterals by Glisson and Wilton [2]. For surfaces, the subdomains are often referred to as patches. The term elements is used to denote a general type of subdomain, e.g., a wire segment, a surface patch, or a volumetric cell. RWG and rooftop functions provide a piecewise linear expansion of the surface current, i.e., the current is expanded in terms of 1st order polynomials. Higher-order basis functions are subsectional basis functions that provide a piecewise 2nd, 3rd, or even

higher-order polynomial expansion[3]. The high-order expansion allows the size of the element to be increased and the overall number of basis functions to be decreased in comparison with a 1st order expansion.

Divergence-conforming basis functions impose normal continuity of a vector quantity between neighboring elements and are suitable for expansion of the surface current in a MoM solution. The enforced continuity avoids buildup of line charges at the boundary between adjacent patches. The Appendices B.2 and B.3 give some details on imposing tangential or normal continuity. A recent study by Peterson [74] suggests that the need for imposing continuity has been overestimated in the past. However, the information embedded in the continuity equation still provide an important reduction in the number of unknowns. This reduction is 50% for rooftop functions but drops down as the order of the basis functions is increased. Some experiments towards enforcing normal as well as tangential continuity were done by Gürel *et al.* [75]. However, they concluded that this approach leads to inaccurate surface currents due to an improper modeling of the surface charge.

Higher-order basis functions can be categorized as interpolatory or hierarchical. The interpolatory ones, e.g. those of Graglia *et al.* [7], interpolate the value of the current at a number of interpolation points such that only one function is non-zero at each interpolation point. This allows a direct physical interpretation of the unknown coefficients. However, for a given expansion order M, all basis functions involve polynomials of order M, including those basis functions that take part in enforcing the continuity between adjacent elements. This limits the applicability of interpolatory basis functions since the expansion order must be kept constant throughout the mesh. To avoid an excessive number of unknowns this requires a mesh with approximately equal length of all element edges. Hierarchical functions, e.g. those of Kolundžija and Popović [6], allow for much greater flexibility. The basis functions of order M are a subset of the basis functions of order $M + 1$ and only the basis functions with a 1st-order polynomial variation along the direction of current flow take part in enforcing the continuity. This enables different expansion orders on different elements in the same mesh[4]. Hierarchical basis functions include the 1st-order basis functions, e.g. RWG or rooftop, as the lowest order functions.

For surfaces, the expansion order is often taken to be one order higher along the direction of current flow than along the transverse direction. The reason for this is most easily explained by an example. A rooftop function provides a 1st-order expansion of the surface current along the direction of current flow but is constant along the transverse direction. This implicitly results in a surface charge that is constant along

[3] Some authors refer to higher-order basis functions as entire-domain basis functions [6] or large-domain basis functions [13]. The convention in this work is to reserve the term entire-domain basis functions for functions that are truly defi ned on the entire computational domain. Higher-order basis functions, or large-domain basis functions, are defi ned on a subsection of the computational domain and it is natural to refer to such functions as subsectional higher-order basis functions. However, the word "subsectional" is usually left out for brevity.

[4] Improving the accuracy of a solution by locally increasing the expansion order is known as p-refi nement in the FEM community. Similarly, improving the accuracy by decreasing the element size is sometimes referred to as h-refi nement.

both directions. Adding an additional unknown to obtain a linear current expansion also in the transverse direction would not increase the overall accuracy of the solution since the surface charge would still be constant along the direction of current flow. This is known as the Nedelec [4] constraint and basis functions satisfying this constraint are sometimes said to be of mixed order. The rooftop basis function can then be referred to as a 0th-order function since the expansion is only polynomial complete to 0th order. This convention is meaningful for higher-order basis functions of the interpolatory kind but not particularly useful for basis functions of the hierarchical kind that allow the expansion orders along the direction of current flow and along the transverse direction to be selected independently. As an example, hierarchical basis functions providing a 5th-order expansion in one direction and a 2nd-order expansion along the other direction are only polynomial complete to 2nd order and would be referred to as 2nd-order basis functions. This is not practical and the convention used in this work thus differs from that used in most works on higher-order basis functions. Henceforth, the term 'order of the basis function' always refers to the expansion order along the direction of current flow. This implies that RWG and rooftop functions are 1st-order basis functions.

The discussion in this section has not answered the important question of which basis functions to choose for a specific problem. Many authors have tried to answer this question, including the already cited works of Sarkar *et al.* [55, 73] and Gürel *et al.* [75]. Another interesting work in this context is that of Aksun and Mittra [76] that investigated the properties of basis and testing functions by considering the convergence of the integrals involved in computing the MoM matrix. These works illustrate that the choice of basis functions is always a tradeoff between different properties. The famous work of Harrington [1, p.7] mentioned four factors that can be used to rate a set of basis functions:

> (1) The accuracy of the solution desired, (2) the ease of evaluation of the matrix elements, (3) the size of the matrix that can be inverted, and (4) the realization of a well-conditioned matrix.

These factors are as valid today as 35 years ago. Low-order basis functions are appropriate when considering (2) and (4) but not (1) and (3). The existing higher-order basis functions are appropriate when considering (1) and (3) but not (2) and (4). The new higher-order basis functions presented in this work constitute an attempt of meeting all four requirements.

2.3.4 Comparison of MoM and Higher-Order Nyström Method

The higher-order Nyström method has attracted much attention in recent years and was briefly mentioned in Section 2.1.2. It appears to be the most direct competitor to MoM and deserves some additional comments. As already mentioned, the Nyström method does not use basis functions but employs a quadrature rule to discretize the integral equation directly. This approach can be seen as a clever way of using Dirac delta functions as basis and testing functions in the MoM. However, the higher-order Nyström

method can achieve much better convergence than such a MoM scheme, simply due to the application of the quadrature rules. The quadrature rules must be corrected locally to account for the singularities of the kernel and these local corrections must be repeated for each quadrature point which turns out to be the dominant contribution to the matrix fill time [77]. In the area of CEM, the Nyström method has been applied to 2-D and 3-D PEC scattering configurations by Kress [78] and Canino *et al.* [77], respectively. The latter work, however, only considered smooth objects. Penetrable objects were considered by Ottusch *et al.* [79]. Apparently, 3-D objects with edges and antenna problems involving generators and wire-surface junctions have not been solved yet. This makes MoM more generally applicable at the present time.

The Nyström method does not explicitly yield the value of the surface current on the object. It yields a set of integration weights that can be used to compute the fields upon insertion in a radiation integral. The radiated far field is therefore obtained in approximately the same steps as required by MoM. On the other hand, the procedure for obtaining surface currents is more troublesome. The radiation integral for the magnetic field must be evaluated on the surface of the object by using the computed integration weights and the surface current is then found from the magnetic field.

In comparison to MoM, the Nyström method excels with its low matrix fill time. However, the Nyström method does not enforce current continuity between adjacent patches. The guaranteed continuity makes MoM superior in terms of accuracy for a fixed number of unknowns but also complicates the meshing of general objects. A comparison of computation times using higher-order Nyström and higher-order MoM/Galerkin methods was conducted by Canino *et al.* [77]. The number of unknowns was kept constant in both methods. This approach does not allow a direct comparison of the relative efficiency of the methods since MoM is more accurate but Nyström is faster. Canino *et al.* note that the Nyström method can be made as accurate as the MoM method by decreasing the mesh size in the Nyström solution with a modest 20% and keeping the expansion order constant. However, this increases the number of unknowns by approximately a factor of 1.5 and thereby also increases the required memory and matrix solution time. For large problems, the matrix solution time is usually the bottleneck, not the matrix fill time. Thus, the extra time used to fill the MoM matrix may be well spent since the matrix solution time, which is dominant, is minimal.

Recently, a method known as higher-order MoM with quadrature-based point matching was proposed by Gedney [80] and Gedney and Lu [81]. This method essentially employs Dirac delta functions as testing functions but delta functions has an associated weighting factor obtained from a quadrature rule. This approach can be seen as a hybrid between MoM/Galerkin and Nyström, that is, the current is expanded in terms of smooth basis functions but continuity is not enforced and the matrix fill time is reduced. The accuracy is apparently slightly better than Nyström but slightly worse than MoM/Galerkin, although no direct comparisons were made by Gedney and Lu [80, 81].

2.4 Error Analysis

Section 2.3 introduced the MoM to find an approximation $\mathbf{f}^N$ to the unknown function $\mathbf{f}$ in an operator equation. However, for the operators and basis functions encountered in CEM, it is generally not possible to show that $\mathbf{f}^N$ converges to $\mathbf{f}$ as N tends to infinity [67]. The MFIE is a Fredholm integral equation of the second kind and involves the sum of a compact operator and a constant operator. By assuming that the basis and testing functions constitute complete and orthogonal sets it is actually possible to prove convergence [52]. However, the basis functions used in MoM rarely fulfill these requirements. The situation is much worse for the EFIE which is a Fredholm integral equation of the first kind involving an unbounded operator. It is not possible to formally prove convergence of MoM for this type of operator. Nevertheless, the MoM has been practiced in CEM for many years and the convergence has been established through experiments. Although convergence cannot be proven in the general case, it is still possible to derive error bounds for simple geometries. This type of analysis lends insight to more general cases and is usually based on the eigenvalue spectrum of the operators. The remainder of this section discusses these eigenvalues and their influence on the matrix condition number which is an important quantity in this context.

2.4.1 Matrix Condition Number

The matrix condition number is an important quantity when dealing with matrix equations. The condition number is defined as [82]

$$\text{cond}\left(\bar{\mathbf{Z}}\right) = \left\|\bar{\mathbf{Z}}\right\| \left\|\bar{\mathbf{Z}}^{-1}\right\| , \tag{2.31}$$

where the norm is usually the 2-norm or the infinity-norm. For the specific case of the 2-norm, the condition number is also given by

$$\text{cond}_2\left(\bar{\mathbf{Z}}\right) = \sqrt{\frac{|\Lambda_{max}|}{|\Lambda_{min}|}}, \tag{2.32}$$

where Λ_{max} and Λ_{min} are the maximum and minimum eigenvalues of $\bar{\mathbf{Z}}\bar{\mathbf{Z}}^H$, respectively. Here, $\bar{\mathbf{Z}}^H$ denotes the transpose and complex conjugate of $\bar{\mathbf{Z}}$.

Consider the matrix equation

$$\bar{\mathbf{Z}}\mathbf{I} = \mathbf{V} \tag{2.33}$$

and assume that the vector $\mathbf{V}$ for some reason has an error $\delta\mathbf{V}$. The relative solution error can then be estimated as [82]

$$\frac{\|\delta\mathbf{I}\|}{\|\mathbf{I}\|} \leq \text{cond}\left(\bar{\mathbf{Z}}\right) \frac{\|\delta\mathbf{V}\|}{\|\mathbf{V}\|}. \tag{2.34}$$

In other words, in a worst-case scenario the relative error on $\mathbf{V}$ is magnified by the condition number and results in a large relative error on $\mathbf{I}$. Similarly, if $\bar{\mathbf{Z}}$ has an error

$\delta\bar{\mathbf{Z}}$, the solution error can be estimated as [82]

$$\frac{\|\delta\mathbf{I}\|}{\|\mathbf{I}+\delta\mathbf{I}\|} \leq \text{cond}\left(\bar{\mathbf{Z}}\right) \frac{\|\delta\bar{\mathbf{Z}}\|}{\|\bar{\mathbf{Z}}\|}. \tag{2.35}$$

Again, the error is magnified by the condition number. For the MoM, $\bar{\mathbf{Z}}$ and $\mathbf{V}$ are found through numerical integration and sometimes the incident field used to compute $\mathbf{V}$ is even based on measured data. In all cases, the small errors present on $\bar{\mathbf{Z}}$ and $\mathbf{V}$ are possibly magnified by the condition number which may lead to large errors on $\mathbf{I}$. In addition, the performance of the matrix solution procedure is also influenced by the condition number. Specifically, the number of iterations required to solve (2.33) by an iterative procedure is proportional to the matrix condition number [23]. These considerations explain why the condition number of $\bar{\mathbf{Z}}$ must be kept as low as possible.

2.4.2 Condition Numbers of EFIE and MFIE Matrices

Condition number estimates for the EFIE and MFIE can be derived for simple objects. Hsiao and Kleinman [56] considered a PEC sphere for which an analytical solution exists. Warnick and Chew [71] considered the EFIE for an infinite PEC strip and made some interesting observations. They found that the condition number increases linearly with the discretization density. The EFIE is an unbounded operator and the eigenvalues have accumulation point at infinity. As the number of basis functions increases, more and more eigensolutions can be represented by the discretized operator. These eigensolutions radiate either propagating fields or evanescent fields. The eigensolutions that radiate evanescent fields are those responsible for the ill-conditioning as the discretization density increases. These evanescent fields represent local interactions and the ill-conditioning can be avoided by using a near-neighbor preconditioner which will be considered in Chapter 4. The eigensolutions that radiate propagating fields represent long-range interactions. These are also a source of ill-conditioning and cause the condition number to grow as the square root of the electrical size of the strip. Unfortunately, the increase in condition number originating from long-range interactions is not avoided by employing a near-neighbor preconditioner.

The fundamentally different properties of the EFIE and the MFIE can be illustrated by an example. A PEC cube is discretized using 10×10 quadrilateral patches on each face and the resulting mesh is shown in the insert of Figure 2.1. The 2-norm condition numbers of the EFIE and MFIE matrices obtained by employing rooftop basis functions and Galerkin testing are displayed in the figure. The frequency is changed such that the electrical length of each edge varies from $\lambda/2$ to $3\lambda/2$. This implies that the discretization density is quite high when the edge length is $\lambda/2$ and quite low when the edge length is $3\lambda/2$. This is clearly reflected in the condition number for the EFIE that decreases as the electrical length of the edge increases, except at the resonance frequencies of the cube. The homogeneous solutions discussed in Section 2.2.5 correspond to eigenvalues with zero magnitude and the condition number blows up at these frequencies. In contrast to the EFIE, the condition number for the MFIE is much lower and remains almost constant away from the resonance frequencies. These

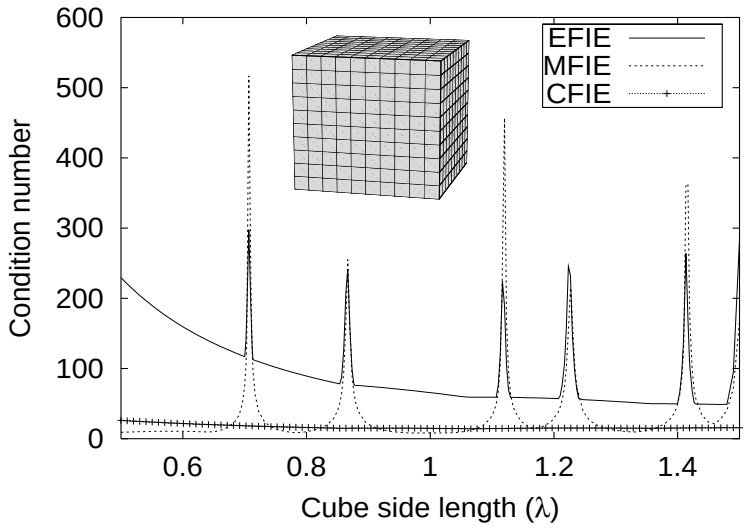

Figure 2.1: *2-norm condition number of MoM matrix for increasing electrical size of PEC cube. The curves are obtained using EFIE, MFIE, and CFIE.*

curves clearly show why Fredholm integral equations of the second kind (MFIE) are preferred over Fredholm integral equations of the first kind (EFIE).

As explained in Section 2.2.5, the CFIE have no homogeneous solutions. The condition number obtained with the CFIE ($\alpha = 0.5$) is also shown in Figure 2.1 and the smooth curve confirms that there are no eigenvalues with zero magnitude. A slightly increased condition number is observed where the electrical length of the edges is small. This is caused by the EFIE part of the CFIE that involves an unbounded operator. Consequently, the CFIE condition number also increases as the discretization density increases but the problem is much less severe than for the EFIE. For practical problems the CFIE should always be preferred over the EFIE and MFIE. Alternatively, ill-conditioning can be completely avoided by using the dual-surface MFIE that has no homogeneous solutions and involves only a bounded operator. However, the matrix fill time is longer for the dual-surface MFIE.

2.4.3 Eigenvalues of Continuous and Discrete Operators

Peterson *et al.* [59] related the eigenvalues of the continuous and discrete operators in the following way. Consider the continuous eigenvalue equation

$$\mathcal{L}\mathbf{e} = \Lambda\mathbf{e}\,, \tag{2.36}$$

where $\mathbf{e}$ is the eigensolution and Λ is the pertinent eigenvalue. The MoM can be applied to discretize this equation by introducing the approximation

$$\mathbf{e} \approx \sum_{n=1}^{N} I_n \mathbf{B}_n\,, \tag{2.37}$$

which is similar to (2.20). Inserting this in (2.36) and testing with $\mathbf{T}_m$ leads to

$$\sum_{n=1}^{N} \langle \mathbf{T}_m, \mathcal{L}\mathbf{B}_n \rangle I_n = \Lambda \sum_{n=1}^{N} \langle \mathbf{T}_m, \mathbf{B}_n \rangle I_n, \quad m = 1, 2, \ldots, N. \tag{2.38}$$

This can be written in matrix notation as

$$\bar{\mathbf{Z}}\mathbf{I} = \Lambda \bar{\mathbf{S}}\mathbf{I}, \tag{2.39}$$

where $\bar{\mathbf{Z}}$ is the standard MoM matrix in (2.24a) and the matrix $\bar{\mathbf{S}}$ is has the elements

$$S_{mn} = \langle \mathbf{T}_m, \mathbf{B}_n \rangle. \tag{2.40}$$

Equation (2.39) can be rewritten as

$$\bar{\mathbf{S}}^{-1}\bar{\mathbf{Z}}\mathbf{I} = \Lambda\mathbf{I}\,, \tag{2.41}$$

which is an eigenvalue equation for the eigenvalues of the matrix $\bar{\mathbf{S}}^{-1}\bar{\mathbf{Z}}$. However, Λ is also an eigenvalue of the continuous operator $\mathcal{L}$. Consequently, the eigenvalues of $\bar{\mathbf{S}}^{-1}\bar{\mathbf{Z}}$ and $\mathcal{L}$ are the same provided that the basis functions can accurately represent the eigensolution $\mathbf{e}$. On the other hand, the eigenvalues of the continuous operator $\mathcal{L}$ and the MoM matrix $\bar{\mathbf{Z}}$ are generally not the same except when $\bar{\mathbf{S}}$ is a unit diagonal matrix, i.e., the basis and testing functions are orthonormal.

First-order subsectional basis and testing functions produce a matrix $\bar{\mathbf{S}}$ that is close to a diagonal matrix due to the disjoint supports of the basis and testing functions. Such basis functions produce relatively well-conditioned MoM matrices which was demonstrated in Section 2.4.2 for rooftops. However, for higher-order basis functions the number of functions with common or overlapping supports can be very large, e.g., larger than 100, implying a larger bandwidth for the matrix $\bar{\mathbf{S}}$. Such basis functions are known to produce relatively ill-conditioned MoM matrices. Nevertheless, if the higher-order functions are *orthogonal*, $\bar{\mathbf{S}}$ is a diagonal matrix and similar to the $\bar{\mathbf{S}}$ produced by the first-order functions. This implies that the eigenvalues of the MoM matrices, and thus the condition numbers, remain the same for first-order basis functions and higher-order orthogonal basis functions. In other words, the benefits of the higher-order basis functions can be exploited while maintaining a favorable condition number provided that the higher-order basis functions are orthogonal. This insight will be used in Chapter 3 to formulate a new set of higher-order basis fiunctions.

2.5 Summary

This chapter presented a brief overview of CEM. Then it was explained how integral equations for electromagnetic problems are derived by establishing a source-field relationship, employing an equivalence principle, and enforcing a boundary condition. The MoM was introduced as a discretization scheme for integral equations and the method of least squares and Galerkin's method were considered as two special cases. The choice of basis functions is important for MoM and different categories of basis functions and their properties were discussed. Finally, the important role played by the matrix condition number was considered. Small errors on the MoM matrix or the excitation vector may lead to a large solution error if the condition number is high. If an iterative procedure is used to solve the matrix system, the number of iterations and thus the solution time is proportional to the condition number. Furthermore, it was pointed out that orthogonality is important for higher-order basis functions since this property will allow the expansion order to be increased without increasing the condition number.

Chapter 3
New Higher-Order Hierarchical Legendre Basis Functions

Section 2.3.3 outlined some basic requirements of basis functions for the MoM. Most importantly, the basis functions should provide an accurate expansion of the unknown quantity using a low number of unknowns. Higher-order basis functions are ideally suited for this purpose. As will be apparent from the survey conducted below, the existing higher-order basis functions suffer from one or more of the following undesirable properties:

- The basis functions are hard to derive and implement for arbitrary orders.
- The basis functions are not hierarchical.
- The basis functions produce an ill-conditioned matrix.

This chapter attempts to formulate a new set of basis functions that avoids these drawbacks.

First, a brief survey of existing higher-order basis functions is performed. Next, the new basis functions are derived for surfaces and their properties discussed. The formulation is generalized to wires and volumes and details are given for the evaluation of the MoM matrix elements for the particular case of the EFIE for a PEC surface. Finally, numerical results are presented to validate the new basis functions and demonstrate that higher-order convergence is obtained. In addition, numerical comparisons with two existing types of basis functions confirm that the new basis functions lead to a relatively well-conditioned MoM matrix.

3.1 Survey

A large number of works dealing with higher-order basis functions have been published in the last 15 years, most of these in the context of FEM. With a few exceptions the following survey has been narrowed down to the works related to MoM and divergence-conforming basis functions.

Wandzura [5] formulated hierarchical basis functions on curved triangular patches. These basis functions incorporate RWG functions as the lowest order function and the higher-order order terms are based on a power series expansion. The basis functions

appear quite complicated to implement for arbitrary orders and orthogonality was not considered. In addition, no numerical results were presented. The work of Wandzura was continued by Hamilton *et al.* [9] that presented higher-order hierarchical basis functions based on products of Jacobi and Legendre polynomials. The rather short treatment in [9] did not address orthogonality and condition numbers. The expressions for these basis functions are rather involved and the basis functions appear complicated to implement for arbitrary orders. This conclusion was also reached by the same authors in a later paper [77].

Kolundžija and Popović [6, 8] derived higher-order hierarchical basis functions for bilinear quadrilateral patches. These basis functions are based on a power series expansion and incorporate rooftop functions as the lowest order function. Implementation for arbitrary orders is relatively easy but it will be shown later that the matrix condition number of increases rapidly for increasing polynomial order. Nevertheless, these functions have been rather successful and were applied to many problems, e.g., surface integral equations for metallic and dielectric objects by Kolundžija [18], volumetric integral equations by Notaroš and Popović [11] and Notaroš *et al.* [13], and a FEM formulation by Andersen and Volakis [83]. Recently, Djordević and Notaroš [14] investigated possible improvements of the basis functions by considering combinations of Chebyshev and ultra-spherical polynomials. The latter work and the work presented in this thesis were conducted simultaneously and possess many similarities. Both works are aimed at improving the condition number of the MoM matrix and attempt to do so by considering orthogonal polynomials. However, Djordević and Notaroš obtain condition numbers that are higher than those obtained with interpolatory basis functions [84]. As will be clear later, the approach suggested here provides condition numbers that are lower than those obtained with interpolatory basis functions. This seems to suggest that the approach presented in this work is more appropriate than that of [14].

Aberegg *et al.* [10] presented second-order basis functions that are neither interpolatory nor hierarchical. These functions were applied on curved triangular or quadrilateral patches and orthogonality was not considered. The basis functions are not readily extended to higher orders and this possibility was not discussed in [10].

Graglia *et al.* [7] developed divergence- and curl-conforming higher-order interpolatory basis functions for surfaces and volumes. These basis functions are based on Lagrange interpolation polynomials and interpolate the unknown vector quantity at a number of interpolation points depending on the expansion order. However, the expansion order must be kept constant throughout the mesh which constitutes the main drawback of interpolatory functions. In addition, implementation for arbitrary orders is somewhat troublesome since the basis functions and their derivatives cannot be computed by recurrence formulas. Nevertheless, many authors have applied these basis functions up to third order, e.g., Chew *et al.* [64]. The primary motivation for using these functions have been favorable condition numbers. It is therefore natural to use the condition numbers obtained with these basis functions as a reference which will be done in Section 3.3. Kang *et al.* [85] considered an extension to the basis functions of Graglia *et al.* . The idea was to allow defective meshes, i.e. meshes where neigh-

boring patches may not share an edge in its full length. This was done by relaxing the requirement of a continuous normal component between neighboring patches at the expense of an increased number of unknowns.

Cai *et al.* [12] presented higher-order hierarchical basis functions for triangular and quadrilateral patches. In fact, these basis functions are only hierarchical for expansion orders higher than two since the lowest order function (RWG) is discarded in the second-order basis functions. The expansion order is fixed to be the same along the direction of current flow and the orthogonal direction which makes the basis functions incompatible with the Nedelec constraint [4]. In addition, it precludes the use of patches with significantly different side lengths. The basis functions for orders higher than four incorporate Legendre polynomials but they are multiplied by other functions and the resulting basis functions are not orthogonal.

Orthogonality was not discussed in any of the works on higher-order basis functions for MoM cited above. In the FEM context, Webb [86] used partial Gramm-Schmidt orthogonalization to derive a set of hierarchical functions. This approach is interesting since it guarantees the orthogonality of the higher-order functions. However, the basis functions are not easily implemented for arbitrary orders and the orthogonality cannot be maintained if normal continuity is to be enforced. The possibility of using the approach of Webb is further discussed in the following section.

Higher-order basis functions enable large patches which calls for higher-order curvilinear geometry modeling. Several authors have treated higher-order curvilinear surface modeling for both low-order [87]-[89] and higher-order [7, 90] basis functions. These works all used curved elements based on Lagrange interpolation polynomials which have been adopted here. This formulation is presented in Appendix B for the specific case of curved quadrilaterals of arbitrary order. However, it is emphasized that the basis functions developed here are also applicable to other types of parametric geometries, e.g., the non-uniform rational B-splines (NURBS) and Bézier patches considered by Valle *et al.* [91].

3.2 New Higher-Order Legendre Basis Functions

A new set of higher-order hierarchical basis functions are developed in this section. They are derived by considering orthogonality and ease of implementation for arbitrary order as important parameters.

3.2.1 Construction of the Basis for Quadrilaterals

Consider a curved quadrilateral patch of arbitrary order with an associated parametric curvilinear coordinate system defined by $-1 \leq u, v \leq 1$ (see Appendix B). The surface current density on each patch is expanded in terms of its contravariant components as

$$\mathbf{J}_s = J_s^u \mathbf{a}_u + J_s^v \mathbf{a}_v \,, \tag{3.1}$$

where $\mathbf{a}_u$ and $\mathbf{a}_v$ are the covariant unitary vectors $\mathbf{a}_u = \frac{\partial \mathbf{r}}{\partial u}$ and $\mathbf{a}_v = \frac{\partial \mathbf{r}}{\partial v}$. Without loss of generality only u-directed currents are considered in the following with the

understanding that v-directed currents can be obtained by interchanging u and v. The u-directed current is expanded as

$$J_s^u(u,v) \;=\; \frac{1}{\mathcal{J}_s(u,v)} \sum_{m=0}^{M^u} \sum_{n=0}^{N^v} a_{mn}^u P_m(u)\, P_n(v)\,, \tag{3.2}$$

where $\mathcal{J}_s(u,v) = |\mathbf{a}_u \times \mathbf{a}_v|$ is the surface Jacobian, a_{mn}^u are unknown coefficients, and $P_m(u)$ and $P_n(v)$ are expansion polynomials. It is shown in Appendix B.3 that the vector $\mathbf{a}_u$ in (3.1) and the factor $\mathcal{J}_s(u,v)$ in (3.2) are required by the curvilinear geometry modeling when normal continuity between patches is desired. However, they make it difficult to derive orthogonal basis functions for all possible patch shapes. Therefore, the following discussion about orthogonality is strictly related to the expansion polynomials $P_m(u)$ and $P_n(v)$. Thus, the orthogonality of the basis functions is only maintained when $\frac{\mathbf{a}_u}{\mathcal{J}_s(u,v)}$ has no u- and v-dependence, i.e., on rectangular or rhomboid-shaped patches. Nevertheless, the numerical results in Section 3.3 confirm that favorable condition numbers can also be obtained for more general patch shapes.

The choice of polynomials in (3.2) is important for the resulting matrix condition number. Kolundžija and Popović [6] proposed to use the power expansion $P_m(u) = u^m$. However, these polynomials are not orthogonal and lead to severely ill-conditioned MoM matrices as will be shown later. The polynomials $P_m(u)$ and $P_n(v)$ chosen in this work are the Legendre polynomials

$$P_m(u) = \frac{1}{2^m\, m!} \frac{d^m}{du^m}(u^2-1)^m, \tag{3.3}$$

that satisfy the orthogonality relation

$$\int_{-1}^{1} P_i(u) P_j(u)\, du = \frac{2}{2i+1}\, \delta_{ij}\,, \tag{3.4}$$

where δ_{ij} is the Kronecker delta function.

The expansion in (3.2) is not appropriate if normal continuity of the current flowing across patch boundaries is to be enforced. Instead, the polynomials along the direction of current flow, i.e., the u-direction, must be modified such that only a single low-order polynomial is non-zero at the edge $u = -1$, a single low-order polynomial is non-zero at the edge $u = 1$, and the higher-order polynomials are zero at both edges. This modification can be done in several different ways. To illustrate the properties of the modified polynomials discussed below, a matrix $\tilde{\mathbf{S}}^{1D}$ is defined with the elements

$$S_{ij}^{1D} = \int_{-1}^{1} P_i^{mod}(u)\, P_j^{mod}(u)\, du\,, \tag{3.5}$$

where $P_i^{mod}(u)$ are the modified polynomials to be defined. This matrix should preferably be a diagonal matrix, indicating that the modified polynomials are orthogonal. However, complete orthogonality is not possible if the lowest order expansion

($M^u = 1$) is required to be the rooftop functions $1 \pm u$. One possible modification was applied to the power expansion by Kolundžija and Popović [6] and was later used with three different types of polynomials by Djordević and Notaroš [14]. Applying the same modification to the Legendre polynomials yields the modified polynomials

$$P_m^{mod}(u) = \begin{cases} 1-u, & m=0 \\ 1+u, & m=1 \\ P_m(u)-1, & m=2,4,6,\ldots \\ P_m(u)-u, & m=3,5,7,\ldots \end{cases} \tag{3.6}$$

Unfortunately, the modified polynomials $P_m^{mod}(u)$ obtained from this procedure are far from orthogonal, due to the subtracted terms for $m \geq 2$ in (3.6). In fact, all higher-order functions have non-zero inner products with the two lowest order functions, and all even (odd) higher-order functions have non-zero inner products with all other even (odd) higher-order functions. This is illustrated in Figure 3.1(a) that shows the matrix $\bar{\mathbf{S}}^{1D}$ for the polynomials $P_m^{mod}(u)$ for $0 \leq m \leq 10$. As seen, the coupling between odd and even polynomials results in a large number of non-zero elements, indicating that the orthogonality of the Legendre polynomials have been destroyed by the modification.

The lack of orthogonality can be avoided by using partial Gramm-Schmidt orthogonalization as proposed by Webb [86], to orthogonalize all higher-order functions. Nevertheless, this approach cannot be used to orthogonalize the higher-order functions with respect to the two lowest order functions, $1 \pm u$, since this would destroy the necessary property $P_m^{mod}(\pm 1) = 0$, $m \geq 2$. This is illustrated in Figure 3.1(b) that shows the matrix $\bar{\mathbf{S}}^{1D}$ obtained by applying Gramm-Schmidt orthogonalization to the modified polynomials in (3.6). The non-zero elements in the first two rows and columns indicate the non-zero inner products of the higher-order polynomials with the two lowest-order polynomials, $1 \pm u$. In addition, the application of Gramm-Schmidt orthogonalization creates a set of polynomials that cannot be evaluated through a recurrence formula which complicates implementation for arbitrary orders.

Instead of the two modifications described above, it is proposed here to use the alternative modified higher-order polynomials

$$\widetilde{P}_m(u) = \begin{cases} 1-u, & m=0 \\ 1+u, & m=1 \\ P_m(u)-P_{m-2}(u), & m \geq 2 \end{cases} \tag{3.7}$$

where the superscript ^{mod} is left out for convenience. These polynomials have the desired property $\widetilde{P}_m(\pm 1) = 0$, $m \geq 2$, and span the same polynomial space as the polynomials in (3.6). Moreover, for $m \geq 4$ the modified polynomials in (3.7) are orthogonal to the two lowest order functions, $1 \pm u$. However, all higher-order polynomials have non-zero inner products with the polynomials two orders lower and two orders higher. This is illustrated in Figure 3.1(c) that shows the matrix $\bar{\mathbf{S}}^{1D}$ for the modified polynomials in (3.7). By comparing the three matrices in Figure 3.1, it is observed that this latter modification provides the lowest number of non-zero terms

and a diagonally strong $\bar{\mathbf{S}}^{1D}$. Thus, the orthogonality of the Legendre polynomials is best preserved by applying the modification in (3.7). It is also noted that the modified polynomials obtained by the Gramm-Schmidt orthogonalization do not posses the desirable features derived from (3.15), (3.16), (3.18), (3.19), and (3.13) in Sections 3.2.2 and 3.2.3.

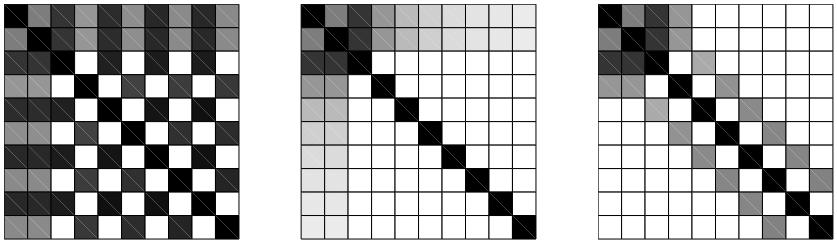

(a) (b) (c)

Figure 3.1: Normalized inner product matrices $\bar{\mathbf{S}}^{1D}$ for the modified polynomials, (a) the modified polynomials $P_m^{mod}(u)$ in (3.6), (b) the modified polynomials $P_m^{mod}(u)$ in (3.6) after Gramm-Schmidt orthogonalization, and (c) the modified polynomials $\widetilde{P}_m(u)$ in (3.7).

The next step is to determine appropriate scaling factors for the basis functions that minimize the condition number. Numerical experiments showed that a good choice is to scale such that the Euclidean norm of each basis function is unity on a square patch of unit side length. The experiments verified that other options, e.g., scaling each function to a maximum value of 1, did not perform equally well. By defining the scaling factors

$$C_m^u = \begin{cases} \frac{\sqrt{3}}{4}, & m = 0, 1 \\ \frac{1}{2}\sqrt{\frac{(2m-3)(2m+1)}{2m-1}}, & m \geq 2 \end{cases} \tag{3.8a}$$

$$C_n^v = \sqrt{n + \frac{1}{2}}, \tag{3.8b}$$

and inserting the modified polynomials $\widetilde{P}_m(u)$ in the initial expansion (3.2), the obtained final expansion is

$$J_s^u(u,v) = \frac{1}{\mathcal{J}_s(u,v)} \sum_{m=0}^{M^u} \sum_{n=0}^{N^v} b_{mn}^u C_m^u \widetilde{P}_m(u)\, C_n^v P_n(v)\,, \tag{3.9}$$

where b_{mn}^u are the new unknown coefficients. An alternative representation that separates the functions which take part in maintaining the normal continuity and the func-

tions which are zero at $u = \pm 1$ is

$$\begin{aligned} J_s^u(u,v) =& \frac{1}{\mathcal{J}_s(u,v)} \sum_{n=0}^{N^v} \Big[b_{0n}(1-u) + b_{1n}(1+u) \Big] C_0^u \, C_n^v P_n(v) \\ &+ \frac{1}{\mathcal{J}_s(u,v)} \sum_{m=2}^{M^u} \sum_{n=0}^{N^v} b_{mn}^u C_m^u \widetilde{P}_m(u) \, C_n^v P_n(v) \, . \end{aligned} \tag{3.10}$$

The properties of the above expansion are further examined below.

3.2.2 Properties of the Expansion

In (3.10), the polynomials with a u-dependence were modified to incorporate normal continuity across patch edges. To be specific, the functions in the first line of (3.10) have a linear variation in the u-direction and are non-zero at $u = \pm 1$. These functions serve to ensure the normal continuity across the v-directed edges and must be matched with similar functions on the neighboring patch. For this reason, these functions are sometimes referred to as edge functions or doublets. The normal component of the basis functions will be continuous provided that the normal components of $\mathbf{a_u}/\mathcal{J}_s$ are the same on both sides of a common edge of two neighboring patches. Using the results (B.11b) and (B.20b) from Appendix B.3, the normal component of $\mathbf{a_u}/\mathcal{J}_s$ across a v-directed edge is

$$\frac{\mathbf{a_u}}{\mathcal{J}_s} \cdot \frac{\mathbf{a}^u}{|\mathbf{a}^u|} = \frac{1}{\mathcal{J}_s |\mathbf{a}^u|} = \frac{1}{|\mathbf{a}_v|} \, , \tag{3.11}$$

where $\mathbf{a}^u$ is the contravariant unitary vector. The quantity $|\mathbf{a}_v|$ remains the same on both sides of the edge since the vectors $\mathbf{a}_v$ on two neighboring patches are tangential to the same edge. Thus, normal continuity is maintained when the surface Jacobian $\mathcal{J}_s$ is included in the expansion. More details can be found in Appendix B.3.

The functions in the second line of (3.10) are zero at $u = \pm 1$ and do not contribute to the normal continuity of the current. They are defined on a single patch and have an m th order polynomial variation in the u-direction, where $m \geq 2$. These functions are often referred to as patch functions or singletons.

The lowest order of approximation yields the well-known rooftop functions which is obtained be choosing ($M^u = 1$, $N^v = 0$) for the u-component. For the v-component obtained by interchanging u and v in (3.9), this corresponds to ($M^v = 1$, $N^u = 0$). The special case $M^u - 1 = M^v - 1 = N^v = N^u$ yields a basis compatible to the Nedelec constraint [4] with $\mathbf{J}_s$ and $\nabla_s \cdot \mathbf{J}_s$ complete to order N^v. Several types of higher-order basis functions, e.g., those of Graglia *et al.* [7], are limited to this special case. However, this is only a good choice if all edges of the patch have approximately equal lengths. For more general patch shapes, M^u and M^v should be chosen independently to avoid introducing unnecessary unknowns. This independent selection is possible with the basis functions in (3.9). In principle, all four parameters M^u, M^v, N^v, and N^u are independent. However, it seems most appropriate to

choose

$$N^u = M^u - 1 \quad \text{and} \quad N^v = M^v - 1. \tag{3.12}$$

This requirement can be seen as a generalized Nedelec constraint which ensures that $\mathbf{J}_s$ and $\nabla_s \cdot \mathbf{J}_s$ are complete to order N^u and N^v along the u- and v-directions, respectively. Numerical experiments confirm that the choice (3.12) is generally optimal.

When implementing the basis functions in (3.9), the Legendre polynomials are efficiently calculated by the recurrence formula

$$P_m(u) = \frac{1}{m}\left[(2m-1)uP_{m-1}(u) - (m-1)P_{m-2}(u)\right] . \tag{3.13}$$

Equations (3.13) and (3.15) imply that by computing the basis function of order m, all polynomials required for computing the basis functions of all lower orders, as well as their corresponding charges, have been computed as a byproduct.

The charge associated with the u-directed currents can be obtained from the continuity equation as

$$\rho_s^u = \frac{1}{\mathcal{J}_s}\frac{j}{\omega}\frac{d}{du}\left(\mathcal{J}_s J_s^u\right) . \tag{3.14}$$

Furthermore, Legendre polynomials satisfy the identity

$$\frac{d}{du}(P_m(u) - P_{m-2}(u)) = \frac{d}{du}\widetilde{P}_m(u) = (2m-1)P_{m-1}(u), \quad m \geq 2 . \tag{3.15}$$

Substituting this into (3.14) yields

$$\begin{aligned}\rho_s^u(u,v) =& \frac{j}{\omega}\frac{1}{\mathcal{J}_s(u,v)}\sum_{n=0}^{N^v}\Big[-b_{0n}+b_{1n}\Big]C_0^u\, C_n^v P_n(v) \\ &+\frac{j}{\omega}\frac{1}{\mathcal{J}_s(u,v)}\sum_{m=2}^{M^u}\sum_{n=0}^{N^v} b_{mn}^u C_m^u (2m-1)P_{m-1}(u)\, C_n^v P_n(v) .\end{aligned} \tag{3.16}$$

The functions in the second line of this equation are all mutually orthogonal and orthogonal to the functions in the first line of the equation. Consequently, the current expansion in (3.9) implicitly yields a higher-order orthogonal expansion of the charge. Note that this is only accomplished by using Legendre polynomials and modifying the polynomials as in (3.7). The significance of the orthogonal charge can be seen when the MoM matrix elements associated with the mixed-potential EFIE with Galerkin testing are evaluated. With $\mathbf{J}_s^p$ being the p'th testing function and $\mathbf{J}_s^q$ the q'th expansion function, the matrix elements have the form

$$Z_{pq} = \langle \mathbf{J}_s^p, L_J(\mathbf{J}_s^q)\rangle - \frac{j}{\omega}\langle \nabla_s \cdot \mathbf{J}_s^p, L_\rho(\nabla_s \cdot \mathbf{J}_s^q)\rangle , \tag{3.17}$$

where $L_J(\cdot)$ is the electric field integral operator associated with the vector potential and $L_\rho(\cdot)$ is the electric field integral operator associated with the scalar potential.

The last inner product appearing in (3.17) is essentially the inner product of the charge associated with the testing function and the operator working on the charge associated with the expansion function. In analogy with the argumentation of Section 2.4.3, this suggests that an orthogonal expansion of the charge will contribute to a favorable condition number of the MoM matrix.

The Legendre polynomials satisfy the relations

$$\int_{-1}^{1} P_n(v)\,dv \quad = \quad 0\,, \quad n>0\,, \tag{3.18a}$$

$$\int_{-1}^{1} vP_n(v)\,dv \quad = \quad 0\,, \quad n>1\,, \tag{3.18b}$$

and for the modified polynomials these imply

$$\int_{-1}^{1} \widetilde{P}_m(u)\,du \quad = \quad 0\,, \quad m>2\,, \tag{3.19a}$$

$$\int_{-1}^{1} u\widetilde{P}_m(u)\,du \quad = \quad 0\,, \quad m>3\,. \tag{3.19b}$$

This property of vanishing moments can be used to estimate the far field radiated by a higher-order basis function. Using a first-order Taylor expansion of the slowly varying far-zone Green's function shows that all functions with $m > 3$ or $n > 1$ radiate zero far field. In other words, the Legendre basis functions are carefully shaped to concentrate the far-zone interactions in the low-order functions, whereas the higher-order terms mostly act as local corrections.

3.2.3 Matrix Element Evaluation

The general expression for the MoM matrix elements is

$$Z_{pq} \quad = \quad \langle \mathbf{T}^p, \mathcal{L}\mathbf{B}^q \rangle, \tag{3.20}$$

where $\mathbf{T}^p$ is the p'th testing function and $\mathbf{B}^q$ the q'th basis function. Explicit expressions will not be given since they depend on the type of integral equation being solved. It is worth noting, that evaluation of $\mathcal{J}_s(u,v)$ is not required when the basis or testing functions appear inside an integral. This will be illustrated by considering the particular case of a mixed-potential surface EFIE (2.11) with Galerkin testing. The matrix elements for this case can be written as

$$\begin{aligned} Z_{pq} = & \int_{S^p} \mathbf{T}^p(\mathbf{r}) \cdot \left(j\omega\mu \int_{S^q} \mathbf{B}^q(\mathbf{r}') G(\mathbf{r},\mathbf{r}')\,dS' \right. \\ & \left. -\frac{1}{j\omega\epsilon} \nabla \int_{S^q} \nabla'_s \cdot \mathbf{B}^q(\mathbf{r}') G(\mathbf{r},\mathbf{r}')\,dS' \right) \\ = & \, j\omega\mu \int_{S^p} \mathbf{T}^p(\mathbf{r}) \cdot \int_{S^q} \mathbf{B}^q(\mathbf{r}') G(\mathbf{r},\mathbf{r}')\,dS' \\ & + \frac{1}{j\omega\epsilon} \int_{S^p} \nabla_s \cdot \mathbf{T}^p(\mathbf{r}) \int_{S^q} \nabla'_s \cdot \mathbf{J}^q(\mathbf{r}') G(\mathbf{r},\mathbf{r}')\,dS'\,. \end{aligned} \tag{3.21}$$

The integration domain S^p (S^q) is the domain where $\mathbf{T}^p$ ($\mathbf{B}^q$) is non-zero which includes one patch for patch functions and two patches for edge functions. The last equality in (3.21) was derived using the identity [92, p. 503]

$$\int_{S^p} \mathbf{T}^p \cdot \nabla\Phi \, dS = -\int_{S^p} \Phi \nabla_s \cdot \mathbf{B}^p \, dS, \tag{3.22}$$

where Φ is a scalar function. The general form of (3.22) is more complicated but $\mathbf{T}^p$ has no component normal to the surface S^p and the component perpendicular to the edges of S^p are zero. Equation (3.21) holds for a general set of basis functions and the integrals can be evaluated in the parametric coordinate system on each patch. For the particular case of the Legendre basis functions in (3.9), all required integrals can be written as linear combinations of the generic integral

$$I_1 = \iiiint P_c(s)P_d(t)P_m(u)P_n(v)\, a(s,t,u,v)\, G\big(\mathbf{r}(s,t), \mathbf{r}'(u,v)\big)\, dv\, du\, dt\, ds, \tag{3.23}$$

where $-1 \leq s,t,u,v \leq 1$. The polynomials $P_c(s)$, $P_d(t)$, $P_m(u)$, and $P_n(v)$ are the Legendre polynomials in (3.3) and $a(s,t,u,v)$ can be any of the combinations

$$a(s,t,u,v) = \begin{cases} \mathbf{a}_s(s,t) \cdot \mathbf{a}_u(u,v) \\ \mathbf{a}_s(s,t) \cdot \mathbf{a}_v(u,v) \\ \mathbf{a}_t(s,t) \cdot \mathbf{a}_u(u,v) \\ \mathbf{a}_t(s,t) \cdot \mathbf{a}_v(u,v) \\ 1 \end{cases} \tag{3.24}$$

The Jacobians $\mathcal{J}_s(s,t)$ and $\mathcal{J}_s(u,v)$ originating from the basis and testing functions are not needed in (3.23) since they are cancelled by the differential surface elements $dS = \mathcal{J}_s(s,t)ds\,dt$ and $dS' = \mathcal{J}_s(u,v)du\,dv$. The integrals in (3.23) can be evaluated using the Gauss-Legendre integration scheme (see appendix C.4) provided that the domains of the basis functions do not overlap. This special case will be considered below.

3.2.4 Self-Term Matrix Element Evaluation

The integrand in (3.23) contains an integrable singularity when the domains of the basis and testing functions overlap. The evaluation of these self-term matrix elements is often based on extraction of the singular part of the integrand which is then integrated analytically. However, in the case of higher-order basis functions and curved patches this approach is extremely tedious and leads to complicated expressions for the singular part of the integrand. A better choice is the purely numerical annihilation procedure that is based on the Duffy transform [93] and was applied to hexahedrals by Sertel and Volakis [94]. This procedure can be adapted to quadrilateral patches as described below.

Consider the generic integral

$$I_2 = \int_{-1}^{1}\int_{-1}^{1} f(u,v)G(u,v,u_0,v_0)du\,dv\,, \tag{3.25}$$

where f is a well-behaved arbitrary function and $G(u,v,u_0,v_0)$ is some other function with a first order singularity at $(u,v) = (u_0,v_0)$. The original integration domain is now mapped into four new domains, each with a vertex at (u_0,v_0), as illustrated in Figure 3.2. By using four different linear mappings, (3.25) can be cast into the form

$$I_2 = \sum_{i=1}^{4}\int_{0}^{1}\int_{0}^{1} f_i(\zeta,\eta)G_i(\zeta,\eta)J_i d\zeta\,d\eta\,, \tag{3.26}$$

where J_i is the Jacobian of the linear mapping. By applying the transformations $\zeta = \alpha^2$ and $\eta = \beta^2$, (3.26) becomes

$$I_2 = \sum_{i=1}^{4}\int_{0}^{1}\int_{0}^{1} f_i(\alpha^2,\beta^2)G_i(\alpha^2,\beta^2)J_i 4\alpha\beta d\alpha\,d\beta\,, \tag{3.27}$$

where G_i after the transformation has a second order singularity at $(\alpha,\beta) = (0,0)$. However, this singularity is canceled by the term $\alpha\beta$. Thus, the four integrands in (3.27) are all well-behaved and can be integrated using a standard Gauss-Legendre integration scheme. The annihilation procedure is an excellent tool for writing very general codes since the functions f and G are arbitrary. Thus, the same code can be used without modifications for a variety of basis functions and Green's functions. This is not possible with methods based on analytical singularity extraction.

The above transformation is directly applicable to the calculation of mixed-potential EFIE matrix elements. For the MFIE in (2.15), the dot products appearing in (2.16) are zero whenever the observation point is located in the plane of the surface current. However, problems may occur at sharp edges if the source and observation points are located on different patches but approach the sharp edge shared by the two patches. The gradient operator yields a $1/r^2$-singularity but the dot products do not cancel. The resulting strongly singular integrand requires that the annihilation procedure is used for neighboring patches as well. The original integration domain is then mapped into two new domains instead of four. The origin of these two domains is located on the sharp edge as close as possible to the observation point. Similar problems may occur if the MFIE is used to model thin plates with finite thickness. The annihilation procedure should therefore be used whenever the distance between the observation point and the integration domain is below some predefined limit.

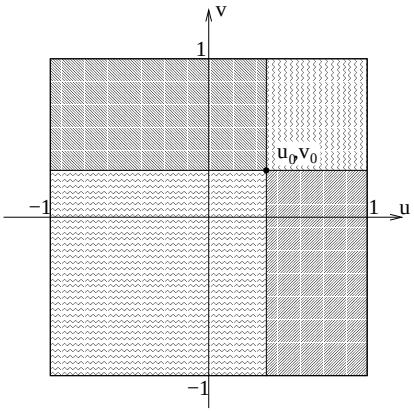

Figure 3.2: *Illustration of the annihilation procedure. The quadrilateral patch with a singularity at* (u_0, v_0) *is mapped into four smaller patches, each with a singularity at the origin.*

3.2.5 Triangles in a Quadrilateral Mesh

The geometrical modeling using generalized quadrilateral patches of arbitrary order can represent most objects with sufficient accuracy. However, it simplifies meshing of complicated structures if the MoM scheme allows a few triangular patches in a quadrilateral mesh. Introducing special basis functions on triangles would complicate the practical implementation significantly. Instead, the standard quadrilateral basis functions can be maintained if triangles are treated as degenerate quadrilaterals with two vertices collapsed into one. This possibility was also briefly discussed by Valle *et al.* [91] for rooftop functions. Naturally, the current component normal to an edge with zero length must be zero which can be enforced by treating the edge as an external edge. The u- and v-coordinate lines on such a degenerate quadrilateral are shown in Figure 3.3. It is observed that the three edges are not treated symmetrically since one current component flows between two edges whereas the other current component flows from a vertex to an edge. Numerical experiments have verified that this does not introduce numerical instabilities and that the accuracy is comparable to basis functions specifically defined on triangles. This shows that the results of Valle *et al.* [91] also holds for higher-order basis functions.

3.2.6 Generalization to Wires and Volumes

The basis functions defined in the (3.9) were given for surface patches. However, it is straightforward to generalize them to wires and volumes. Specifically, the current on a wire can be expanded as

$$I(u) = \sum_{m=0}^{M} b_m C_m^u \widetilde{P}_m(u) \ . \tag{3.28}$$

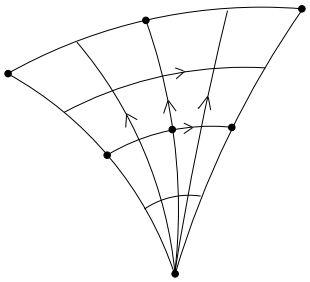

Figure 3.3: Coordinate lines on a 7-node second-order triangle represented as a degenerate 9-node second-order quadrilateral.

For a curvilinear hexahedral volume with the parametric coordinates (u, v, w), the electric flux density $\mathbf{D}$ can be written in terms of its contravariant components as

$$\mathbf{D}(u,v,w) = D^u \mathbf{a_u} + D^v \mathbf{a_v} + D^w \mathbf{a_w} \,, \tag{3.29}$$

where $\mathbf{a}_w = \frac{\partial \mathbf{r}}{\partial w}$ is the covariant unitary vector in the w-direction. A divergence-conforming expansion of the D^u component is then

$$D^u(u,v,w) = \frac{1}{\mathcal{J}(u,v,w)} \sum_{m=0}^{M^u} \sum_{n=0}^{N^v} \sum_{q=0}^{Q^w} b_{mnq} C_m^u \widetilde{P}_m(u)\, C_n^v P_n(v)\, C_q^v P_q(w) \,, \tag{3.30}$$

where $\mathcal{J}$ is the Jacobian

$$\mathcal{J} = \mathbf{a}_u \cdot \mathbf{a}_v \times \mathbf{a}_w \,. \tag{3.31}$$

The components D^v and D^w can be expanded in a similar way by interchanging (u, v, w) in a cyclic fashion. The basis functions for wires and volumes have the same favorable orthogonality properties as the surface functions in (3.9). Thus, they provide similar improvements of the condition number when compared to other higher-order expansions, e.g. [7, 11], which was recently verified by Kim *et al.* [42] for the volumetric Legendre basis function in (3.30).

All the basis functions presented above are divergence-conforming and allows to impose normal continuity of a vector quantity across element boundaries. Similar curl-conforming basis functions for imposing tangential continuity can be obtained by using the contravariant unitary vectors (see Appendix B). Such functions are suitable for FEM or volumetric integral equations with the electric field as the unknown.

3.3 Numerical results

This section presents numerical results aimed at demonstrating the favorable properties of the higher-order Legendre basis functions. First, the implementation is validated and the higher-order convergence is verified by comparison with the exact solution for a sphere. Next, the condition numbers of the MoM matrix obtained with the

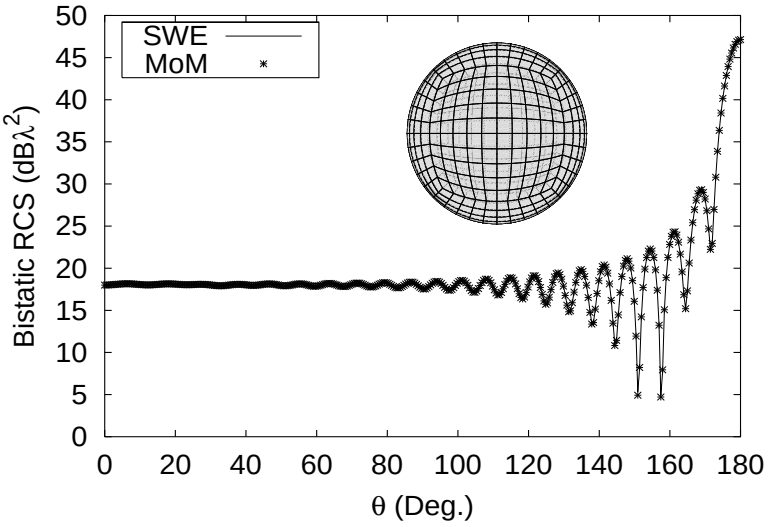

Figure 3.4: *Bistatic RCS of a 9λ diameter sphere. The exact SWE solution compared to the higher-order MoM solution obtained with third-order functions ($M = 3$, 10800 unknowns).*

higher-order Legendre basis functions are compared to condition numbers obtained with two existing types of higher-order basis functions.

3.3.1 Validation and Convergence

A PEC sphere is an excellent object for validation purposes since an exact solution exists. A sphere with 9λ diameter was chosen to allow comparison with the FMM results obtained by Donepudi *et al.* [95]. The CFIE must be used although the sphere is not exactly resonant. In fact, numerical investigations revealed that the accuracy of the EFIE is compromised by a high matrix condition number leading to irregular convergence. The sphere is discretized using second-order quadrilateral patches given by 9 points. These curved patches yield a fairly accurate approximation of the sphere surface, except for very coarse meshes with less than 200 patches. The CFIE is solved with equally weighted EFIE and MFIE parts ($\alpha = 0.5$) and a direct solver was used. The computed radar cross section (RCS) is compared to the exact RCS obtained from a spherical wave expansion[1] (SWE) [96]. Figure 3.4 displays the bistatic RCS in the E-plane for incidence from $\theta^i = 0^\circ$. The E-plane was chosen since the RCS exhibits a rapid variation which is more difficult to compute than the rather smoothly varying RCS in the H-plane. The MoM result was obtained using third-order functions ($M = M^u = M^v = 3$) and a mesh with 600 patches. This resulted in a total of 10800

[1]Mirza Karamehmedovic, Technical University of Denmark, is acknowledged for providing the exact results for the sphere.

Order of basis ⇒	1st ($M = 1$)		2nd ($M = 2$)		3rd ($M = 3$)	
Number of patches	Unk.	Dens.	Unk.	Dens.	Unk.	Dens.
294					5292	20
384					6912	27
486					8748	34
600			4800	18	10800	42
1014			8112	31	18252	71
1536			12288	48		
1944	3888	15	15552	61		
2904	5808	27	23232	91		
5400	10800	42				
7776	15552	61				
10584	21168	83				

Table 3.1: *Number of unknowns and density of unknowns per λ^2 for the 9λ diameter sphere.*

unknowns which corresponds to 42 unknowns per square wavelength. The MoM and SWE results seem to agree very well.

To study the accuracy in greater detail, the root-mean-square (RMS) error of the RCS is defined as

$$\text{RMS} = \sqrt{\frac{1}{N_s}\sum_{i=1}^{N_s}|\sigma_{SWE} - \sigma_{MoM}|^2} \tag{3.32}$$

where N_s is the number of sampling points (bistatic observation angles), and σ_{MoM} and σ_{SWE} are the computed and exact RCS measured in dB, respectively. The RMS error is defined as in [95] to facilitate a comparison. Table 3.1 lists the number of patches for 11 different meshes, the resulting number of unknowns, and the density of unknowns for first-, second-, and third-order basis functions. Figure 3.5 displays the RMS error as a function of the density of unknowns per square wavelength. The solid lines show the error of the MoM using the hierarchical Legendre basis functions on quadrilateral patches. It is observed that the error decays much faster when second-order functions are used instead of first-order functions. Thus, the desired higher-order convergence has been achieved. The third-order functions provide even higher accuracy although the slope of the curve seems to be almost the same as for the second-order curve. This probably indicates that the RMS error for the third-order functions is dominated by geometrical modeling errors. Specifically, only second-order quadrilateral patches were used to model the sphere and the third-order results were obtained using quite coarse meshes. This might result in second-order convergence even for the third-order basis functions. Nevertheless, it is important to emphasize that third-order basis functions and basis functions of much higher orders provide significant improvements if the surface curvature is smaller than for the present case.

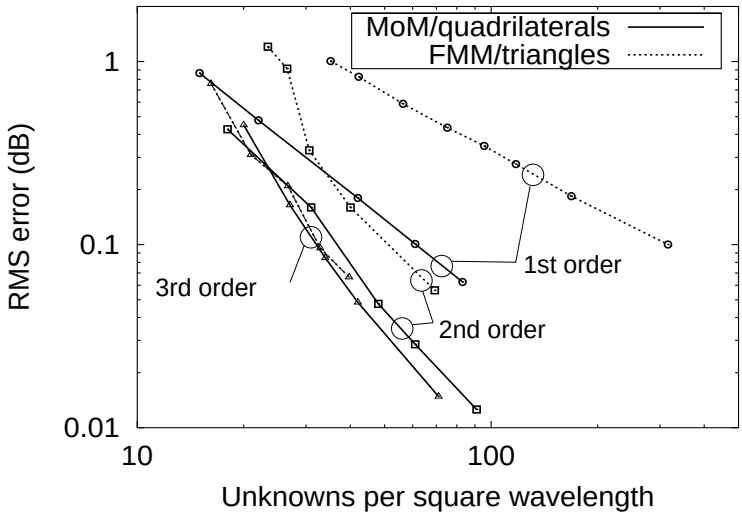

Figure 3.5: *E-plane RMS error for the bistatic RCS of a 9λ diameter sphere. The error for first- (circles), second- (squares), and third-order (triangles) basis functions are shown. The MoM using quadrilateral patches and hierarchical Legendre basis functions (solid lines) is compared to the MLFMM [95] using triangular patches and interpolatory basis functions (dashed lines).*

Figure 3.5 also displays the RMS error obtained by Donepudi *et al.* [95]. They used the interpolatory basis functions proposed by Graglia *et al.* [7] and second-order triangular patches in an MLFMM formulation. For first- and second-order functions, the error obtained with MLFMM and triangular patches is observed to be much higher than the error obtained with MoM and quadrilateral patches. This is probably caused by the approximations introduced in the MLFMM and the inherent redundancy of basis functions on triangular patches that use three vector components where only two are needed. The third-order curves are quite similar which, as mentioned above, might indicate that geometrical modeling errors are dominating. Donepudi *et al.* concluded that a 0.1 dB RMS error requires 80688 first-order functions, 14400 second-order functions, or 8400 third-order functions. The corresponding numbers required by the formulation presented here are approximately 15550, 8900, and 8300, respectively. Apparently, the difference between MoM and MLFMM seems to decrease as the expansion order increase. However, the data given in [95] for the memory consumption of the MLFMM indicates that the third-order result was obtained with only a marginal saving in memory compared to MoM. This suggests that the higher-order convergence of the MLFMM shown in Figure 3.5 was only obtained by increasing the accuracy of the multipole expansion along with the expansion order.

Pol. order M^u	2	3	4	5	6
Patch size (λ)	0.38	0.6	0.86	1.0	1.2
Unknowns	3968	3480	3024	3480	3480

Table 3.2: *Patch size and number of unknowns for the $6\lambda \times 6\lambda$parallel plates.*

3.3.2 Condition Numbers

The derivation of the new Legendre basis functions were aimed at obtaining a low condition number of the MoM matrix. To investigate this the MoM with Galerkin testing is applied to three simple PEC objects; these are two parallel plates, two parallel circular discs, and a pyramid. The condition number is higher when geometrical singularities such as corners and edges are present. Furthermore, the condition number is strongly affected by over-discretization. Thus, the geometrical objects are chosen to incorporate geometrical singularities with over-discretization to obtain a worst-case scenario. In each case, the condition number for increasing polynomial order is obtained. Further, to isolate the effect of increasing the polynomial order, the number of unknowns is kept constant, or slightly decreasing, by increasing the patch size along with the polynomial order. Results are presented for both EFIE and CFIE.

First, consider the two $6\lambda \times 6\lambda$ parallel plates with 1λ separation shown in the inset of Figure 3.6. The polynomial order is varied from $M = 2$ to $M = 6$ and the corresponding patch size and number of unknowns are listed in Table 3.2. To show the necessity of the scaling factors in (3.8), the Legendre basis functions are initially applied without these factors and the 2-norm EFIE condition number is computed. The hierarchical Legendre basis functions are compared to the hierarchical power basis functions of Kolundžija and Popović [6] and the interpolatory basis functions of Graglia *et al.* [7] which were based on Lagrange polynomials. The scaling factors given in [7] are also left out whereas no scaling factors were suggested in [6]. The condition numbers with all three types of basis functions are plotted in Figure 3.6. Clearly, the new hierarchical Legendre basis functions yield an almost constant condition number as the polynomial order increases. However, at the same time, the condition numbers obtained with the two existing types of basis functions grow rapidly, approximately one order of magnitude for each polynomial order.

When the appropriate scaling factors are introduced for the basis functions of [7] and the Legendre basis functions, the condition numbers improve. This is illustrated in Figure 3.7 for the same configuration as in Figure 3.6). The improvements due to the scaling factors are more pronounced for the interpolatory basis functions but the slope of the curve obtained with the hierarchical Legendre basis functions is still significantly lower than the slope of the two other curves.

The discussion on orthogonality in Section 3.2.1 was limited to rectangular or rhomboid shaped patches. To show that the favorable condition numbers are maintained for more general patch shapes, the three different kinds of basis functions are applied to two parallel discs with a diameter of 10λ and 1λ separation, as shown in the

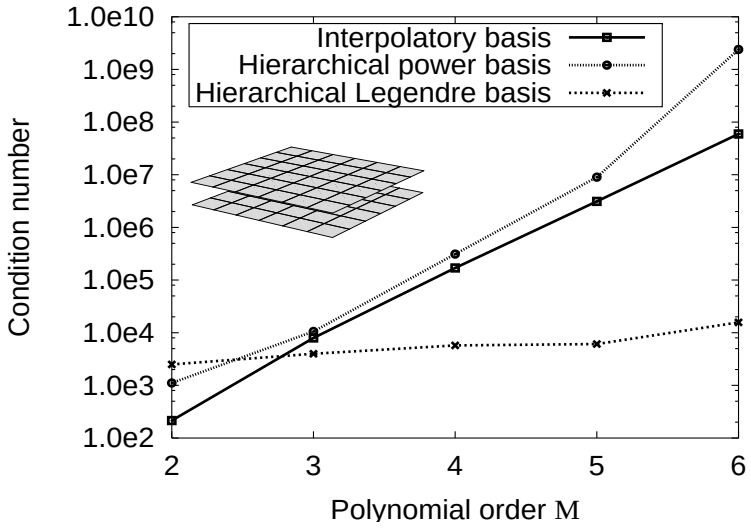

Figure 3.6: *Condition numbers for the $6\lambda \times 6\lambda$ parallel plates obtained using basis functions without scaling factors. The interpolatory basis functions of [7] are compared to the hierarchical power basis functions of [6] and the hierarchical Legendre basis functions.*

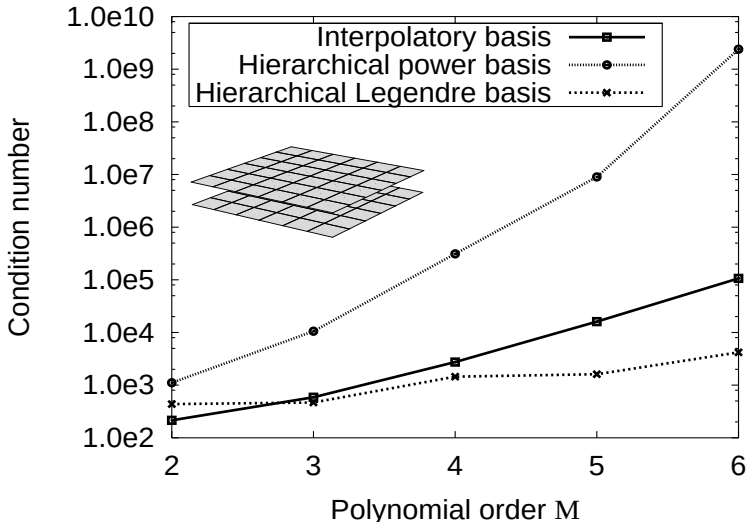

Figure 3.7: *Condition numbers for the $6\lambda \times 6\lambda$ parallel plates when scaling factors are included. The interpolatory basis functions of [7] are compared to the hierarchical power basis functions of [6] and the hierarchical Legendre basis functions.*

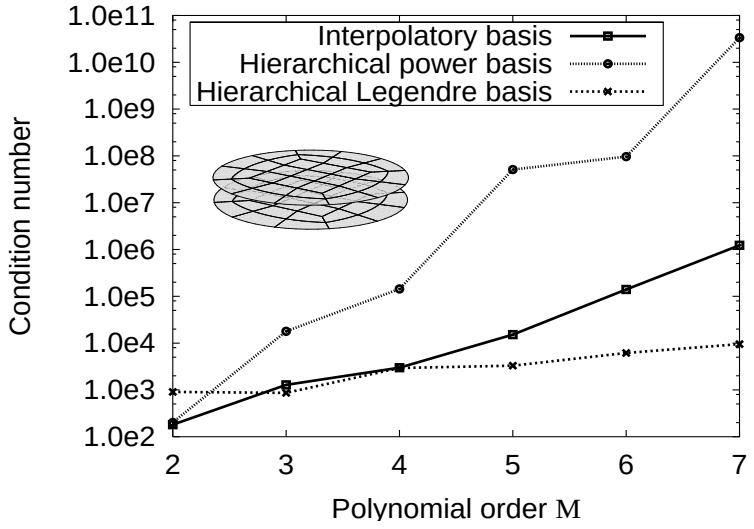

Figure 3.8: *Condition numbers for two parallel discs with diameter* 10λ *and* 1λ *separation. The interpolatory basis functions of [7] are compared to the hierarchical power basis functions of [6] and the hierarchical Legendre basis functions.*

Pol. order M^u	2	3	4	5	6	7
Average patch size (λ)	0.5	0.83	1.08	1.35	2.10	2.10
Unknowns	10200	7992	8400	8400	4680	6384

Table 3.3: *Average patch size and number of unknowns for the parallel discs.*

inset of Figure 3.8. The patches are 9-node quadrilaterals with curved edges and the average patch size and number of unknowns for varying polynomial order are listed in Table 3.3. The EFIE condition numbers are shown in Figure 3.8. Again, the hierarchical Legendre basis functions yield an almost constant condition number whereas the basis functions of [6] and [7] result in a rapidly growing condition number for increasing polynomial order. In fact, by increasing the polynomial order from 2 to 7 the condition number obtained with the interpolatory basis functions displays an increase by almost 4 orders of magnitude whereas the condition number obtained with the Legendre basis functions does not even increase by a factor of 10.

The EFIE, being a first-kind integral equation, always suffers more from ill-conditioning than the CFIE. Thus, the CFIE is preferable for closed structures such as the pyramid in Figure 3.9. A high condition number is expected for this object due to its sharp edges and the irregularly shaped patches. The condition number obtained with $M = 4$, 5, and 6 are listed in Table 3.4 for the hierarchical Legendre basis functions and for the interpolatory basis functions [7]. Clearly, for the CFIE the growth in

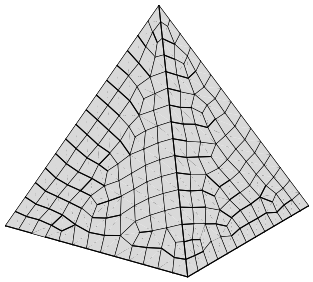

Figure 3.9: *Mesh of a pyramid with side length* 10λ.

Pol. order M		4	5	6
Average patch size (λ)		0.8	1.2	1.2
Unknowns		18656	11800	16992
Cond. number	This work	425	724	1332
	[7]	1547	7680	79846

Table 3.4: *Average patch size, number of unknowns, and the resulting CFIE condition number for the pyramid.*

condition number with increasing polynomial order is much lower than that of the EFIE. Nevertheless, the hierarchical Legendre basis functions provide much lower condition numbers than the interpolatory basis functions.

3.4 Summary

A new set of higher-order hierarchical Legendre basis functions were developed and expressions of the basis functions for wires, surfaces, and volumes were given. The new basis basis functions are constructed by using orthogonal Legendre polynomials as the starting point. These polynomials are modified in a way that preserves almost perfect orthogonality while enforcing continuity of the normal current component flowing between neighboring patches. As a result of this procedure, the surface charge is implicitly expanded in orthogonal functions. The favorable orthogonality properties of the basis functions result in a low condition number of the MoM matrix. This was confirmed by numerical experiments that also verified that the new basis functions provide a much better condition number than available higher-order hierarchical and higher-order interpolatory basis functions. At the same time, the new higher-order Legendre basis functions can easily be computed for arbitrary orders and are very flexible to apply due to their hierarchical property. Thus, the new basis functions appear to have all the advantages of existing higher-order basis functions and none of their disadvantages. Finally, it was verified through comparisons with exact results for a sphere that the present implementation provides excellent accuracy and that the expected higher-order convergence is achieved.

Chapter 4
Iterative Solution of Higher-Order MoM Systems

The MoM leads to the matrix equation

$$\bar{\mathbf{Z}}\mathbf{I} = \mathbf{V}\,, \tag{4.1}$$

where the impedance matrix $\bar{\mathbf{Z}}$ is generally non-symmetric, complex, and fully populated. This chapter investigates how an efficient iterative solution of the matrix equation (4.1) is achieved. Four key issues can be identified to reach this goal:

1. The continuous operator equation must produce a well-conditioned matrix.
2. The discretization scheme must produce a well-conditioned matrix. The choice of basis functions and testing functions in MoM is therefore crucial.
3. An efficient preconditioner must be applied. The convergence speed of iterative solvers can be improved by multiplying (4.1) with an additional matrix, preferably as close to $\bar{\mathbf{Z}}^{-1}$ as possible. This leads to the preconditioned system
$$\bar{\mathbf{P}}\bar{\mathbf{Z}}\mathbf{I} = \bar{\mathbf{P}}\mathbf{V} \quad \text{where} \quad \bar{\mathbf{P}} \approx \bar{\mathbf{Z}}^{-1}\,. \tag{4.2}$$
4. An fast and robust iterative solution algorithm must be applied.

This chapter begins with a survey of existing works and Section 4.2 then deals with the second issue above. Specifically, an attempt is made to improve convergence by leaving the current and charge as independent unknowns. Issue 3 above is treated in Sections 4.3 and 4.4 that present various preconditioners for higher-order MoM. Finally, the numerical results presented in Section 4.5 illustrate the performance of the preconditioners in conjunction with various iterative solution algorithms.

4.1 Survey

The application of conjugate gradient (CG) methods in CEM was first investigated during the eighties. Sarkar *et al.* [21, 22] and Peterson and Mittra [23] applied the CG to solve the normal equations (see Appendix D.2.9) since general MoM matrices are not symmetric and positive definite as required by CG. The simplicity of the CG

method allows for estimating an upper bound on the number of iterations required to achieve a certain accuracy. Several authors presented such iteration bounds, including Woodworth and Yaghjian [66], Sarkar *et al.* [21, 22], and Peterson and Mittra [23]. These works proved that MoM systems can be solved significantly faster by applying an iterative method rather than a direct method.

During the late eighties and early nineties, several new advanced iterative methods were developed. These new methods belong to the class of methods known as Krylov subspace methods which are described in Appendix D. Particularly, the GMRES of Saad and Schultz [97], the CGS by Sonneveld [98], the BICGSTAB by Van der Vorst [99], and the TFQMR by Freund [100] are appropriate candidates for the non-symmetric systems encountered in MoM. Despite the use of these advanced mathematical tools, iterative methods do not always provide stable and efficient solutions to MoM problems. This has spawned a lot of work in CEM to improve the formulations and develop appropriate preconditioners as described below.

4.1.1 Analytical Improvements of Condition Numbers

One way to improve the convergence of iterative methods is to change the underlying continuous problem. This implies that a second-kind integral equation should be preferred over a first-kind integral equation. The method of analytical regularization is a systematic approach for converting a first-kind integral equation into a second-kind integral equation. Several authors have applied this technique to practical problems and an overview was given by Nosich [101]. The second-kind integral operator is obtained by extracting an analytically invertible singular part of the original integral operator. This inverted operator is then used as an analytical preconditioner which leads to a second-kind integral equation. There are apparently three ways of selecting the invertible part to extract; the static part, the high-frequency part, or the part corresponding to a canonical shape. The major drawback of analytical regularization is the need for inverting the extracted part of the integral operator analytically. This makes it difficult, if at all possible, to develop algorithms that work for general objects.

Another recent method that can be viewed as an analytical preconditioner was proposed by Adams and Brown [102]. It is based on the observation made by Hsiao and Kleinman [56] that the EFIE operator working on itself produces a second kind integral equation involving a bounded operator. However, the matrix fill time increases dramatically due to the extra integrals required by the composite operator. Nevertheless, the fill time is acceptable if the Nyström method is used. This approach was used by Contopanagos *et al.* [103] in a CFIE solution for closed structures. However, the dual-surface MFIE by Woodworth and Yaghjian [66] provides a shorter matrix fill-time and has the same features as the analytically preconditioned CFIE. The work of Adams and Brown [102] is therefore better justified by its potential to produce a well-conditioned integral equation applicable to open objects.

4.1.2 Preconditioners for Low-Order Basis Functions

Multiplying the matrix equation with a preconditioning matrix as in (4.2) is probably the most common way of improving convergence. The matrix $\bar{\mathbf{P}}$ is often obtained by inverting a small but important part of $\bar{\mathbf{Z}}$. For CEM applications, $\bar{\mathbf{P}}$ is nearly always obtained by inverting the part of $\bar{\mathbf{Z}}$ corresponding to near-neighbor interactions. There are, however, several ways to obtain such preconditioners.

A particularly simple preconditioner is the diagonal preconditioner considered by Davidson and McNamara [104]. $\bar{\mathbf{P}}$ is obtained by taking the reciprocal values of the diagonal elements of $\bar{\mathbf{Z}}$. However, Davidson and McNamara demonstrated for a body of revolution that the diagonal preconditioner actually slowed the convergence. A better and still simple preconditioner is possible if the object comprises several spatially separated subdomains. A block-diagonal preconditioner is then obtained by inverting the part of $\bar{\mathbf{Z}}$ belonging to each subdomain. Such preconditioners have been independently developed by Bürger *et al.* [105], von Hagen and Wiesbeck [106, 107], and Poirier *et al.* [108]. Also related to those preconditioners is the generalized forward-backward method by Pino *et al.* [109] that has been applied to rough-surface scattering. A more appropriate preconditioner is desirable if the object does not comprise spatially separated subdomains. Yaghjian [110] used a banded version of $\bar{\mathbf{Z}}$ to construct a preconditioner for 2D applications. In 3D it is next to impossible to order the basis functions such that all matrix elements corresponding to near-neighbor interactions are close to the diagonal. However, Poirier *et al.* [108] considered a 3D preconditioner based on a banded matrix. A similar preconditioner that captures more near-neighbor interactions was proposed by Xie *et al.* [111] but required a small matrix system to be solved for each basis function.

The near-neighbor concept is also used in the incomplete LU (ILU) decomposition where the preconditioner is obtained by imposing a certain sparsity pattern on $\bar{\mathbf{Z}}$ and computing a LU decomposition of this "incomplete" matrix. The two banded-matrix preconditioners [108, 110] mentioned above can be seen as a special case of an ILU preconditioner. A more general sparsity pattern can be obtained by thresholding the matrix as proposed by Heldring *et al.* [112]. Thresholding was also used by Prakash and Mittra [113, 114] in a multi-frontal preconditioner that enable general sparsity patterns with low computational overhead. Thresholding can be avoided by ordering basis functions in groups. This latter approach was used by Sertel and Volakis [115] that used the near field portion of a FMM matrix to obtain the sparsity pattern. A similar sparsity pattern was used by Brüning *et al.* [116] and Rahola [117] but they formulated sparse approximate inverse (SPAI) preconditioners. SPAI preconditioners attempt to minimize the matrix norm $\|\bar{\mathbf{P}}\bar{\mathbf{Z}} - \bar{\mathbf{I}}\|$ where $\bar{\mathbf{I}}$ is the identity matrix. This requires that a large number of least-squares problems are solved but the resulting preconditioner is very robust. A SPAI preconditioner using thresholding was presented by Galléon *et al.* [118] and a SPAI preconditioner using the sparsity pattern of a MLFMM near field matrix was suggested by Zhang *et al.* [119]. An additional feature of SPAI preconditioners is that they are easy to implement for parallel execution on distributed memory systems. In contrast to this, ILU preconditioners are not easily parallelized [24].

Another family of preconditioners is related to wavelet methods. Canning and Scholl [120] used the wavelet transform to transform a standard MoM matrix into a sparse matrix that was preconditioned with a diagonal matrix. Recently, Deng and Ling [121] avoided using the wavelet transform by obtaining the preconditioner directly from a wavelet basis. Only 2-D results were presented in [120, 121].

4.1.3 Preconditioners for Higher-Order Bases

Apparently, only very few authors have attempted to solve a higher-order MoM system iteratively. The reason for this is most likely the ill-conditioned matrix systems obtained with conventional higher-order basis functions (see Section 3.3). The performance of iterative methods was studied by Kolundžija and Sarkar [20] for the case of higher-order power basis functions developed by Kolundžija and Popović [6]. The study revealed that the use of higher-order basis functions significantly reduces the efficiency of iterative solvers. For the case of a sphere which is well-conditioned due to the lack of geometrical singularities, the iterative and the direct method performed equally well when fourth-order basis functions were used. No results were presented for basis functions of orders higher than four. The study by Kolundžija and Sarkar [20] clearly demonstrated the need for an efficient preconditioner for higher-order basis functions.

Preconditioners for low-order MoM systems can, to some extent, also be applied to higher-order systems. It is apparent from Section 4.1.2 that virtually all preconditioners are based on the concept of near-neighbor interactions. For higher-order basis functions, the number of near-neighbor interactions can be very large which may compromise the efficiency of near-neighbor preconditioners for higher-order systems.

Recently, there has been some interest in additive Schwarz Preconditioners when used in conjunction with hierarchical basis functions. Therefore, additive Schwarz preconditioners will be described in Section 4.3. Stephan and Tran [122] presented a preconditioner for a 2D problem. However, the problem was already well-conditioned and the improvement by applying the preconditioner was not clear. Heuer considered a static problem in [123] and a time-harmonic problem in [124]. The latter work considered a planar plate and theoretical bounds for the condition number of the preconditioned matrix were proven. However, these bounds were derived under rather restrictive assumptions which will be further explained in Section 4.3.2.

4.2 Independent Charge and Current

This section investigates a non-conventional integral equation for PEC objects. As suggested by Volakis and Sancer [125], the electric surface current density and surface charge density can be used as independent unknowns. This approach increases the number of unknowns but might also lead to a matrix equation more amenable for solving with iterative methods. The rationale behind this idea can be found in the FEM literature. Some authors, e.g. Dyczij-Edlinger and Biro [126], use both scalar and vector potentials as unknowns in their FEM scheme. This formulation provides much faster convergence than conventional formulations using the electric field as the

only unknown. This suggests that it is advantageous to solve separately for a vector quantity (the vector potential) and its divergence (the scalar potential). An equivalent approach for surface integral equations is investigated below.

4.2.1 Charge Augmented Electric Field Integral Equation

Leaving the charge as an independent unknown in the EFIE increases the number of unknowns by a factor $3/2$. Thus, it is not sufficient to enforce the boundary condition on the tangential electric field since this would lead to an under-determined matrix system. To provide the extra equations needed, it seems natural to enforce also the boundary condition on the normal component of the electric field as it was done by Yaghjian [61] in the augmented EFIE (AEFIE). The AEFIE was intended to remove interior resonance problems of closed objects but is also applicable for the present purpose. Leaving the charge as an independent unknown leads to the two coupled equations,

$$\hat{\mathbf{n}} \times \mathbf{E}^i(\mathbf{r}) = \hat{\mathbf{n}} \times \left(j\omega\mu \int_S \mathbf{J}_s(\mathbf{r}') G(\mathbf{r}, \mathbf{r}')\, dS' + \frac{1}{\epsilon} \fint_S \rho_s(\mathbf{r}') \nabla G(\mathbf{r}, \mathbf{r}')\, dS' \right), \tag{4.3a}$$

$$\hat{\mathbf{n}} \cdot \mathbf{E}^i(\mathbf{r}) = \hat{\mathbf{n}} \cdot \left(j\omega\mu \int_S \mathbf{J}_s(\mathbf{r}') G(\mathbf{r}, \mathbf{r}')\, dS' + \frac{1}{\epsilon} \fint_S \rho_s(\mathbf{r}') \nabla G(\mathbf{r}, \mathbf{r}')\, dS' \right) + \frac{\rho_s(\mathbf{r})}{2\epsilon}. \tag{4.3b}$$

The result of Appendix A.1 was used to derive this equation and the bar on the integral signs indicates that the point $\mathbf{r}' = \mathbf{r}$ is excluded from the integration. In the conventional EFIE and AEFIE, the continuity equation $j\omega\rho_s = -\nabla_s \cdot \mathbf{J}_s$ is used to eliminate the unknown ρ_s. The scalar equation (4.3b) is not needed in the EFIE and used to over-determine the system in the AEFIE. Here, ρ_s is kept as an unknown and both (4.3a) and (4.3b) are needed. These coupled equations will be referred to as the charge AEFIE (CAEFIE). The CAEFIE is derived by letting the observation point approach the surface of the object from the exterior side. The interior CAEFIE would imply a sign change in analogy with the MFIE and the CAEFIE is only applicable to closed surfaces.

4.2.2 Discretization of the CAEFIE

The CAEFIE in (4.3) is discretized with MoM using the higher-order hierarchical Legendre basis functions. Specifically, the surface current density $\mathbf{J}_s$ is expanded in

terms of the vector basis functions implicitly defined in (3.1) and (3.9), i.e.,

$$\mathbf{J}_s(u,v) = \frac{1}{\mathcal{J}_s(u,v)} \Bigg(\mathbf{a}_u \sum_{m=0}^{M^u} \sum_{n=0}^{N^v} b^u_{mn} C^u_m \widetilde{P}_m(u)\, C^v_n P_n(v) + \mathbf{a}_v \sum_{m=0}^{M^v} \sum_{n=0}^{N^u} b^v_{mn} C^u_m \widetilde{P}_m(v)\, C^v_n P_n(u) \Bigg) , \tag{4.4}$$

where all quantities are defined as in Section 3.2.1. The unknown coefficients are b^u_{mn} and b^v_{mn} for the u- and v-directed currents, respectively. The expansion orders are chosen as $N^u = M^u - 1$ and $N^v = M^v - 1$ as discussed in Section 3.2.2. The surface charge density is expanded as

$$\rho_s(u,v) = \frac{1}{\mathcal{J}_s(u,v)} \sum_{m=0}^{N^u} \sum_{n=0}^{N^v} c_{mn} C^v_m P_m(u)\, C^v_n P_n(v) , \tag{4.5}$$

where c_{mn} are unknown coefficients for the charge. The Galerkin scheme is chosen for testing. That is, the vectorial equation (4.3a) is tested with the vectorial functions in (4.4) and the scalar equation (4.3b) is tested with the scalar functions in (4.5). The gradient operator in the vectorial equation (4.3a) can be transferred to the testing functions as it is done for the mixed-potential EFIE. This is not possible for the scalar equation (4.3b) which leaves a strongly singular kernel. Extreme care must be taken when computing the matrix elements, particularly in the vicinity of edges. The annihilation procedure was used for the self-terms and neighboring patches as described in Section 3.2.3.

4.2.3 Numerical Results for the CAEFIE

The validity of the CAEFIE formulation is now demonstrated with a numerical example. The $3\lambda \times 3\lambda \times 3\lambda$ cube shown in Figure 4.1 is located with one vertex at the origin of a rectangular coordinate system and illuminated by a plane wave incident from the direction specified by ($\theta^i = 45°$, $\phi^i = 0°$). The incident magnetic field is polarized in the y-direction. A closed curve ABCDA is located in the plane defined by $(x, y = \frac{3}{2}\lambda, z)$ and the coordinate along the curve is denoted t. The $\hat{\mathbf{t}}$-component of the surface current density is then obtained with the EFIE and CAEFIE using $\lambda/2 \times \lambda/2$ patches and a third order expansion ($M^u = M^v = 3$). This results in 3888 unknowns for the EFIE and 5832 unknowns for the CAEFIE. The real and imaginary parts of the normalized surface current are shown in Figure 4.2. The EFIE and CAEFIE are in close agreement except for the small discrepancies at point C and in vicinity of points B and D. It was carefully checked that those discrepancies are not caused by lack of accuracy in the numerical integrations performed during the matrix fill. However, the EFIE and CAEFIE are different operators and the current is projected onto different finite-dimensional function spaces. Consequently, the two solutions need not to be identical.

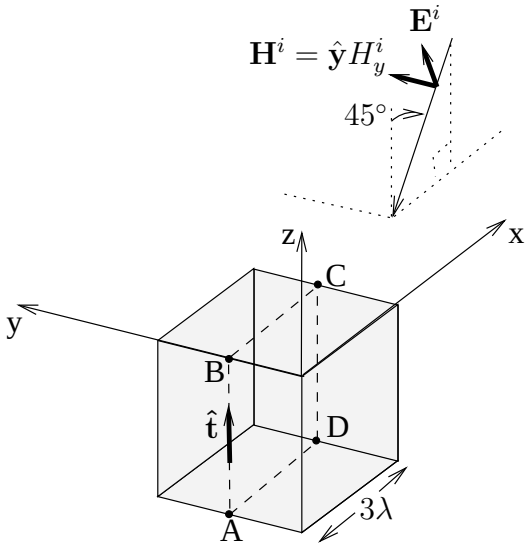

Figure 4.1: $3\lambda \times 3\lambda \times 3\lambda$ *PEC cube illuminated by a plane wave with* $\hat{\mathbf{y}}$*-polarized magnetic field. The direction of incidence forms a* $45°$ *angle with the* $\hat{\mathbf{z}} - axis$*. The points A, B, C, and D define a closed curve denoted ABCDA.*

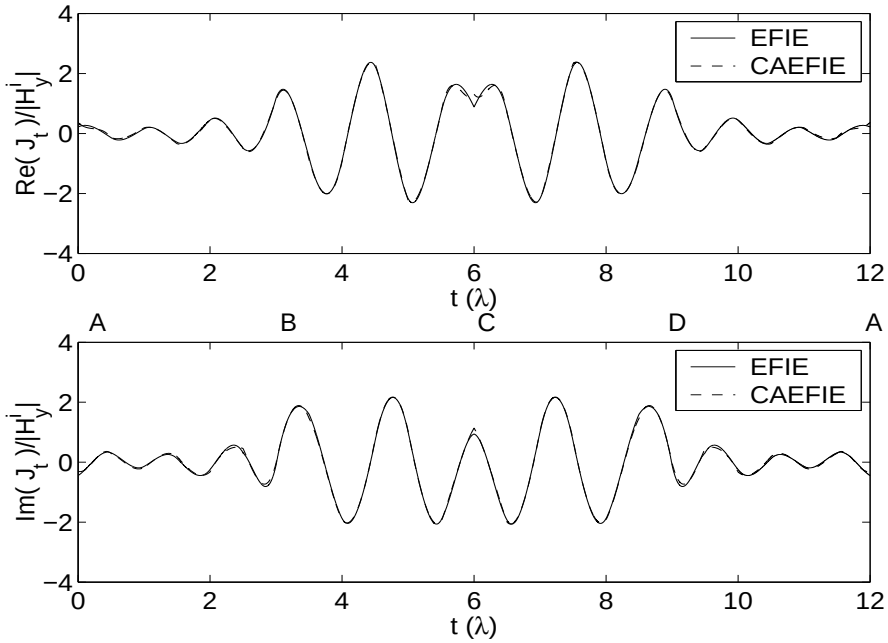

Figure 4.2: *Real and imaginary part of the normalized surface current density (*$\hat{\mathbf{t}}$*-component). The coordinate* t *is measured along the curve ABCDA shown in Figure 4.1.*

The derivation of the CAEFIE was motivated by the possibility of improving convergence of iterative solvers. To investigate this possibility, the condition number is computed for a cube discretized using 600 square patches and first order functions ($M^u = M^v = 1$). The frequency is varied over a small interval corresponding to varying the cube side length from $\lambda/2$ to $3\lambda/2$. This curve is therefore comparable to Figure 2.1. The condition number obtained with EFIE and CAEFIE is shown in Figure 4.3 (logarithmic scale). Clearly, the CAEFIE yields a much higher condition number than the conventional EFIE. This disappointing result leaves little hope that current and charges as independent unknowns are feasible in the MoM. At least, the CAEFIE and the discretization scheme outlined here are not appropriate. Figure 4.3 also reveals that the CAEFIE has homogeneous solutions at some of the cavity resonance frequencies. A closer look confirmed that cavity modes with a constant field along one direction, i.e. cavity modes with a zero as one of the mode numbers, are not homogeneous solutions to the CAEFIE while all other cavity modes are. However, the CAEFIE was abandoned due to the poor condition numbers and a rigorous explanation of the resonance problem was not pursued.

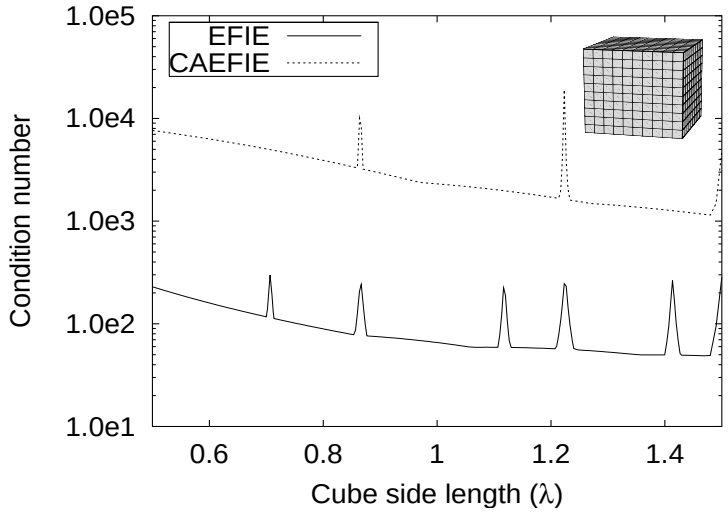

Figure 4.3: *Condition numbers of MoM matrix for increasing electrical size of cube.*

4.3 Additive Schwarz Preconditioners

The Schwarz procedure is an iterative domain decomposition method [24]. The domain of a given problem is decomposed into a number of subdomains and the local solution on each subdomain is used to find the solution on the original domain. Several variants of this method exist but only the so-called additive Schwarz method is considered below. Specifically, it is considered how the Schwarz method can be used to define a preconditioner for the matrix equation (4.1).

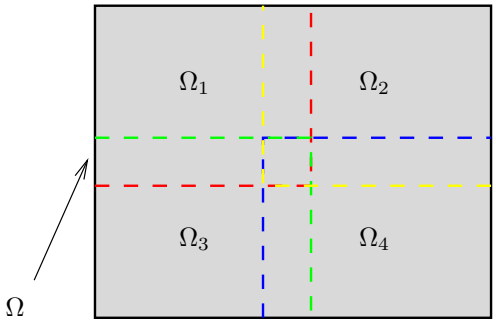

Figure 4.4: *Domain Ω divided into four overlapping subdomains. Ω_1 is bounded by the red curve, Ω_2 by the yellow curve, Ω_3 by the green curve, and Ω_4 by the blue curve.*

Consider the domain Ω shown in Figure 4.4. Ω is divided into four, possibly overlapping, subdomains Ω_i, $i = 1, 2, 3, 4$. Assume that n_i basis functions are defined on Ω_i and that the total number of basis functions is n. Let $\bar{\mathbf{R}}_i$ denote a $n_i \times n$ matrix that maps a vector $\mathbf{v}$ from Ω onto a vector $\mathbf{v}_i$ that only contains the elements belonging to Ω_i. That is, $\bar{\mathbf{R}}_i$ contains only zeros and ones and $\mathbf{v}_i = \bar{\mathbf{R}}_i\mathbf{v}$. The matrix $\bar{\mathbf{R}}_i$ is a restriction operator that restricts a vector in Ω to a vector Ω_i. The transpose $\bar{\mathbf{R}}_i^T$ is then a prolongation operator which takes a vector in Ω_i and extends it into Ω. Assume that a physical problem is governed by a matrix equation involving the matrix $\bar{\mathbf{Z}}$. The matrices governing the local problem on each subdomain are then found as $\bar{\mathbf{Z}}_i = \bar{\mathbf{R}}_i\bar{\mathbf{Z}}\bar{\mathbf{R}}_i^T$. $\bar{\mathbf{Z}}_i$ is relative small and $\bar{\mathbf{Z}}_i^{-1}$ can be computed within reasonable time. The additive Schwarz method provides a solution to the original problem through the iterative procedure

$$\mathbf{I}_{new} = \mathbf{I} + \sum_i \bar{\mathbf{R}}_i^T\bar{\mathbf{Z}}_i^{-1}\bar{\mathbf{R}}_i\left(\mathbf{V} - \bar{\mathbf{Z}}\mathbf{I}\right). \tag{4.6}$$

In words, the Schwarz procedure takes the residual of the original equation, restricts it to the subdomains, finds the solution on each subdomain, and extends it into the original domain. The global solution is then updated with the sum of the local solutions.

The iterative procedure described above is rather slow if used to solve (4.1). However, the Schwarz procedure can be used as a preconditioner for a Krylov subspace method. The preconditioning matrix is then given by

$$\bar{\mathbf{P}} = \sum_i \bar{\mathbf{R}}_i^T\bar{\mathbf{Z}}_i^{-1}\bar{\mathbf{R}}_i. \tag{4.7}$$

This matrix is never computed explicitly since it would be very time and memory consuming. The restriction and prolongation operators are not implemented as matrix operators. Specifically, applying the restriction operator simply corresponds to picking the vector elements belonging to a specific subdomain. Similarly, applying the prolongation operator corresponds to putting the elements back in their correct

position in the global vector. Thus, only the LU decompositions of the local matrices $\bar{\mathbf{Z}}_i$ need to be stored. The matrix-vector product $\mathbf{x} = \bar{\mathbf{P}}\mathbf{v}$ required by the Krylov subspace method is then computed through the following steps:

1. Do for all i subdomains
2. Form $\mathbf{v}_i$ by taking the elements of $\mathbf{v}$ belonging to Ω_i (restriction)
3. Compute $\mathbf{x}_i = \bar{\mathbf{Z}}_i^{-1}\mathbf{v}_i$ (forward and backward solve using a stored LU decomposition of $\bar{\mathbf{Z}}_i$).
4. Add the elements of $\mathbf{x_i}$ to the proper elements of $\mathbf{x}$ (prolongation)
5. End do

The above algorithm is easy to implement for parallel execution since each subdomain is handled independent of the others.

So far nothing has been said about the subdomains Ω_i. Two possible choices are described below. First, decomposition of the physical space leads to a near-neighbor preconditioner. Second, decomposition of the polynomial space leads to a preconditioner tailored to higher-order hierarchical basis functions.

4.3.1 Physical Space Decomposition

Most existing preconditioners mentioned in Section 4.1.2 are based on a near-neighbor concept and the same concept can be applied in an additive Schwarz preconditioner. The surface of the physical object is then discretized using curvilinear patches and these patches are collected into groups of nearby patches. This is illustrated in Figure 4.5(a) where the patches used to model a sphere are located in 90 different groups. The groups then define the domains Ω_i. That is, all basis functions defined on the patches belonging to group i are in Ω_i. However, the edge basis functions in (3.9) span two patches. Such basis functions may belong to two groups and the domains are overlapping. The resulting preconditioner will be referred to as an overlapping group preconditioner. Alternatively, the overlapping domains can be avoided by randomly placing basis functions belonging to two groups in one of the groups. This type of preconditioner will be referred to as a group preconditioner and is equivalent to several of the existing preconditioners mentioned in Section 4.1.2, e.g., those of [105]-[108]. In contrast to this, the overlapping group preconditioner is different from any of the preconditioners mentioned in Section 4.1.2.

The difference between overlapping and non-overlapping domains is negligible when the patches are small. Thus, overlapping domains are not required for low-order basis functions. However, overlapping domains are important when large patches are used. Therefore, the overlapping group preconditioner can be seen as a natural extension of the works [105]-[109] and [115] to account for the larger patches used by higher-order basis functions. Figure 4.6(a) and 4.6(b) illustrate the matrix structure of the group preconditioner and the overlapping group preconditioner, respectively. It is noted that the size of the groups does not increase as the size of the object increases; only the number of groups is increased.

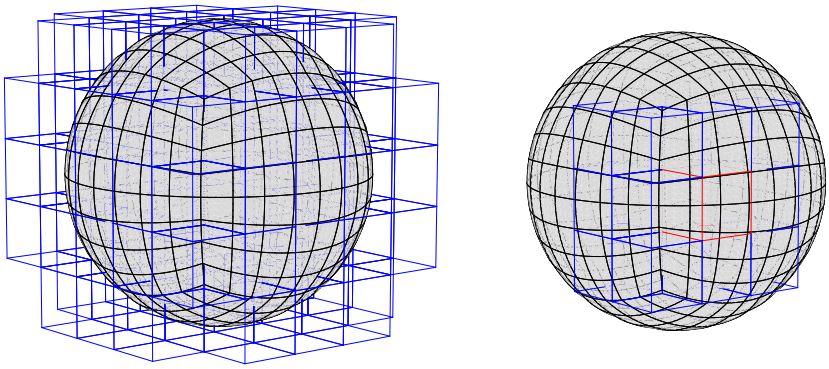

(a) (b)

Figure 4.5: *A sphere modeled by 384 curved patches. The patches are divided into 90 groups and the borders of the groups are shown with blue lines in (a). In (b), a single group is shown with red lines. The 11 neighboring groups sharing at least one vertex with the red group are shown with blue lines.*

4.3.2 Polynomial Space Decomposition

Additive Schwarz preconditioners with polynomial space decomposition were suggested for hierarchical basis functions by Stephan and Tran [122] and Heuer [123, 124]. More precisely, the preconditioners employed a combination of polynomial and physical space decomposition. However, the basis functions used in those works did not enforce continuity of the normal current component between neighboring patches. Consequently, the domain decomposition applied in [122]-[124] is not appropriate for edge functions possibly spanning two patches. Instead, the basis functions defined in (3.10) can be divided following these rules:

1. Edge functions with $m = 0, 1$ and $n = 0$, i.e. all rooftops, belong to the domain Ω_0. This domain only includes low-order functions and is usually referred to as the coarse problem.

2. Patch functions with $m \geq 2$ are only defined on a single patch. Each patch defines a domain Ω_i, $i = 1, 2, \ldots, N^p$ with N^p being the number of patches.

3. Edge functions with $m = 0, 1$ and $n > 0$ are defined on two patches. These functions belong to two of the domains introduced in 2. Thus, the domains Ω_i, $i = 1, 2, \ldots, N^p$ are overlapping.

These rules imply a combined polynomial and physical space decomposition and lead to an overlapping additive Schwarz preconditioner that are only applicable to higher-order hierarchical basis functions. In the following, this preconditioner is simply referred to as the Schwarz preconditioner. Theoretical bounds for the condition number

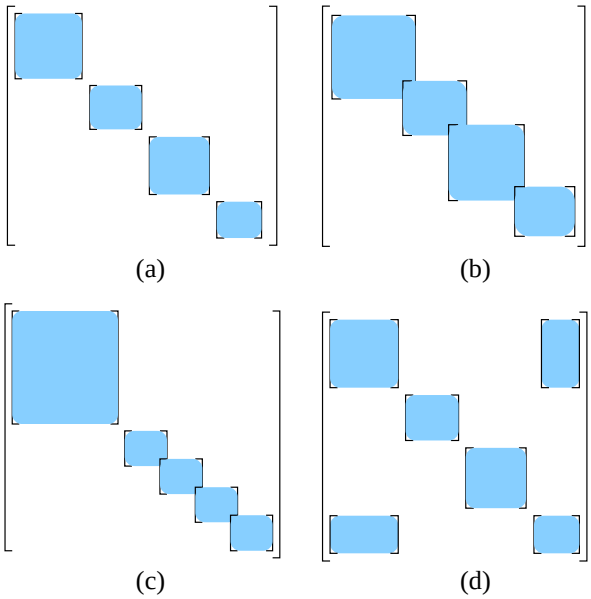

Figure 4.6: *Matrix structure of four different preconditioners. The group preconditioner in (a) is a block-diagonal preconditioner with blocks in different sizes. The overlapping group preconditioner in (b) allows basis functions to be in two groups which results in overlapping blocks. Note that (b) illustrates the simple case where each group only has two neighbors. In general, the overlap can be more complicated. The Schwarz preconditioner in (c) is based on polynomial space decomposition and has one large block containing all low-order functions and one small group for each patch containing all higher-order functions. The ILU preconditioner in (d) includes all interactions within the individual group and with its neighbors.*

of the preconditioned matrix system were proven by Heuer [124]. These bounds were derived under quite restrictive assumptions which are not fulfilled by hierarchical Legendre basis functions. Most importantly, it was assumed in [124] that the domains Ω_i are not overlapping and that the coarse problem is well-posed. This latter assumption generally restricts the maximum size of the patches to $\lambda/2$ [127]. Nevertheless, good performance might still be possible despite the violated assumptions.

The matrix structure of the Schwarz peconditioner is illustrated in Figure 4.6(c). One inherent disadvantage is large size of the coarse problem which grows with the size of the object. Also, this coarse problem is not readily solved in parallel.

4.4 Incomplete LU Preconditioner

ILU preconditioners have been described by several authors, e.g., Saad [24]. As the name suggests, the preconditioner is obtained by performing an LU factorization of the matrix $\bar{\mathbf{Z}}$ but leaving out some matrix entries in predetermined locations. The location of elements that are left out can be found by thresholding the elements of $\bar{\mathbf{Z}}$ which leads to a quite complicated sparsity pattern of the preconditioning matrix $\bar{\mathbf{P}}$. This is inconvenient since it is hard to store $\bar{\mathbf{P}}$ without overhead if the non-zero elements are randomly distributed throughout $\bar{\mathbf{P}}$. It is more convenient to impose a fixed sparsity pattern on $\bar{\mathbf{P}}$. This fixed pattern should allow all matrix elements resulting from near-neighbor interactions to be included in the ILU decomposition. This can be achieved if the object under consideration is divided into groups as in Figure 4.5(a). The sparsity pattern is then obtained by including all matrix elements resulting from interactions within each group as well as interactions with all neighboring groups. Neighboring groups are defined here as those groups sharing at least one vertex, as illustrated in Figure 4.5(b). Therefore, each group might have up to 26 neighbors. The matrix structure of the ILU preconditioner is illustrated in Figure 4.6(d). The ILU preconditioner is not easily parallelized and will, for a fixed group size, consume more memory than the group preconditioners considered in Section 4.3.1. On the other hand, the group preconditioners do not include interactions between neighboring groups.

4.5 Numerical Results

This section investigates the convergence of iterative methods when applied to solve the matrix equation (4.2). The matrix $\bar{\mathbf{Z}}$ is obtained by applying the higher-order hierarchical Legendre basis functions in the MoM. First, the performance of two iterative methods with four different preconditioners is investigated in Section 4.5.1 for both the EFIE and CFIE. Based on this, one combination is examined closer in Section 4.5.2.

4.5.1 Comparison of Preconditioners and Iterative Methods

The iterative methods considered here are described in Appendix D. Several methods have been tested, including, but not limited to, CGS, BICGSTAB, BICG, TFQMR, and GMRES. However, the dense and relatively ill-conditioned MoM matrix systems require a very stable iterative method. It was found that BICGSTAB and GMRES always perform better than any of the other methods. Specifically, these two methods are faster as well as more robust for the present application and results for other methods will not be presented. The GMRES algorithm must be restarted to avoid buildup of rounding errors and to avoid excessive memory requirements. The restart was performed every 30 iterations for all the cases studied here. The four preconditioners outlined in Section 4.3 and 4.4 are used for both BICGSTAB and GMRES.

Convergence results for two simple objects are shown below. Specifically, the CFIE is applied to a cube and the EFIE is applied to an open cube with one face removed to ensure that the convergence is not plagued by internal resonances. These

two geometries are chosen since they involve edges and corners which tend to produce an ill-conditioned matrix. The results are obtained with fourth-order basis functions on $\frac{5\lambda}{6} \times \frac{5\lambda}{6}$ patches and the cube side length is 5λ. This leads to 6912 and 5712 unknowns in the CFIE and EFIE, respectively. The incident field is a plane wave with a $\hat{\mathbf{y}}$-polarized magnetic field and the direction of incidence is specified by ($\theta^i = 45^\circ, \phi^i = 0^\circ$) as shown in Figure 4.1. However, the convergence of the iterative methods proved to be largely independent of the incident field. The group preconditioners and the ILU preconditioner are based on a group size of 2λ. It should be emphasized that the results presented here are only illustrative examples and that a large number of experiments have been conducted for various objects with various polynomial orders and patch sizes. All these experiments supported the conclusions that are drawn below.

Many authors choose to measure the performance of iterative methods by comparing the number of iterations to achieve a certain relative error (defined as in (D.12)). This is not the best performance measure because different iterative algorithms imply different workloads per iteration. As an example, the BICGSTAB requires two matrix-vector products per iteration whereas the GMRES only requires one. Also, the time to construct the preconditioner, as well as the time to apply the preconditioner in each iteration, are not included if comparisons are based on the number of iterations. Instead, the CPU time is the proper parameter to compare although it depends on the computer hardware. To eliminate this dependence, it was chosen to normalize the CPU time with the time required to compute the solution using a direct solver. The efficient LU decomposition included in the LAPACK [128] package was used as a reference. The two group preconditioners and the Schwarz preconditioner require LU decompositions of small submatrices which are also done using the LAPACK library. The ILU decomposition is implemented in the most simple way which is not comparable to the highly optimized LAPACK library. Therefore, it is not a fair comparison if the actual setup time of the ILU preconditioner is compared to the setup times of the other preconditioners. Instead, the setup time of the ILU preconditioner is assumed to be the same as that of the overlapping group preconditioner. This is a best-case scenario since the ILU preconditioner includes much more terms than the overlapping group preconditioner (see Figures 4.5(b) and 4.5(d)).

First, the CFIE is applied to the cube. The relative errors (defined as in (D.12)) obtained with GMRES and BICGSTAB are displayed in Figures 4.7 and 4.8, respectively. Five curves are plotted in each figure corresponding to no preconditioner, group preconditioner, overlapping group preconditioner, Schwarz preconditioner, and ILU preconditioner. The observations are the same for both GMRES and BICGSTAB. The Schwarz preconditioner is only slightly better than no preconditioner at all. The group preconditioners and the ILU preconditioner perform almost equally well but the overlapping group preconditioner is the fastest. This latter preconditioner reaches a relative error of 10^{-5} in a relative CPU time of 0.02. This means that the iterative solution is 50 times faster than the direct LU decomposition. The lowest number of iterations is actually achieved by the ILU preconditioner but it is more time-consuming to apply than the other preconditioners which leaves the overlapping group preconditioner as the fastest option.

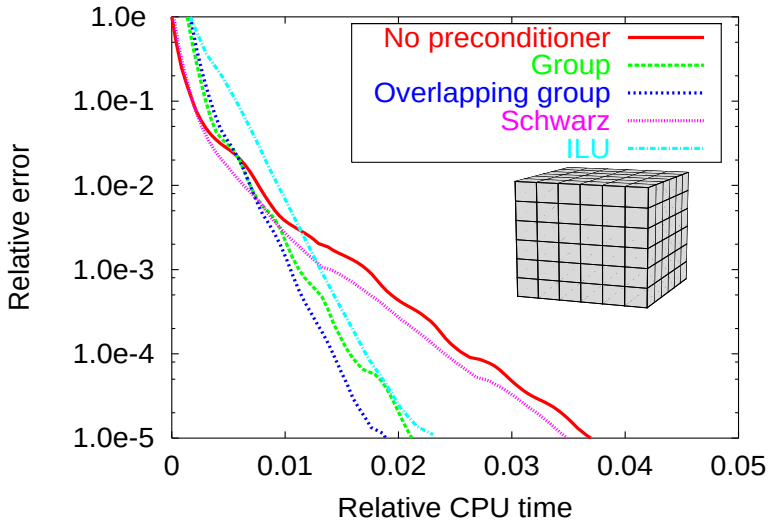

Figure 4.7: *Relative error versus relative CPU time obtained with GMRES and various preconditioners. The CFIE is applied to the cube shown in the inset.*

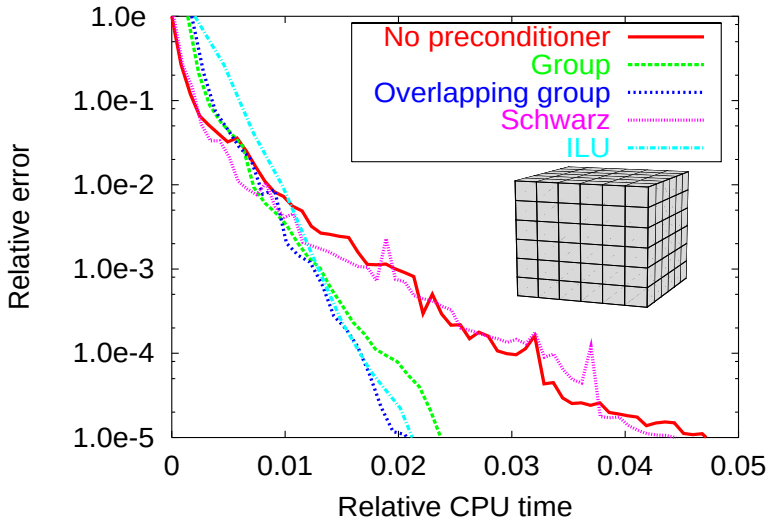

Figure 4.8: *Relative error versus relative CPU time obtained with BICGSTAB and various preconditioners. The CFIE is applied to the cube shown in the inset.*

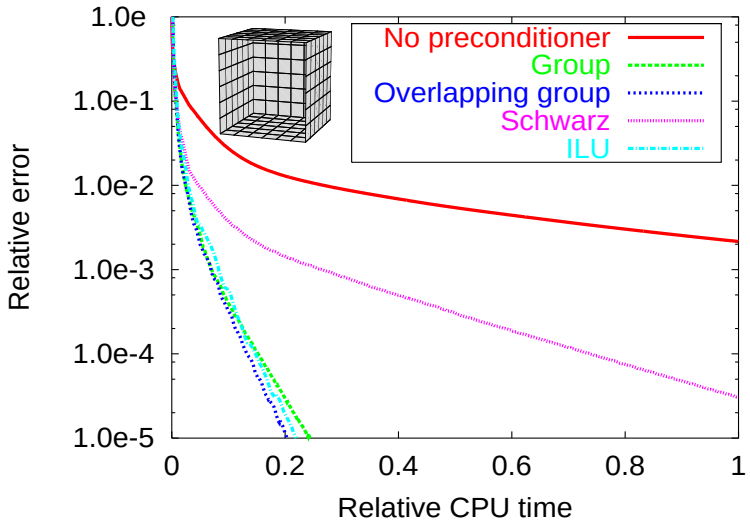

Figure 4.9: *Relative error versus relative CPU time obtained with GMRES and various preconditioners. The EFIE is applied to the open cube shown in the inset.*

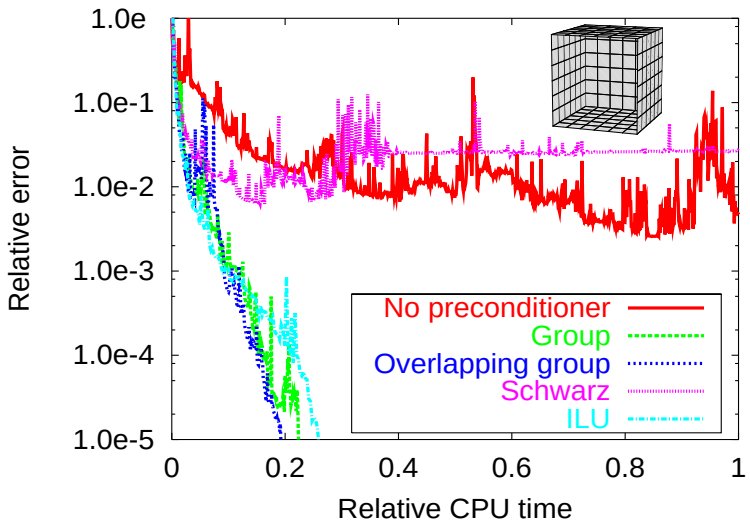

Figure 4.10: *Relative error versus relative CPU time obtained with BICGSTAB and various preconditioners. The EFIE is applied to the open cube shown in the inset.*

Next, the EFIE is applied to the open cube. The relative errors obtained with GMRES and BICGSTAB are displayed in Figures 4.9 and 4.10, respectively. The convergence is considerably slower than for the CFIE. The results obtained with GMRES using no preconditioner and the Schwarz preconditioner are only slowly converging. In contrast, the ILU preconditioner and the group preconditioners reduce the CPU time dramatically. The situation is even worse with BICGSTAB that does not converge unless one of these preconditioners is used. The overlapping group preconditioner is again the fastest.

Based on the results presented above, the GMRES seems to be the method of choice because it is more stable than the BICGSTAB for the rather ill-conditioned EFIE matrices. For the well-conditioned CFIE matrices, GMRES and BICGSTAB yield similar performance although the GMRES is usually slightly faster. The need for a good preconditioner is evident in Figures 4.7-4.10. The Schwarz preconditioner performed poorly in the cases considered here. However, other experiments verify that acceptable performance is achieved if the patch size is smaller than $\lambda/2$. This observation fits well with the the theoretical considerations in [122]-[124] that assumed that the the coarse problem is well-posed. In addition, the size of the coarse problem increases with the size of the object which implies that the setup time of the preconditioner scales as $O(N^3)$. The overlapping group preconditioner performed better than the other three preconditioners. For smaller patches ($\approx \lambda/2$) the group and overlapping group preconditioners are equally good. As the patch size increases, the overlapping domains are more important and the overlapping group preconditioner performs better than the simpler group preconditioner. In conclusion, the GMRES and the overlapping group preconditioner are the best combination which is investigated further below. It is noted that a comparison based on the number of iterations would have favored BICGSTAB and the ILU preconditioner.

4.5.2 Overlapping Group Preconditioner and GMRES

The results in this section are all obtained by applying the EFIE to the open cube. Figure 4.11 displays the convergence of GMRES using the overlapping group preconditioner when different expansion orders are applied. Specifically, the results are obtained for $M = 2, 4, 6, 8$ and pertaining patch size $\frac{5\lambda}{12}$, $\frac{5\lambda}{6}$, $\frac{5\lambda}{4}$, and $\frac{5\lambda}{3}$, respectively. This implies that all four curves requires 5712 unknowns. Both the 4th and the 6th order problem converge faster than the 2nd order problem. Thus, it seems that the expansion order can be increased without necessarily increasing the solution time. The 8th order problem converges slower than the others. This might be caused by a too small group size in the overlapping group preconditioner since each group only contains one or two patches. Experiments have shown that it is preferable to have at least 4 patches in each group. Theoretically, the GMRES method should converge monotonically. Nevertheless, some small glitches are observed on the 6th and 8th order curves. These glitches are caused by the actual GMRES implementation in which the true error is only calculated every time the method is restarted (30 iterations in this case). Between the restarts, the error is based on an estimate which apparently is not

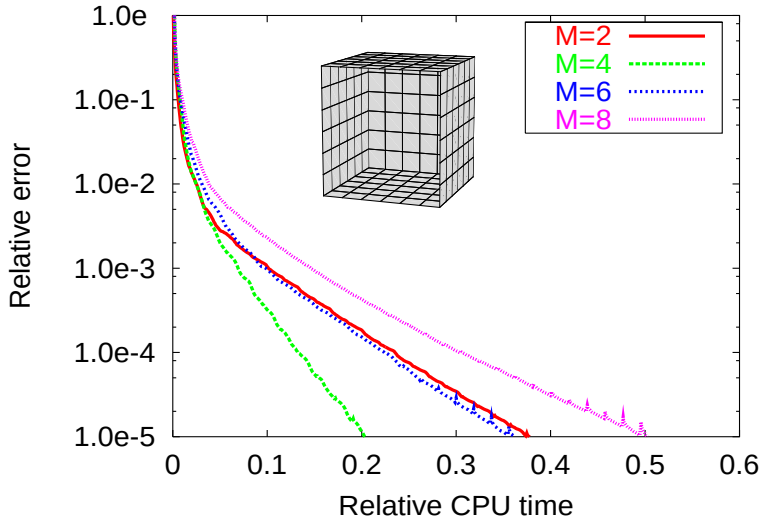

Figure 4.11: *Relative error versus relative CPU time obtained with GMRES and overlapping group preconditioner. The EFIE using different expansion orders is applied to the open cube shown in the inset.*

always accurate.

The results presented above indicate that efficient iterative solutions can be obtained even for high expansion orders. A reasonable error level for scattering computations is 10^{-4} which was achieved 3 to 10 times faster than the direct LU decomposition for the example above. However, the speedup increases with the size of the object since the CPU time scales as $O(N^2)$ and $O(N^3)$ for the iterative and direct methods, respectively. Unfortunately, the required number of iterations usually increases as the size of the object increases. For the dual-surface MFIE applied to cubes, Woodworth and Yaghjian [66] found that the number of iterations scales as $O(A^{\frac{1}{2}})$ where A is the electrical surface area of the cube. Pocock and Walker [129] found the worse $O(A)$ scaling for spheres[1]. To investigate this dependence for the higher-order functions in conjunction with the preconditioned GMRES, the EFIE is applied to open cubes of varying sizes and the number of iterations is plotted as a function of the electrical surface area in Figure 4.12(a). In this case 4th order functions and $\frac{5\lambda}{6}$ patches are used. The axes are both logarithmic and the curve $17\sqrt{A}$ is also shown. It seems that $17\sqrt{A}$ is a reasonable estimate for the number of iterations which fits well with

[1]Pocock and Walker concluded that the favorable result of Woodworth and Yaghjian was caused by special symmetry of the cube and the fact that many matrix elements are zero when the MFIE is applied to a cube. Apparently, Pocock and Walker overlooked that the dual-surface MFIE does not produce those zero entries. They also concluded that their MFIE solution was not influenced by spurious solutions simply because they chose a non-resonant frequency. The experience of this author is that the condition number of the MFIE is influenced by the presence of spurious solutions even for frequencies quite far from a resonance.

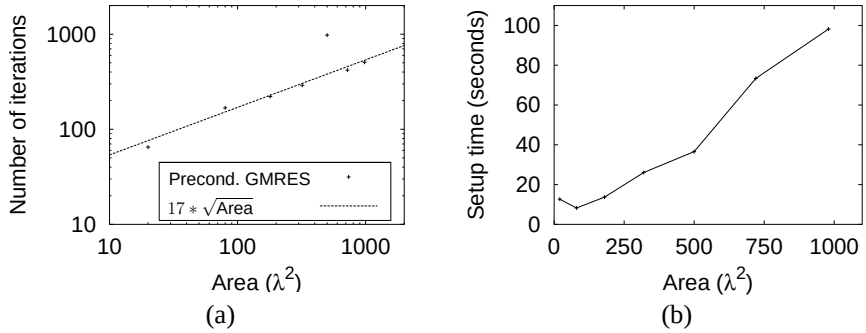

Figure 4.12: *Number of iterations versus the electrical surface area of open cube (a), and (b), setup time for overlapping group preconditioner.*

the observations of Woodworth and Yaghjian [66] and Warnick and Chew [71]. The latter work also presented an explanation for the increased number of iterations. The matrix ill-conditioning originating from long-range interactions is not removed by a near-neighbor preconditioner and the condition number increases with the electrical size of the object. The results above are obtained with a constant group size in the overlapping group preconditioner which implies that the time to construct and apply the preconditioner increases linearly with the number of groups and thus, linearly with the electrical size of the object. This is illustrated in Figure 4.12(b) that shows the setup time in seconds for the preconditioner as a functions of the electrical surface area. Both axes are linear and the setup time appears to have the expected linear dependence of the electrical surface area. This means that the fraction of the total solution time spent by preconditioning decreases as the size of the object increases.

4.6 Summary

This chapter investigated efficient iterative solution methods for higher-order MoM systems. A non-conventional MoM formulation was attempted by leaving currents and charges as independent unknowns in an augmented integral equation. However, this resulted in a high matrix condition number and it appeared feasible to keep the conventional formulation and resort to preconditioning. Four preconditioners were investigated: Two group preconditioners with or without overlap, an ILU preconditioner, and an additive Schwarz preconditioner with polynomial space decomposition. This latter preconditioner is formulated specifically for higher-order hierarchical basis functions but does not perform well for patches larger than $\lambda/2$. Instead, the overlapping group preconditioner in conjunction with the GMRES method results in the fastest convergence. The overlapping group preconditioner is a special case of an additive Schwarz preconditioner and is similar to many near-neighbor preconditioners

found in existing works except that the groups may overlap. This overlap is important when large patches are employed which is the case for higher-order basis functions. An example was shown where the 4th and 6th order solutions converged faster than the 2nd order solution which demonstrates that the expansion order can be increased without increasing the number of iterations. This conclusion differs from that of other authors, e.g. Kolundžija and Sarkar [20]. The favorable result achieved here is attributed to the low condition numbers provided by the basis functions presented in Chapter 3 in conjunction with a good preconditioner and a stable iterative method.

Chapter 5
Singular Basis Functions

Electromagnetic fields and currents can be singular in the vicinity of edges. The singular behaviour cannot be accurately represented in the polynomial spaces spanned by non-singular basis functions which leads to slow convergence. For first-order basis functions that inherently require small patches, the improper non-singular expansion of the singular current only affects a small area in vicinity of the edge. In contrast, the non-singular expansion compromises the accuracy of the currents as much as two wavelengths away from the edge when higher-order basis functions are used on large patches. Although the edge singularity appears to have a greater impact on higher-order basis functions, Kolundžija [17] showed that the higher-order basis functions still provide better accuracy for the same number of unknowns.

This chapter investigates the use of singular higher-order basis functions. A small survey of previous works on singular basis functions is presented in Section 5.1. Section 5.2 deals with the behavior of currents and charges at an infinite wedge. Section 5.3 then presents three different types of singular basis functions and numerical results are presented in Section 5.4.

5.1 Survey

The first works on singular basis functions dealt with the 2-D problem of an infinite strip and TM incidence. Wilton and Govind [28] used pulse and triangle basis functions incorporating the edge singularity. Richmond [130] considered the same problem but applied singular functions in conjunction with an entire domain Fourier expansion. The general 3-D case was considered by Andersson [26] that formulated singular basis functions incorporating both edge and corner singularities. These basis functions impose a certain behaviour on the currents directed along as well as perpendicular to the edge and were later applied to model magnetic currents in aperture problems [27]. Kaklamani and Uzunoglu [131] investigated singular entire domain basis functions for a rectangular plate. As in Andersson's works, the edge behaviour was imposed on the currents along as well as perpendicular to the edge. Kolundžija [29] formulated two kinds of singular higher-order hierarchical basis functions: One kind that imposes the edge behaviour on the current directed along the edge and another kind that imposes the edge behaviour on the current directed along as well as perpendicular to the edge. The first kind was shown to provide accurate results for the current tangential to the edge but the second kind was apparently not implemented.

The first kind was also used by Kolundžija [17] to establish an accurate benchmark solution for a square plate scatterer. Brown and Wilton [132] formulated singular interpolatory basis functions defined on curvilinear triangles but concluded that the performance was unsatisfactory for wedges. Graglia and Lombardi [30] corrected this problem and considered interpolatory basis functions of two distinct classes: Substitutive or non-substitutive. Non-substitutive basis functions are singular basis functions that reduce to the non-singular basis function in the special case where the edge is absent. Substitutive basis functions are singular basis functions that do not reduce to the non-singular basis functions. With this classification, the above-mentioned basis functions by Andersson and Kolundžija are non-substitutive.

In a recent work, Ufimtsev *et al.* [133] demonstrated that the singular behaviour of the current not only depends on geometrical parameters but also on the incident field. That is, a non-singular current may exist on an edge that qualifies for a singular current which was also discussed by Van Bladel [25]. He showed that the current directed along the edge is usually singular but zero under some special symmetry conditions. Motivated by those works, Benelli [134] considered two kinds of singular higher-order hierarchical basis functions for 2-D problems with TM incidence. One non-substitutive kind that *enforced* a singular behaviour on the current and another substitutive kind that *allowed* a singular behaviour. The numerical investigations showed that both kinds of basis functions are able to represent a singular current with almost equal accuracy. As expected, the basis functions that *allow* a singular current also provide good accuracy in absence of the singularity. However, the basis functions that *enforce* a singular behaviour are surprisingly good at representing a non-singular current. Thus, it seems that both kinds of functions can be applied without taking into account the incident field but only the geometry. The problem foreseen by Ufimtsev thus appears to be a minor problem. The study by Benelli also revealed that non-singular testing functions can be used in conjunction with singular basis functions and provide approximately the same accuracy as Galerkin testing. Thus, non-Galerkin testing schemes can perform as well as the Galerkin testing scheme which was also shown Peterson *et al.* [72]. This is worth noting since it is considerably easier to evaluate the integrals needed to fill the MoM matrix if the testing functions are non-singular.

5.2 Behaviour of Surface Currents at a Wedge

Consider the infinite PEC wedge shown in Figure 5.1. The wedge angle is denoted by β, the unit vector along the edge of the wedge by $\hat{\mathbf{z}}$, the unit vector perpendicular to the edge and along the surface of the wedge by $\hat{\boldsymbol{\rho}}$, and the unit normal vector by $\hat{\mathbf{n}}$. The distance from the edge measured along $\hat{\boldsymbol{\rho}}$ is ρ. The behaviour of the currents and charges in vicinity of a PEC wedge can be derived by using the results of Meixner [135] and restricting the observation point to be on the surface. The edge coefficient ν is determined from β as

$$\nu = \frac{\pi}{\beta}\,, \tag{5.1}$$

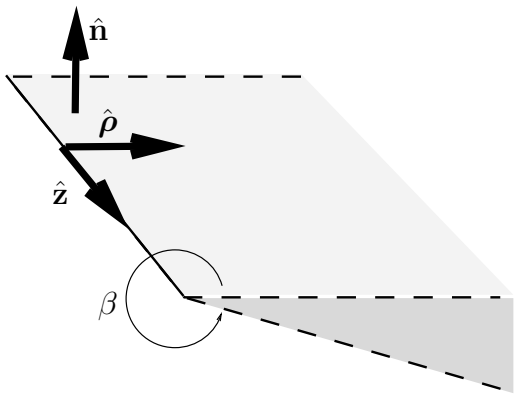

Figure 5.1: *Infinite PEC wedge with wedge angle β.*

where $\pi < \beta \leq 2\pi$ (for $0 < \beta \leq \pi$ all fields and currents are finite). The magnetic field on the surface for $k\rho \ll 1$ is then

$$H_\rho \simeq -\nu A \rho^{\nu-1} \tag{5.2a}$$

$$H_z \simeq \left(-\frac{\partial A}{\partial z} + j\omega\epsilon B\right)\rho^\nu + C\,, \tag{5.2b}$$

where A, B, and C are constant with respect to ρ but may have a z-dependence[1]. The surface current density for $k\rho \ll 1$ is obtained from $\mathbf{J}_s = \hat{\mathbf{n}} \times \mathbf{H}$ which leads to

$$J_{s\rho} \simeq \left(-\frac{\partial A}{\partial z} + j\omega\epsilon B\right)\rho^\nu + C \tag{5.3a}$$

$$J_{sz} \simeq \nu A \rho^{\nu-1}. \tag{5.3b}$$

Consequently, the current component along the edge is infinite whereas the component perpendicular to the edge is finite and generally non-zero. For the special case $\beta = 2\pi$ (half plane), C vanishes since $J_{s\rho}$ must vanish. The surface charge density for $k\rho \ll 1$ is then obtained from the continuity equation $\rho_s = \frac{j}{w}\nabla_s \cdot J_s$ as

$$\rho_s \simeq -\epsilon\nu B \rho^{\nu-1}. \tag{5.4}$$

Thus, the charge is singular at the edge. Note that the terms containing A in (5.3) cancel and do not appear in the expression for the charge. That is, J_{sz} gives rise to a

[1]The expressions found in [135] appear to be inadequate since the constant term C is not included. Similar expressions for the fi eld behavior at edges that include this constant was found by van Bladel [25]. However, this latter work considered only the z-invariant case. For several specifi c incident fi elds, the exhaustive work by Bowman, Senior, and Uslenghi [136] confi rms that H_z is indeed non-zero at the edge. The expressions in (5.2) are therefore derived from the general z-dependent case considered by Meixner but modifi ed to include the constant term.

singular charge but that contribution is exactly cancelled by another contribution originating from $J_{s\rho}$. This is interesting since some singular basis functions mentioned in Section 5.1 only incorporate the edge behaviour into J_{sz}. This leads to an infinite charge associated with J_{sz} that cannot be cancelled by a similar contribution from $J_{s\rho}$.

5.3 Three Types of Singular Basis Functions

As in Section 3.2.1, the surface current density on each patch is represented in terms of its contravariant components as

$$\mathbf{J}_s(u,v) = J_s^u(u,v)\mathbf{a}_u + J_s^v(u,v)\mathbf{a}_v. \tag{5.5}$$

Only u-directed currents are considered in the following without loss of generality. Three types of singular higher-order hierarchical Legendre basis functions are presented below. All three formulations can be used to enhance the basis given in (3.9) if edges are present. The scaling factors included in (3.9) are left out for brevity but should be included.

5.3.1 Singular Basis Functions - Formulation 1

Kolundžija [29] formulated and applied singular basis functions suitable for enhancing the power basis functions presented in [6]. These functions are of the non-substitutive kind and enforce (5.3b) but not (5.3a). Consequently, the charge cancellation associated with the current component along the edge cannot occur. For the Legendre basis functions, these singular basis functions are given by

$$J_s^u(u,v) = \frac{1}{\mathcal{J}_s(u,v)} \sum_{m=0}^{M^u} \sum_{n=0}^{N^v} b_{mn}^u \widetilde{P}_m(u) \frac{P_n(v)}{(1-v)^{1-\nu_v^+}(1+v)^{1-\nu_v^-}}, \tag{5.6}$$

where ν_v^+ and ν_v^- are the edge coefficients for the u-directed edges at $v = 1$ and $v = -1$, respectively. For $\nu_v^+ = \nu_v^- = 1$ the basis functions reduce to the non-singular Legendre basis functions (3.9).

The MoM matrix elements are evaluated by employing a Gauss-Jacobi integration scheme (see Appendix C.4) for the singular integrals along the v-direction. This means that the factor $1/((1-v)^{1-\nu_v^+}(1+v)^{1-\nu_v^-})$ is built into the integration scheme and included in the integration weights. Consequently, the integrations for the non-singular basis functions in (3.9) and the singular basis functions in (5.6) only differ by the choice of integration scheme. However, the current perpendicular to the edge does not incorporate the edge singularity which implies that the standard Gauss-Legendre integration scheme must also be used along the v-direction. This implies that the integration time is essentially doubled by incorporating the singular behavior into the basis functions. If the number of patches with edges is much lower than the number of patches without edges, the total matrix fill-time is only marginally increased.

Special care must be taken when evaluating matrix elements for basis and testing functions defined on the same patch since the annihilation procedure (see Section 3.2.3) cannot be used in conjunction with the Gauss-Jacobi integration scheme. However, the testing functions need not to be singular as demonstrated by Benelli [134]. The standard Legendre basis functions can be used as testing functions which leads to a quasi-Galerkin scheme. This allows the order of integration to be interchanged such that the inner integrand is the product of the non-singular testing function and the singular kernel. This integral is evaluated using the annihilation procedure. The outer integrand includes the singular basis function but this integral is evaluated by employing the Gauss-Jacobi integration scheme.

5.3.2 Singular Basis Functions - Formulation 2

Benelli [134] applied substitutive basis functions for a 2-D configuration with TM incidence. The polynomial basis functions were supplemented by a single singular function that allows a singular behaviour but does not enforce it. For the Legendre basis functions for surface patches, the same concept can be used to formulate substitutive singular basis functions which results in

$$J_s^u(u,v) = \frac{1}{\mathcal{J}_s(u,v)} \sum_{m=0}^{M^u} \widetilde{P}_m(u) \Bigg\{ \sum_{n=0}^{N^v} b_{mn}^u \, P_n(v) + b_m^u \frac{1}{(1-v)^{1-\nu_v^+}(1+v)^{1-\nu_v^-}} \Bigg\}. \tag{5.7}$$

The functions in the second line of (5.7) should be left out if $\nu_v^+ = \nu_v^- = 1$. As for formulation 1, the edge behaviour is only incorporated into the current component along the edge. The component perpendicular to the edge is not modified which does not allow the proper surface charge cancellation as discussed below (5.4). The matrix elements associated with these basis basis functions are computed in the same way as described for Formulation 1. Thus, the integration time is approximately doubled in comparison to non-singular functions since the integration along the v-direction must be done with both Gauss-Legendre and Gauss-Jacobi integration schemes.

5.3.3 Singular Basis Functions - Formulation 3

Kolundžija [29] also formulated singular basis functions that incorporate the edge behaviour into the current component along as well as perpendicular to the edge. The functions are non-substitutive and enforce both (5.3b) and (5.3a). Consequently, the charge cancellation discussed below (5.4) can occur. For the Legendre basis functions,

these singular basis functions are given by

$$J_s^u(u,v) = \frac{1}{\mathcal{J}_s(u,v)} \sum_{n=0}^{N^v} \left\{ b_{0n} \frac{2^{1-\nu_u^+}(1-u)}{(1-u)^{1-\nu_u^+}} + b_{1n} \frac{2^{1-\nu_u^-}(1+u)}{(1+u)^{1-\nu_u^-}} + \sum_{m=2}^{M^u} b_{mn}^u \frac{\widetilde{P}_m(u)}{(1-u)^{1-\nu_u^+}(1+u)^{1-\nu_u^-}} \right\} \frac{P_n(v)}{(1-v)^{1-\nu_v^+}(1+v)^{1-\nu_v^-}}, \tag{5.8}$$

where ν_u^+ and ν_u^- are the edge coefficients for the edges at $u = 1$ and $u = -1$, respectively. The factors $2^{1-\nu_u^+}$ and $2^{1-\nu_u^-}$ are included to ensure continuity with possibly non-singular functions on adjacent patches. It is easy to verify that (5.3a) is fulfilled by these basis functions. Consider the example $\nu_u^+ = \frac{2}{3}$ (90° wedge at $u = 1$) and $\nu_u^- = \nu_v^+ = \nu_v^- = 1$. The first term in (5.8) ($m = 0$) goes to zero as $(1-u)^{2/3}$ for $u \longrightarrow 1$ and the second term ($m = 1$) goes to a finite value determined by the coefficient b_{1n}. The terms for $m > 2$ goes to zero at $u = 1$ since $\widetilde{P}_m(1) = 0$.

The matrix elements associated with the basis functions are computed in the same way as described for Formulations 1 and 2. In the often encountered special case where the edge is a sharp edge, only one quadrature scheme is needed along each direction. This can be seen by taking $\nu_u^+ = \frac{1}{2}$ in the above example. The functions multiplying b_{1n} must then be left out to enforce a zero current perpendicular to the edge. All remaining functions then have a $(1-u)^{\nu_u^+}$ dependence, including the v-directed functions not included in (5.8), and the Gauss-Legendre scheme is not needed along the u-direction. This implies that the matrix elements are computed in approximately the same time as for the non-singular functions. Thus, in this special case Formulation 3 actually provides a faster matrix fill than Formulations 1 and 2.

5.4 Numerical Results

This section presents numerical results obtained with the three types of singular basis functions suggested above.

5.4.1 Results for Surface Currents

For simplicity, the $1\lambda \times 1\lambda$ PEC plate shown in Figure 5.2 is chosen as the test object. The plate is illuminated by a normally incident plane wave with a $\hat{\mathbf{y}}$-polarized magnetic field. Four $\frac{\lambda}{2} \times \frac{\lambda}{2}$ patches are used to mesh the plate, each of them having two external edges supporting singular currents. Fourth-order basis functions ($M = 4$) are applied although second-order basis functions are usually adequate on $\frac{\lambda}{2} \times \frac{\lambda}{2}$ patches. The high polynomial order is chosen to ensure that the currents would have converged in the absence of edges. In the following, the current obtained with non-singular basis function is compared to that obtained with three types of singular basis functions. A reference solution has been obtained by using first-order basis functions (rooftops) on $\frac{\lambda}{50} \times \frac{\lambda}{50}$ patches.

The surface current $\mathbf{J}_s$ is obtained along the curves AB and CD defined in Figure 5.2. The dominant component is J_{sx} and the normalized amplitudes $|J_{sx}|/|H^i|$ along

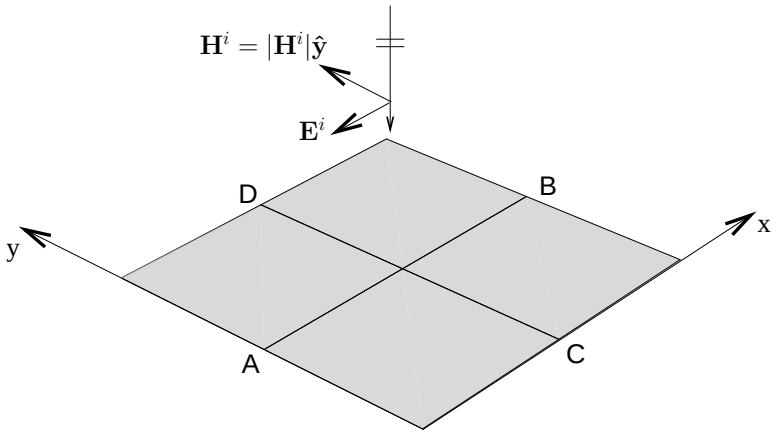

Figure 5.2: $1\lambda \times 1\lambda$ *PEC plate illuminated by a normally incident plane wave with a* $\hat{\mathbf{y}}$*-polarized magnetic field. Four square patches are used to mesh the plate. Two curves, AB and CD, are defined where the patches intersect.*

the curves AB and CD are displayed in Figure 5.3 and Figure 5.4, respectively. As observed in Figure 5.3, the non-singular basis functions yield a very poor accuracy along AB although this component is not singular. The first two types of singular basis functions provide good accuracy away from the edge but the current does not decay to zero at the right rate in vicinity of the edges. This could be expected because Formulation 1 and 2 do not incorporate the edge behaviour perpendicular to the edge. In contrast, Formulation 3 appears to be very accurate even close to the edges. The non-singular basis functions cannot accurately represent the singular current along CD displayed in Figure 5.4. However, all three types of singular basis functions provide good accuracy for this component.

Due to the symmetry of the problem, J_{sy} must be zero along AB and CD. The performance of the basis functions can therefore be rated by observing the maximum value of the normalized amplitude $|J_{sy}|/|H^i|$ along AB and CD. These values are listed in Table 5.1. The reference solution achieves a level of approximately 10^{-3}. The non-singular basis functions result in a much higher level along CD. The singular basis functions Formulation 1 and 3 result in a level comparable to the reference solution whereas Formulation 2 fails quite dramatically along CD. This problem is most likely caused by the charge cancellation mentioned below (5.4) that cannot occur for Formulation 2. The same is true for Formulation 1 but appears to be a minor problem.

Based on Figures 5.3 and 5.4 and Table 5.1, Formulation 3 is identified as the best choice. This conclusion differs from that of Kolundžija [29] that preferred Formulation 2 due to a much shorter matrix fill time. However, for the present implementation,

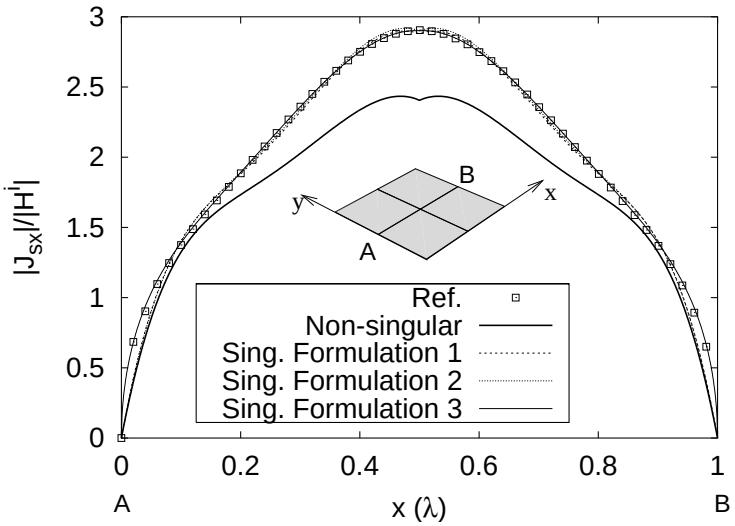

Figure 5.3: *Normalized amplitude of J_{sx} along the curve AB.*

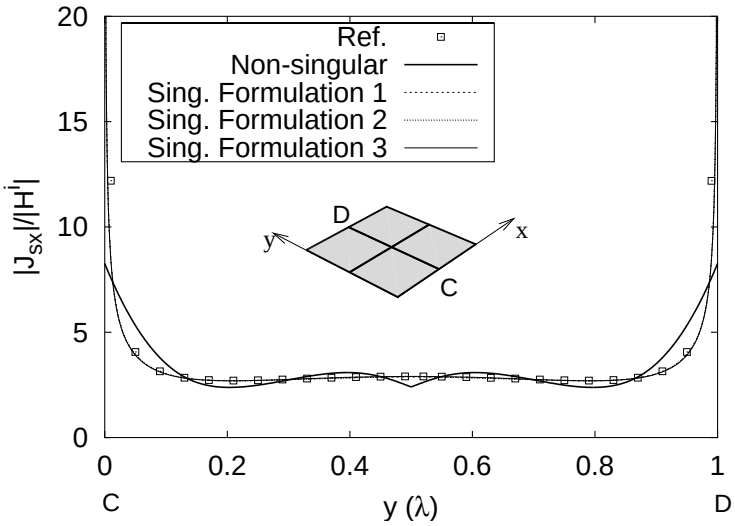

Figure 5.4: *Normalized amplitude of J_{sx} along the curve CD.*

Type of basis	AB	CD
Reference	$1.5 \cdot 10^{-3}$	$3.4 \cdot 10^{-3}$
Non-singular	$3.1 \cdot 10^{-5}$	$9.5 \cdot 10^{-2}$
Sing. Formulation 1	$9.2 \cdot 10^{-4}$	$5.2 \cdot 10^{-3}$
Sing. Formulation 2	$2.1 \cdot 10^{-4}$	1.7
Sing. Formulation 3	$6.7 \cdot 10^{-4}$	$5.1 \cdot 10^{-3}$

Table 5.1: *Maximum error of $|J_{sy}|/|H^i|$ along the curves AB and CD.*

the matrix fill time for Formulation 3 is at least as fast as for Formulation 2 and can be as fast as for the non-singular basis functions. This is a result of employing the Gauss-Jacobi integration scheme that incorporates the singular behavior.

The investigations above have been repeated for a cube which is fundamentally different because the current component perpendicular to the edge is non-zero. Nevertheless, the observations made for the plate remain valid for the cube.

5.4.2 Results for Far Fields

The far field obtained with singular basis functions Formulation 3 are now compared to that obtained with low- and higher-order basis functions. The currents displayed in Figures 5.3 and 5.4 all radiate approximately the same far field which was also noted by Kolundžija [29] for the same configuration. However, this only holds for symmetric configurations whereas experiments show that the accuracy of far fields *are* affected by the edge singularity for non-symmetric configurations. Therefore, the configuration shown in Figure 5.2 is changed such that the direction of incidence is specified by $(\theta^i = 45^\circ, \phi^i = 45^\circ)$ and the electric field is polarized along $\hat{\theta}^i$. The cross-polarized $\hat{\phi}$-component of the scattered field is observed in the cut ($\phi = 90^\circ$, $0^\circ < \theta < 90^\circ$). A very accurate reference solution has been established by using small patches and singular basis functions.

Figure 5.5(a) displays three results obtained using rooftop basis functions and $\lambda/10$, $\lambda/50$, and $\lambda/100$ square patches. The result for $\lambda/10$ patches requires $N = 180$ unknowns and is approximately 1 dB in error at $\theta = 90^\circ$. Better accuracy is obtained by increasing the number of unknowns but not even $N = 19800$ unknowns is sufficient for getting the right far field.

The result for non-singular higher-order basis functions is displayed in Figure 5.5(b) for polynomial orders $M = 4, 6, 8$. The mesh is shown in the inset of Figure 5.4 and employs four $\lambda/2 \times \lambda/2$ patches. It is observed that the accuracy improves by increasing the polynomial order but the convergence appears rather slow. Nevertheless, comparing Figures 5.5(a) and 5.5(b) reveals that 480 eight-order basis functions yield better accuracy than 4900 rooftop basis functions. For the surface currents discussed in the previous section the situation was reversed which might appear somewhat strange. However, it is well-understood by recalling the discussion on the Galerkin method given in Section 2.3.2: The Galerkin method is optimal for

(a)

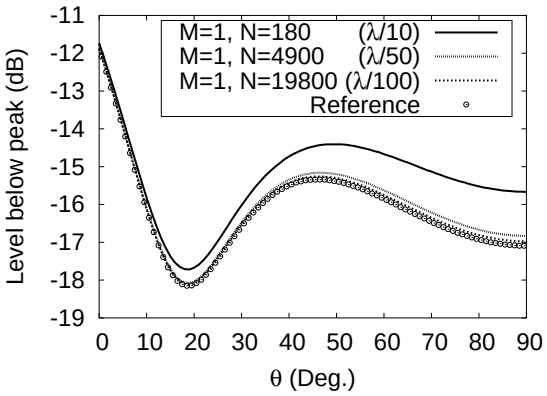

(b)

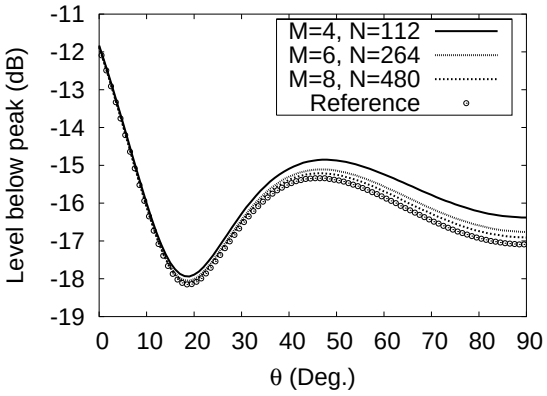

(c)

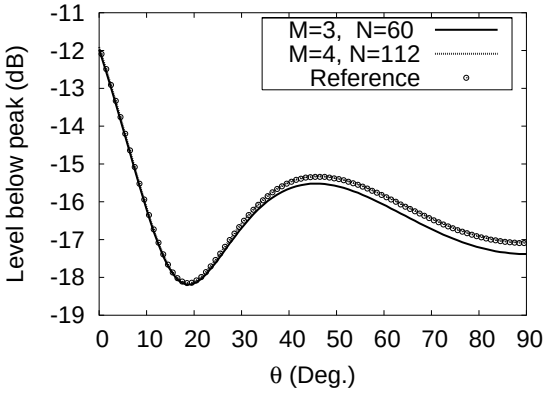

Figure 5.5: *Normalized ϕ-component of the scattered field in the cut ($\phi = 90°$, $0° < \theta < 90°$) for a $\hat{\theta}^i$-polarized plane wave incident from the direction ($\theta^i = 45°$, $\phi^i = 45°$). The results are shown for rooftops in (a), for non-singular higher-order basis functions in (b), and for singular higher-order basis functions in (c). The polynomial order is denoted M and the total number of unknowns N.*

far fields and the far field exhibits super-convergence. This appears to hold even for the quasi-Galerkin scheme used here. Neither the rooftops nor the higher-order basis functions can represent the singular physical surface current but, loosely speaking, the higher-order basis functions have better approximation power than the rooftop basis functions. Thus, higher-order basis functions can represent a non-singular equivalent surface current that radiates a more accurate far field than the rooftops. This is true even though the equivalent surface current produced by the rooftops is closer to the physical current.

The non-singular basis functions discussed above provide a relative slow convergence when edges are present. The results obtained with singular basis functions Formulation 3 are shown in Figure 5.5(c) where a much better accuracy can be observed. In fact, the result obtained with 112 unknowns cannot be distinguished from the reference solution. This leads to the conclusion that singular basis functions must be included if very accurate far fields are desired.

5.5 Summary

A survey of existing singular basis functions for objects with edges was performed. Only the works by Kolundžija [29] and Benelli [134] considered higher-order hierarchical basis functions and the three formulations suggested in those works were adapted to the Legendre basis functions derived in Chapter 3. One formulation was found to be the most accurate as well as the fastest to compute. This formulation was suggested by Kolundžija [29] and incorporates the edge behaviour into the basis functions directed along as well as perpendicular to the edge. These singular basis functions are suitable for enhancing the non-singular Legendre basis functions derived in Chapter 3 and are required to obtain accurate surface currents in the vicinity of edges. For far fields, the need for singular basis functions is questionable. Rooftop functions provide quite poor convergence but non-singular higher-order basis functions yield a fairly accurate far field and will be sufficient for many applications. However, the singular higher-order basis functions are preferable if very accurate far fields are desired.

Chapter 6
Hybrid Physical Optics - MoM

The higher-order hierarchical MoM presented in Chapter 3 is very efficient in comparison to low-order methods. Nevertheless, the computational burden becomes prohibitively large as the electrical size of the object increases. On the other hand, approximate high-frequency methods, such as the physical optics (PO), are characterized by low computational requirements and improve their accuracy as the electrical size of the object increases. However, even for electrically large objects, the PO current is not accurate close to edges, corners, or highly curved regions. On the other hand, such regions are usually small in size and may be handled with MoM. Consequently, it seems natural to formulate an efficient hybrid PO-MoM. The next section contains a survey of existing works in this area. Section 6.2 then reviews a hybrid PO-MoM formulation that appears to be the most powerful. This formulation is extended to the case of higher-order hierarchical basis functions. For this purpose, Section 6.3 presents the derivation of a projection operator based on the higher-order hierarchical Legendre basis functions. Finally, Section 6.4 presents some numerical examples to illustrate the accuracy of the method.

6.1 Survey

The idea of hybridizing MoM and asymptotic techniques was perceived more than a quarter-century ago. Early works, e.g. Thiele and Newhouse [137], hybridized MoM with the geometrical theory of diffraction and similar ray-based techniques. An overview of such hybrid methods is given by Thiele [138] and Bouche *et al.* [139]. The hybrid techniques considered below are all characterized by being current-based rather than ray-based.

For arbitrary 3-D objects, Medgyesi-Mitschang and Putnam [140] formulated a hybrid PO-MoM where the object under considerations was divided into a PO region and a MoM region. The PO region is the smooth part of the object whereas the MoM region contains edges, corners, wires, and surfaces with high curvature. Both PO currents and MoM currents are expanded in terms of MoM basis functions which allows to enforce current continuity between the two regions. Jakobus and Landstorfer [31, 32] used the same fundamental ideas but included infinitely many interactions between the MoM and PO regions. Thus, the PO current was not only determined from the incident field but also from the field radiated by the MoM region. A further extension was suggested by Hodges and Rahmat-Sahmii [141] by combining the

hybrid PO-MoM with an iterative scheme obtained by employing a Neumann series solution of the MFIE in the PO region. This iterative technique is essentially the same as the one applied earlier by Kaye *et al.* [142] and Murthy *et al.* [143]. Taboada and Obelleiro [144] recently suggested an approach similar to that of Hodges and Rahmat-Samii. Unfortunately, by allowing interactions within the PO region the memory requirement grows and becomes essentially the same as that of a full MoM solution. Thus, the hybrid PO-MoM by Jakobus and Landstorfer [31, 32] requires much less memory and can be seen as a special case of [141] and [144] if iterative improvement is not used in the PO region.

Recently, other interesting works based on similar ideas have been published. Moneum *et al.* [145] analyzed rotationally symmetric radomes by treating the radome tip with MoM and the rest with PO. Shifman and Leviatan [146] considered a 2-D problem with a rectangular groove in an infinite plane by using the PO currents to cope with the infinite region and a wavelet expansion of the fringe current in a finite region in vicinity of the groove. Han *et al.* [147] considered a hybrid method where FEM/MoM was applied to a feed system in a reflector antenna and PO/PTD to the reflector itself. They included mutual interactions between the FEM/MoM and PO/PTD regions but did not consider problems with connected FEM/MoM and PO/PTD regions. Pochini *et al.* [148] formulated a hybrid PO-MoM technique based on a uniform asymptotic representation of the PO fields and Floquet mode expansion to calculate scattering from large but finite frequency-selective surfaces. Kwon *et al.* [149] used the so-called asymptotic phasefront extraction to reduce the number of basis functions in their MoM solution. This was accomplished by forcing the basis functions to have the same phase dependence as the PO current. However, it is inconvenient that the basis functions depend on the direction of incidence and the method did not reduce the number of unknowns in shadow regions.

Based on the considerations above, it seems that the hybrid formulation of Jakobus and Landstorfer [31, 32] is the most widely accepted and generally applicable. The same formulation was applied in a series of works by Obelleiro *et al.* [150, 151] and extended to dielectric objects by Jakobus [152]. Jakobus *et al.* [153] also suggested a neural network approach to determine the MoM and PO region. In all the works using this method [31, 32, 141, 144], [150]-[153], the RWG basis functions are applied on flat triangular patches. These basis functions are used for both the MoM and PO currents and usually require approximately 120 unknowns per square wavelength to achieve good accuracy. To reduce the number of basis functions in the PO region, Taboada *et al.* [154] proposed to represent the PO currents in terms of basis functions with linear phase. This approach is similar to the asymptotic phasefront extraction described above where the phase variation of the incident field is built into the basis functions. However, in this context the incident field also comprises the field radiated by the MoM region. This limits the application of this approach to the case where the MoM region is confined to a few spatially distinct locations. As demonstrated in Chapter 3, the use of higher-order basis functions allows the number of unknowns to be reduced considerably. This reduction can be obtained in both the MoM and PO regions. In addition, higher-order hierarchical functions are ideally suited for a hybrid

PO-MoM technique since they allow small geometrical features in the MoM region as well as large smooth surfaces in the PO region to be treated efficiently. Thus, the remainder of this chapter is devoted to improving the hybrid PO-MoM first proposed in [31] by applying higher-order hierarchical basis functions and curvilinear geometry modeling.

6.2 Hybrid PO-MoM

The hybrid approach applied here is essentially that of Jakobus and Landstorfer [31] except for the choice of basis functions. The object is divided into a PO region and a MoM region. The PO region, S^{PO}, consists of the smooth part of the object and the MoM region, S^{MoM}, is the rest. Thus, S^{MoM} includes edges, corners, and surfaces with high curvature. The incident electric and magnetic fields are $\mathbf{E}^{inc}$ and $\mathbf{H}^{inc}$, respectively. The operators $\mathbf{L}^E[\mathbf{r},\mathbf{J}]$ and $\mathbf{L}^H[\mathbf{r},\mathbf{J}]$ yield the electric and magnetic fields radiated by the current $\mathbf{J}$ and observed at $\mathbf{r}$, respectively. The surface current densities in S^{MoM} and S^{PO} are denoted by $\mathbf{J}^{MoM}$ and $\mathbf{J}^{PO}$, respectively. The EFIE applied in S^{MoM} then yields

$$\mathbf{L}^E_{tan}\left[\mathbf{r},\mathbf{J}^{MoM}\right]+\mathbf{L}^E_{tan}\left[\mathbf{r},\mathbf{J}^{PO}\right]=-\mathbf{E}^{inc}_{tan}(\mathbf{r}),\quad \mathbf{r}\in\mathbf{S^{MoM}}. \tag{6.1}$$

The part of the PO current induced by the incident field is

$$\mathbf{J}^{PO,inc}(\mathbf{r})=\begin{cases} 2\hat{\mathbf{n}}\times\mathbf{H}^{inc}(\mathbf{r}), & \mathbf{r}\in \text{ lit region}\\ 0, & \text{otherwise}\end{cases}, \tag{6.2}$$

where the superscript inc is used to indicate that this current is induced by the incident field. The crucial step in [31] was to include the PO current induced by the field radiated from S^{MoM}. This leads to the total PO current $\mathbf{J}^{PO}=\mathbf{J}^{PO,inc}+\mathbf{J}^{PO,MoM}$ where

$$\mathbf{J}^{PO,MoM}(\mathbf{r})=\begin{cases} 2\hat{\mathbf{n}}\times\mathbf{L}^H\left[\mathbf{r},\mathbf{J}^{MoM}\right], & \mathbf{J}^{MoM}\text{ visible from }\mathbf{r}\\ 0, & \text{otherwise}\end{cases}. \tag{6.3}$$

The total PO current is then written as

$$\mathbf{J}^{PO}(\mathbf{r})=\delta^{inc}2\hat{\mathbf{n}}\times\mathbf{H}^{inc}(\mathbf{r})+2\hat{\mathbf{n}}\times\mathbf{L}^H\left[\mathbf{r},\delta^{MoM}\mathbf{J}^{MoM}\right] \tag{6.4}$$

where δ^{inc} is a visibility function accounting for shadowing effects of the incident field and δ^{MoM} is a visibility function accounting for shadowing effects of the MoM current. This expression is now inserted in (6.1) leading to

$$\begin{aligned}\mathbf{L}^E_{tan}\left[\mathbf{r},\mathbf{J}^{MoM}\right]+\mathbf{L}^E_{tan}\left[\mathbf{r},2\hat{\mathbf{n}}\times\mathbf{L}^H\left[\mathbf{r}',\delta^{MoM}\mathbf{J}^{MoM}\right]\right],\quad \mathbf{r}\in S^{MoM},\\ =-\mathbf{E}^{inc}_{tan}(\mathbf{r})-\mathbf{L}^E_{tan}\left[\mathbf{r},\delta^{inc}\mathbf{J}^{PO,inc}\right]\end{aligned} \tag{6.5}$$

where $\mathbf{r}'\in S^{PO}$. This equation has $\mathbf{J}^{MoM}$ as the only unknown quantity. When $\mathbf{J}^{MoM}$ is found, $\mathbf{J}^{PO}$ can be found from (6.4).

The continuous equation above is now discretized with MoM using the higher-order hierarchical Legendre basis functions defined in (3.9) and curvilinear quadrilateral patches in both S^{MoM} and S^{PO}. The scaling factors in (3.9) are left out for brevity but can easily be included. Consequently, the surface current density on each patch is represented as $\mathbf{J}_s = J_s^u \mathbf{a}_u + J_s^v \mathbf{a}_v$ where

$$J_s^u(u,v) = \sum_{m=0}^{M^u} \sum_{n=0}^{N^v} b_{mn}^u g_{mn}(u,v) \tag{6.6a}$$

$$J_s^v(u,v) = \sum_{m=0}^{M^v} \sum_{n=0}^{N^u} b_{mn}^v g_{mn}(v,u)\,, \tag{6.6b}$$

and the function g_{mn} is defined as

$$g_{mn}(u,v) = \frac{\widetilde{P}_m(u)\, P_n(v)}{\mathcal{J}_s(u,v)} \tag{6.7}$$

This expansion is used for both $\mathbf{J}^{MoM}$ and $\mathbf{J}^{PO}$ which ensures the continuity of the normal component of the current flowing between S^{MoM} and S^{PO}. The edge functions defined across the boundary between the two regions belong to both regions. By convention, the coefficients for those functions are included in the MoM unknowns. The number of MoM basis functions is denoted by N^{MoM} and the number of PO basis functions by N^{PO}. To obtain a matrix system with N^{MoM} unknowns, (6.5) is tested with N^{MoM} testing functions in a Galerkin scheme. There are no testing functions in S^{PO}. Instead, the PO current must be projected onto the PObasis functions which is elaborated in Section 6.3.

By inserting the basis and testing functions in (6.5), the discrete version of that equation becomes

$$\left(\bar{\mathbf{Z}}^{MoM} + \bar{\mathbf{Z}}^{MoM,PO}\bar{\mathbf{P}}^{PO,MoM}\right)\mathbf{I}^{MoM} = \mathbf{V} - \bar{\mathbf{Z}}^{MoM,PO}\mathbf{I}^{PO,inc} \tag{6.8}$$

in which $\bar{\mathbf{Z}}^{MoM}$ and $\mathbf{V}$ are the standard MoM matrix and excitation vector, respectively, and $\mathbf{I}^{MoM}$ is a vector containing the unknown coefficients for the MoM current. $\mathbf{I}^{PO,inc}$ is a vector obtained by projecting $\mathbf{J}^{PO,inc}$ onto the PO basis functions. The $N^{MoM} \times N^{PO}$matrix $\bar{\mathbf{Z}}^{MoM,PO}$ results from testing the electric field radiated by the PO basis function with the MoM testing functions. The $N^{PO} \times N^{MoM}$ matrix $\bar{\mathbf{P}}^{PO,MoM}$ results from projecting $\mathbf{J}^{PO,MoM}$ onto the PO basis functions. Note that this matrix is dimensionless, it maps $\mathbf{J}^{MoM}$ onto $\mathbf{J}^{PO}$. Equation (6.8) is then solved for $\mathbf{I}^{MoM}$ and the PO current is obtained through the discrete version of (6.4),

$$\mathbf{I}^{PO} = \mathbf{I}^{PO,inc} + \bar{\mathbf{P}}^{PO,MoM}\mathbf{I}^{MoM}\,. \tag{6.9}$$

The matrix-matrix product in (6.8) accounts for infinitely many interactions between S^{MoM} and S^{PO}. This product is computationally expensive and should never be evaluated explicitly which can be avoided by applying an iterative procedure to

solve (6.8). Numerical experiments have shown that the combination of the overlapping group preconditioner and the GMRES performs well (see Chapter 4). The preconditioner is then obtained from $\bar{\mathbf{Z}}^{MoM}$ alone since $\bar{\mathbf{Z}}^{MoM,PO}\bar{\mathbf{P}}^{PO,MoM}$ is not available. In fact, even if $\bar{\mathbf{Z}}^{MoM,PO}\bar{\mathbf{P}}^{PO,MoM}$ was available and included in the preconditioner, the preconditioner based on $\bar{\mathbf{Z}}^{MoM}$ alone performs better. As an alternative to the iterative approach described above, it was suggested Hodges and Rahmat-Samii [141] to obtain $\mathbf{I}^{MoM}$ through the iterative procedure

$$\mathbf{I}_{(0)}^{MoM} = \left(\bar{\mathbf{Z}}^{MoM}\right)^{-1}\left(\mathbf{V} - \bar{\mathbf{Z}}^{MoM,PO}\mathbf{I}^{PO,inc}\right) \tag{6.10a}$$

$$\mathbf{I}_{(k+1)}^{MoM} = -(\bar{\mathbf{Z}}^{MoM})^{-1}\bar{\mathbf{Z}}^{MoM,PO}\bar{\mathbf{P}}^{PO,MoM}\mathbf{I}_{(k)}^{MoM}, \quad k = 0, 1, 2, \ldots \tag{6.10b}$$

Physically, the initial solution $\mathbf{I}_{(0)}^{MoM}$ is obtained by neglecting interactions between S^{MoM} and S^{PO}. The solution is then improved iteratively by letting the MoM currents radiate into S^{PO} and back. This iterative process converges rapidly but requires the inverse of $\bar{\mathbf{Z}}^{MoM}$ which is time-consuming to compute unless $\bar{\mathbf{Z}}^{MoM}$ is very small. More investigations are needed in this area to determine the best iterative approach for a given size of $\bar{\mathbf{Z}}^{MoM}$.

If interactions between the PO and MoM regions are negligible $\bar{\mathbf{P}}^{PO,MoM}$ is set to zero and (6.8) reduces to the EFIE with an excitation vector including the field radiated by the PO currents. $\bar{\mathbf{Z}}^{MoM,PO}$ is then only needed once and is not stored.

6.3 Projection of PO Currents onto Higher-Order Basis Functions

The hybrid PO-MoM described in the previous section requires the PO current to be projected onto the PO basis functions. This is straight-forward if RWG functions are employed since each PO basis function is assigned a coefficient determined directly from the normal component of the current flowing between two adjacent patches. This simple projection procedure is not adequate for higher-order basis functions where many functions are defined on the same patch. In fact, projecting the PO current onto a general set of non-orthogonal higher-order basis functions requires the solution of a linear system of equations. Nevertheless, there is a simple relation between the higher-order Legendre basis functions and a set of orthogonal functions. This allows a simple projection procedure to be derived as below.

First, the PO current is written in terms of the covariant unitary vectors through the contravariant projection

$$\mathbf{J}_{PO} = J_{PO}^{u}\mathbf{a}_u + J_{PO}^{v}\mathbf{a}_v = (\mathbf{J}_{PO}\cdot\mathbf{a}^u)\,\mathbf{a}_u + (\mathbf{J}_{PO}\cdot\mathbf{a}^v)\,\mathbf{a}_v\,, \tag{6.11}$$

Only J_{PO}^{u} is considered below without loss of generality. The functions in (6.6) are not orthogonal. Therefore, it is more convenient to consider the expansion

$$J_{PO}^{u} = \sum_{m=0}^{M^u}\sum_{n=0}^{N^v} a_{mn}^{u} f_{mn}(u,v), \tag{6.12}$$

in which the functions f_{mn} are chosen as

$$f_{mn}(u,v) = \frac{P_m(u)P_n(v)}{\mathcal{J}(u,v)}\,. \tag{6.13}$$

These functions are mutually orthogonal if weighted with $\mathcal{J}(u,v)$, i.e.,

$$\int_S \mathcal{J}(u,v) f_{mn}(u,v) f_{ij}(u,v)\,dS = 0\,, \quad m \neq i \text{ or } n \neq j\,, \tag{6.14}$$

where the integration domain S is the specific patch under consideration and $dS = \mathcal{J}(u,v)du\,dv$. According to Appendix C.2, the coefficients a_{mn} in the expansion (6.12) are found as

$$a^u_{mn} = \frac{\int_S \mathcal{J}(u,v) f_{mn}(u,v) J^{PO}_u\,dS}{\int_S \mathcal{J}(u,v) f^2_{mn}(u,v)\,dS}\,. \tag{6.15}$$

This choice of the coefficients yields a least-squares polynomial approximation of J^u_{PO}. For the present case of Legendre polynomials the denominator becomes (see Appendix C.3.2)

$$\int_S \mathcal{J}(u,v) f^2_{mn}(u,v)\,dS = \frac{4}{(2m+1)(2n+1)}. \tag{6.16}$$

The purpose is now to establish the connection between the coefficients b^u_{mn} in (6.6a) and the coefficients a^u_{mn} in (6.15). The modified Legendre polynomials appearing in (6.6a) are defined as

$$\widetilde{P}_m(u) = \begin{cases} 1-u, & m=0 \\ 1+u, & m=1 \\ P_m(u) - P_{m-2}(u), & m \geq 2 \end{cases}\,. \tag{6.17}$$

Thus, a matrix that shifts between the basis $\widetilde{P}_m(u)$ and the basis $P_m(u)$ can be directly identified. As an example, for a 7th order expansion the matrix is

$$\bar{\mathbf{A}} = \begin{bmatrix} 1 & 1 & -1 & 0 & 0 & 0 & 0 & 0 \\ -1 & 1 & 0 & -1 & 0 & 0 & 0 & 0 \\ 0 & 0 & 1 & 0 & -1 & 0 & 0 & 0 \\ 0 & 0 & 0 & 1 & 0 & -1 & 0 & 0 \\ 0 & 0 & 0 & 0 & 1 & 0 & -1 & 0 \\ 0 & 0 & 0 & 0 & 0 & 1 & 0 & -1 \\ 0 & 0 & 0 & 0 & 0 & 0 & 1 & 0 \\ 0 & 0 & 0 & 0 & 0 & 0 & 0 & 1 \end{bmatrix}\,. \tag{6.18}$$

This implies that the matrix that shifts between the basis $P_m(u)$ and the basis $\widetilde{P}_m(u)$

is

$$\bar{\mathbf{B}} = \bar{\mathbf{A}}^{-1} = \begin{bmatrix} \frac{1}{2} & -\frac{1}{2} & \frac{1}{2} & -\frac{1}{2} & \frac{1}{2} & -\frac{1}{2} & \frac{1}{2} & -\frac{1}{2} \\ \frac{1}{2} & \frac{1}{2} & \frac{1}{2} & \frac{1}{2} & \frac{1}{2} & \frac{1}{2} & \frac{1}{2} & \frac{1}{2} \\ 0 & 0 & 1 & 0 & 1 & 0 & 1 & 0 \\ 0 & 0 & 0 & 1 & 0 & 1 & 0 & 1 \\ 0 & 0 & 0 & 0 & 1 & 0 & 1 & 0 \\ 0 & 0 & 0 & 0 & 0 & 1 & 0 & 1 \\ 0 & 0 & 0 & 0 & 0 & 0 & 1 & 0 \\ 0 & 0 & 0 & 0 & 0 & 0 & 0 & 1 \end{bmatrix}. \tag{6.19}$$

These matrices have a particularly simple structure due to the simple definition of the modified polynomials in (6.17). In fact, the matrix for an M-dimensional basis is simply the upper left $M \times M$ submatrix of the matrix for any higher order. Consequently, $\bar{\mathbf{B}}$ can be obtained for a high order and reused for all other patches, regardless of the expansion order. The projection of the PO current onto the basis functions is now simple. The coefficients a^u_{mn} are obtained through (6.15) and stored in a matrix, $\bar{\mathbf{a}}^u$. The desired coefficients b^u_{mn} are then the elements of the matrix $\bar{\mathbf{b}}^u = \bar{\mathbf{B}}\bar{\mathbf{a}}^u$. The matrix multiplication appears outside the integration and is not a time-critical step. The matrices $\bar{\mathbf{b}}^u$ and $\bar{\mathbf{b}}^v$ for each patch are then used to fill the projection matrix $\bar{\mathbf{P}}^{PO,MoM}$ in (6.8).

Before proceeding, it is worth mentioning that a similar projection would have been much more time-consuming with existing higher-order basis functions, e.g. those of Kolundžija and Popović [6] and Graglia *et al.* [7]. These basis functions have no simple relation to a set of orthogonal polynomials and a linear system needs to be solved for each patch. The dimension of this system would be $(M^u + 1)(N^v + 1)$, i.e., much larger than the matrix $\bar{\mathbf{B}}$ in (6.19) which has dimension $M^u + 1$. Also, the projection is more complicated if triangular patches are used since three current components are used on each patch. Thus, the use of existing higher-order basis functions appears inefficient, if at all possible. These remarks might explain why RWG basis functions were used in the previous hybrid PO-MoM works [31, 32, 141, 144], [150]-[153].

6.4 Numerical Results

This section shows the validity and accuracy of the higher-order hierarchical hybrid PO-MoM by considering two numerical examples.

The first example illustrates that interactions between the MoM and PO regions sometimes are negligible. The object is the offset shaped reflector antenna shown in Figure 6.1 that also lists the reflector parameters. The reflector diameter is 19.6λ and the reflector surface is discretized using 225 second-order curved quadrilaterals. The MoM region is indicated in Figure 6.1 and is only one patch wide which in this case is approximately 1.8λ.

The polynomial order is $M = 7$ and the average basis function density is 28 per square wavelength. This resulted in 2265 MoM basis functions and 7791 PO

basis functions as listed in Table 6.1. This table also lists the required memory for the full MoM solution and the hybrid solution when the coupling term in (6.8) is neglected. Therefore, only $\bar{\mathbf{Z}}^{MoM}$ needs to be stored. As observed in the table, the saving in memory is approximately a factor of 20. The incident field is computed as a spherical-wave expansion of the measured field from a corrugated horn. The induced surface current density obtained with the hybrid PO-MoM is displayed in Figure 6.2. The current appears to be continuous at the PO-MoM boundary and no anomalies are visible. The directivities obtained with MoM and the hybrid PO-MoM are shown in Figure 6.3. The PO and PO-PTD results obtained with the software package GRASP8 [155] are also shown. The hybrid PO-MoM and the PO-PTD agree very well with the MoM which illustrates the excellent accuracy of both these methods. However, the hybrid PO-MoM can be applied to much more general problems where a PTD solution is inaccurate or not possible. Furthermore, the accuracy of the hybrid PO-MoM can be improved by increasing the size of the MoM region.

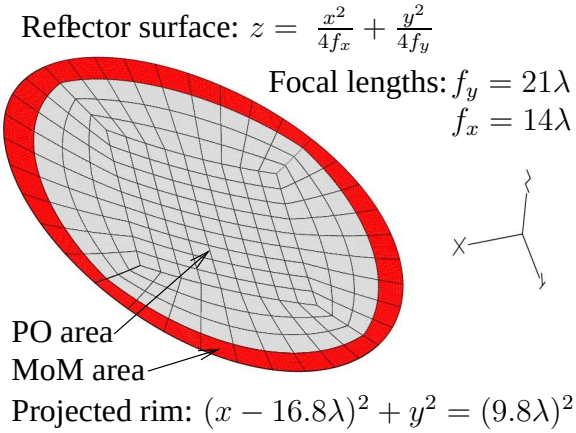

Figure 6.1: *Parameters and mesh of offset shaped reflector antenna. The MoM region S^{MoM} is one patch wide and shown in red.*

	MoM	Hybrid
N^{MoM}	10056	2265
N^{PO}	-	7791
Memory (MB)	774	40

Table 6.1: *Number of unknowns and required memory for shaped offset reflector antenna.*

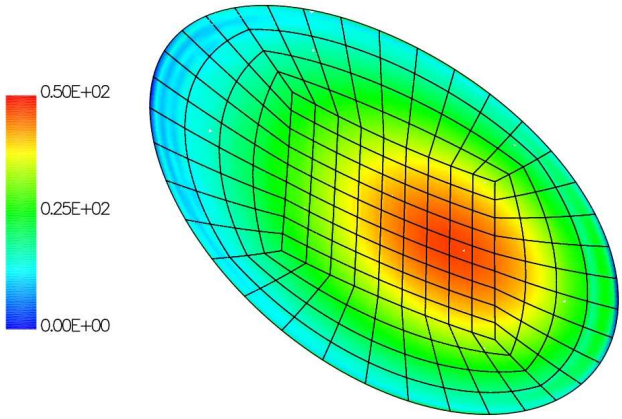

Figure 6.2: *Surface current density (A/m) on shaped reflector antenna obtained with the hybrid PO-MoM.*

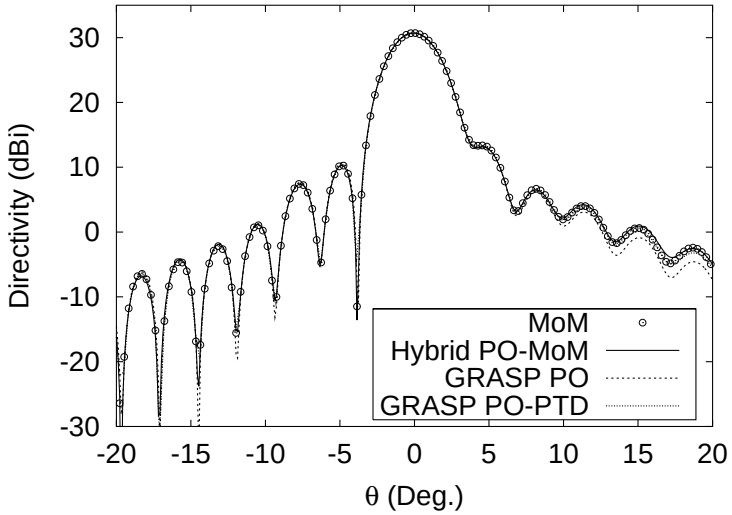

Figure 6.3: *E-plane directivity ($\phi = 0$) of offset shaped reflector antenna obtained with MoM, PO and PO-PTD from the software package GRASP8, and the hybrid PO-MoM presented here.*

The second example is a $\lambda/4$ monopole mounted at the center of a $12\lambda \times 12\lambda$ groundplane. Three wire segments are used to model the monopole which has radius $\lambda/200$. The current continuity at the wire-patch junction is enforced by using the generalized localized junction model proposed by Kolundžija [15]. The groundplane is modeled by 168 $0.92\lambda \times 0.92\lambda$ patches and four patches with one very short side connected to the monopole. The mesh is displayed in Figure 6.4 which also shows the one-patch wide MoM region and details of the monopole attachment point.

The monopole is fed by a delta-gap generator at the wire-patch junction. Therefore, the incident field is zero everywhere except at the junction. This configuration illustrates the importance of the coupling term in (6.8). Without this term, the PO current on the ground plane is zero. When this term is included, the delta gap generator sets up a current on the monopole, this current radiates a field onto the ground plane through the coupling term, and a current is induced in the PO region. The expansion orders are chosen relatively high to ensure that the results are converged; the orders are $M = 5$ on the patches and $M = 2$ on the wire segments. Table 6.2 lists the resulting number of unknowns and required memory for the MoM and the hybrid PO-MoM solution. Two hybrid solutions are considered, one with a one-patch wide MoM region as in Figure 6.4 and another with a two-patch wide MoM region. The input impedance of the monopole is also listed in Table 6.2 and the hybrid PO-MoM results are observed to be in good agreement with the MoM result. The points A and B shown in Figure 6.4 define the curve AB. The coordinate along this curve measured from A to B is denoted by t and the $\hat{\mathbf{t}}$-component of the current along AB is displayed in Figure 6.5(a). The MoM region is one patch wide in this case. The currents obtained with MoM and the hybrid PO-MoM are in good agreement in the MoM region. As mentioned above, the incident field in the PO region is zero and the PO current is caused by the coupling term in (6.8) alone. The good agreement seems to confirm the validity of this coupling term. The current obtained with MoM is modulated by a wave diffracted at the edge of the ground plane. This diffracted wave is recovered by the hybrid solution in the MoM region ($t < 0.92\lambda$) but absent in the PO region ($t > 0.92\lambda$). Figure 6.5(b) displays the currents when the MoM region is two patches wide. As expected, the diffracted wave is now recovered by the hybrid solution for $t < 1.84\lambda$. Note that all four curves in Figures 6.5(a) and 6.5(b) are not differentiable at $t = 0.92\lambda$. This problem is caused by the edge singularity described in Chapter 5

	MoM	Hybrid, 1 patch	Hybrid, 2 patches
N^{MoM}	6989	1109	3509
N^{PO}	-	5880	3480
Memory (MB)	373	109	280
Z_i (Ω)	$48.0 + j21.4$	$47.8 + j21.4$	$47.7 + j21.3$

Table 6.2: *Number of unknowns, required memory, and calculated input impedance for monopole on square groundplane.*

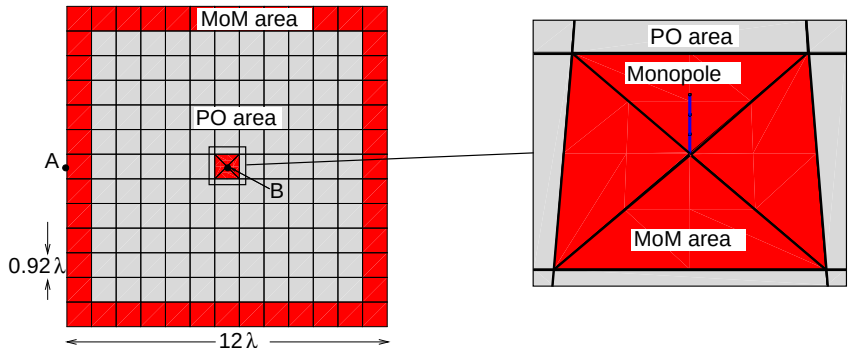

Figure 6.4: *Mesh of $\lambda/4$-monopole on a $12\lambda \times 12\lambda$ ground plane. The MoM region is one patch wide and shown in red. The points A and B define a curve for later use. On the right, details of the monopole attachment point are shown.*

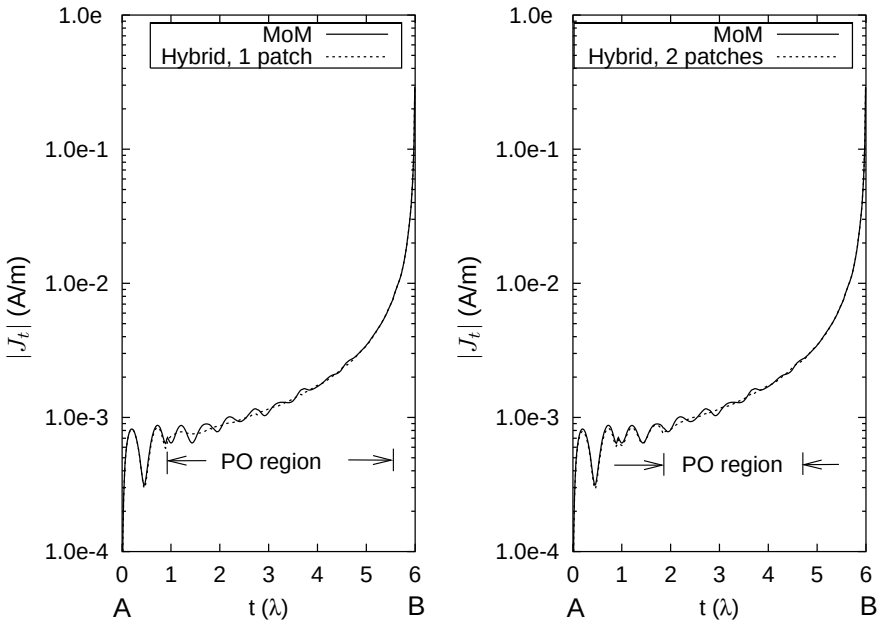

Figure 6.5: *Surface current density along the curve AB obtained with MoM and hybrid PO-MoM. The component along AB is shown. In (a), the MoM region is one patch wide. In (b), the MoM region is two patches wide.*

and could be removed by employing singular basis functions. However, the far field is not affected by this problem.

The directivity of the monopole on the square ground plane is displayed in Figure 6.6. The hybrid solutions for one- or two-patch wide MoM regions are compared to the MoM solution. The agreement is excellent for $\theta < 100^\circ$ and even the back lobes for $\theta > 90^\circ$ are quite accurately represented. The directivity of the monopole on an infinite ground plane is also shown.

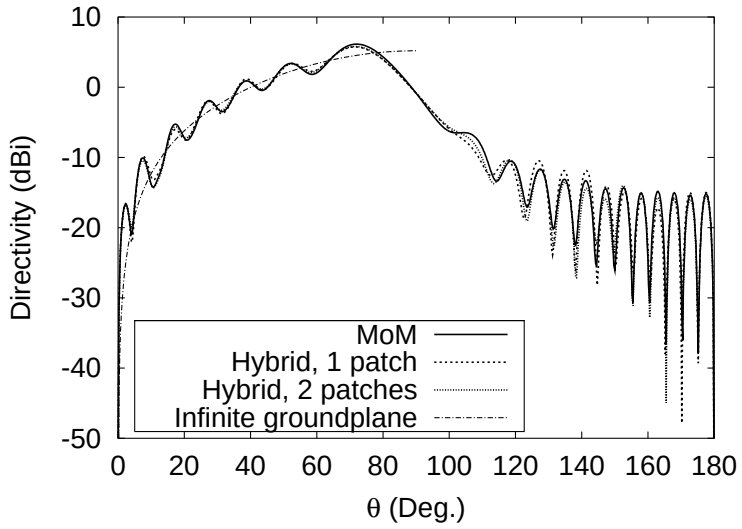

Figure 6.6: *Directivity of $\lambda/4$-monopole on a $12\lambda \times 12\lambda$ groundplane. The angle θ is measured from the monopole towards the point A. The MoM solution is compared to two hybrid solutions with MoM regions 1 or 2 patches wide, respectively. The directivity of the monopole on an infinite groundplane is also shown (only valid for $0^\circ \leq \theta \leq 90^\circ$).*

6.5 Summary

This chapter considered hybrid PO-MoM techniques. A survey was conducted and it was found that one particular hybrid formulation seems to be the most promising. Previous works using this technique employed RWG basis functions and flat triangular patches to discretize the MoM and PO currents. This technique was extended to the case of higher-order hierarchical Legendre basis functions and curvilinear geometry modeling. This extension involves the derivation of a projection operator which is particularly simple for the Legendre basis functions. The higher-order formulation has several advantages in comparison to RWG-based formulations. First, the number of unknowns can be reduced by approximately a factor of three which at the same time reduces the required memory and CPU time by one order of magnitude. Secondly, the Legendre basis functions are ideally suited for the hybrid technique. Their hierarchical property allows fine geometrical details as well as large smooth regions to be handled efficiently. Thirdly, the large patches employed by the higher-order formulation allow a MoM region which is only one patch wide and simplify the bookkeeping significantly. Two numerical examples were presented to demonstrate the accuracy of the hybrid method; a shaped reflector antenna and a monopole on a square ground plane. The hybrid results were in good agreement with the MoM results for both currents and far fields. Nevertheless, the hybrid solution requires much less memory and is considerably faster to compute. Consequently, it is applicable to problems where the computational requirements of MoM are prohibitively large.

Chapter 7
Adaptive Selection of Expansion Order

In the previous chapters, the higher-order hierarchical Legendre basis functions were applied to simple objects that were easily meshed using uniform patches. Therefore, the numerical results presented so far were obtained with a fixed expansion order on all patches and the hierarchical feature was not exploited. The purpose of this chapter is to apply the Legendre basis functions to more complicated problems where the electrical sizes of the patches differ significantly. This calls for an adaptive selection of expansion order on each patch which is demonstrated for two conceptually different configurations. Section 7.1 considers a configuration with patches of non-uniform size in a free-space environment and Section 7.2 considers a configuration with uniform patch size in a layered dielectric medium.

7.1 Object in Free-Space

The configuration considered in this section is shown in Figure 7.1. It is a shaped offset reflector antenna which is a validation standard used by the European Space Agency (ESA) for calibrating measurement facilities. The reflector has a diameter of 19.6λ and is mounted in a rigid mounting structure made of carbon-fiber reinforced plastic (CFRP). The parameters of reflector surface were given in Figure 6.1 and the directivity of the reflector without the mounting structure was obtained with the hybrid PO-MoM method in Section 6.4.

The mesh shown in Figure 7.1(b) includes a part of the mounting structure which is directly illuminated by the incident field from a corrugated horn. This field is scattered into the region $\theta > 0$ where it contributes a relative large part of the total far field. The CFRP mounting structure is modeled as a resistive sheet by enforcing the boundary condition $\hat{\mathbf{n}} \times \mathbf{E} = Z_s \hat{\mathbf{n}} \times (\hat{\mathbf{n}} \times \mathbf{H})$ (see Senior and Volakis [156]) where Z_s is the surface impedance. For CFRP, Boswell and Brewster [157] estimated $Z_s = (1 + j16)\Omega$. The mounting structure comprises sub-wavelength features that require small patches whereas the reflector surface can be modeled by large curved patches. Therefore, the mesh contains both 4- and 9-node curvilinear quadrilaterals and the patch size is between 0.1λ and 2.2λ. The expansion order is adapted to the electrical size of each patch which in this case resulted in expansion orders between $M = 1$ and $M = 10$

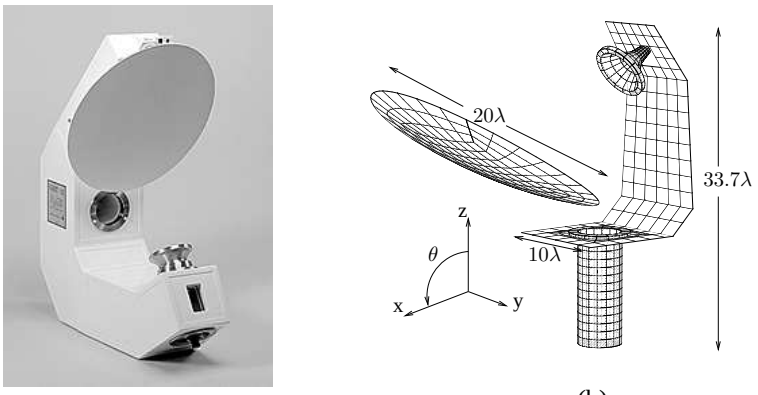

(a) (b)

Figure 7.1: *Shaped offset reflector antenna (a), and (b), mesh of the reflector, feed horn, and that part of the mounting structure contributing to the field for* $\theta > 0$*. The mesh contains both 4- and 9-node curvilinear quadrilaterals with sizes ranging from* 0.1λ *to* 2.2λ*. The total surface area is* $851\lambda^2$*.*

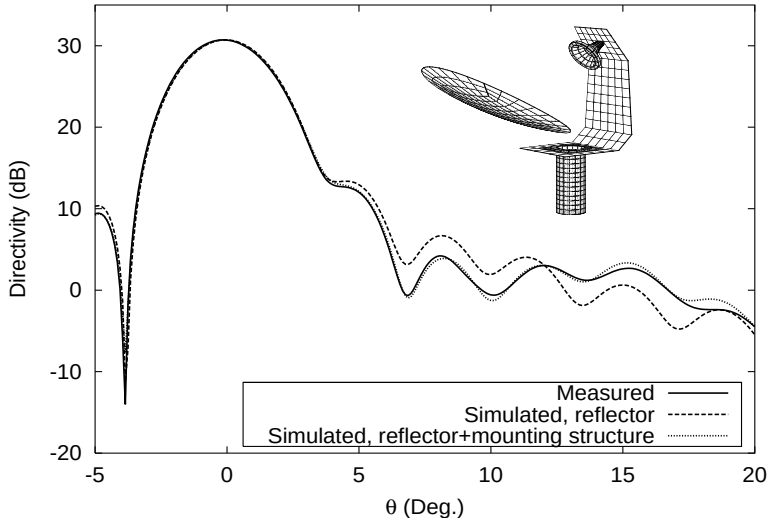

Figure 7.2: *Measured co-polar radiation pattern in the* xz*-plane for the shaped reflector antenna compared to the simulation results obtained with hierarchical Legendre basis functions. The simulations are done both with and without the mounting structure which has a significant effect on the radiation pattern for* $\theta > 0$*.*

leading to 21264 unknowns in total. This corresponds to an average basis function density of 25 per square wavelength.

The GMRES method and the overlapping group preconditioner described in Chapter 4 are applied to solve the MoM system. Despite the use of 10th order basis functions in the relatively ill-conditioned EFIE, the solution converged to a relative error of 10^{-4} in only 79 iterations. As mentioned above, the radiation pattern of the antenna is affected by the mounting structure in the region $\theta > 0$ which can be seen in Figure 7.2. The agreement with the measured result is excellent when the mounting structure is included in the simulation. The measured data were obtained at the DTU-ESA Spherical Near-Field Antenna Test Facility at the Technical University of Denmark. To put the number of iterations into perspective, an equivalent solution obtained with RWG basis functions can be used for comparison. Solving the problem at hand requires approximately 100,000 RWG functions. Consequently, the required memory and CPU time needed to perform a matrix-vector product are increased by approximately a factor of 20 in comparison to the higher-order hiearchical Legendre basis functions. Thus, the RWG solution is not competitive in terms of memory and must converge within an unlikely 4 iterations to be competitive in terms of CPU time.

7.2 Object in Layered Medium

This section considers a PEC object located in a layered medium. Specifically, the object is located below or at the interface between two dielectric half-spaces. The multilayered Green's function[1] formulated by Michalski and Zheng [158] is used to treat the dielectric half-spaces. Higher-order basis functions are well-suited for this application for two reasons. First, they result in a low number of unknowns, and secondly, they reduce the number of points where the Green's function is needed. This fact has not been discussed before in this work but can be explained by considering the number of functions defined on each patch. For low-order basis functions the number of functions on each patch is low, e.g., 4 for rooftops. For higher-order basis functions the number of functions on each patch is high, e.g., 100. Thus, one evaluation of the Green's function can be reused for 3 functions in the rooftop case and 99 functions in the higher-order case. The better reuse of Green's functions provided by the higher-order basis functions allows a significant reduction in the overall number of Green's function evaluations. This is quite important for multilayered media since the Green's function is more time-consuming to compute than the free-space Green's function. A further advantage is provided by hierarchical basis functions if the object is located at the interface between the half-spaces. The upper and lower parts of the object are then surrounded by media with different wavelengths. Nevertheless, the mesh can be kept uniform and the expansion order adapted to the electrical size of the patch in the specific medium. In contrast, methods based on non-hierarchical basis functions are forced to adjust the mesh size to the local wavelength which might differ significantly

[1] Assistant Professor Oleksiy S. Kim, Technical University of Denmark, is gratefully acknowledged for his contributions to this section. Among other things, he provided the implementation of the multilayered Green's function and produced the meshes.

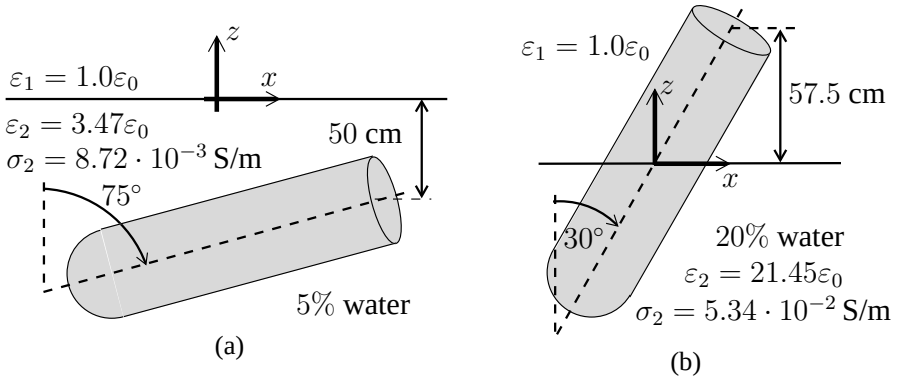

Figure 7.3: *Unexploded ordnance buried in Yuma soil with* 5% *water content in (a), and (b), partly buried in Yuma soil with* 20% *water content.*

in the two media. This kind of mesh is difficult to obtain and often involves patches of irregular shapes which are known to cause ill-conditioning. Alternatively, the part of the object located in the thinnest medium can be over-discretized. This approach leads to an excessive number of unknowns but is often preferred for simplicity, e.g., by Michalski and Zheng [158]. Numerical results for higher-order hierarchical basis functions and curvilinear surface patches in conjunction with a multilayered media cannot be found in the literature. To the knowledge of the author, this combination was only considered by Cai *et al.* [12] but their numerical results only employed rooftops and RWGs. Results for wire antennas were presented by Popović and Djurdjević [159].

The implementation is validated by considering the buried unexploded ordnance (UXO) shown in Figure 7.3(a). The UXO is 153 cm long, the diameter is 40.6 cm, and its axis is tilted 75° with respect to $\hat{\mathbf{z}}$. The upper medium is free-space and the lower medium is Yuma soil with 5% water content. The constitutive parameters for this type of soil are estimated from [160] and listed in Figure 7.3(a). The UXO is illuminated by a $\hat{\phi}^i$-polarized plane wave from the direction specified by ($\theta^i = 60^\circ, \phi^i = 0^\circ$). The frequency is set to 500 MHz. This configuration was also considered by Geng *et al.* [161] which facilitates a comparison. They used RWG basis functions and employed the FMM for the matrix-vector multiplications. The $\hat{\phi}$- and $\hat{\theta}$-polarized scattered fields are used to compute the bistatic radar cross sections (RCS) $\sigma_{\phi\phi}$ and $\sigma_{\theta\phi}$, respectively. Results for the cut ($\theta = 60^\circ$, $-180^\circ < \phi < 180^\circ$) are displayed in Figure 7.4 where good agreement between the MoM and FMM results is observed. This example and examples from [158] were used to validate the present implementation.

The higher-order hierarchical MoM result displayed in Figure 7.4 is obtained with second-order basis functions resulting in $N = 704$ unknowns. This number is much lower than that of the FMM solution in [161] which required $N = 7167$ unknowns. The excessive number of unknowns required by the FMM implementation leads to an overhead in the computational demands. This is true even when the savings provided

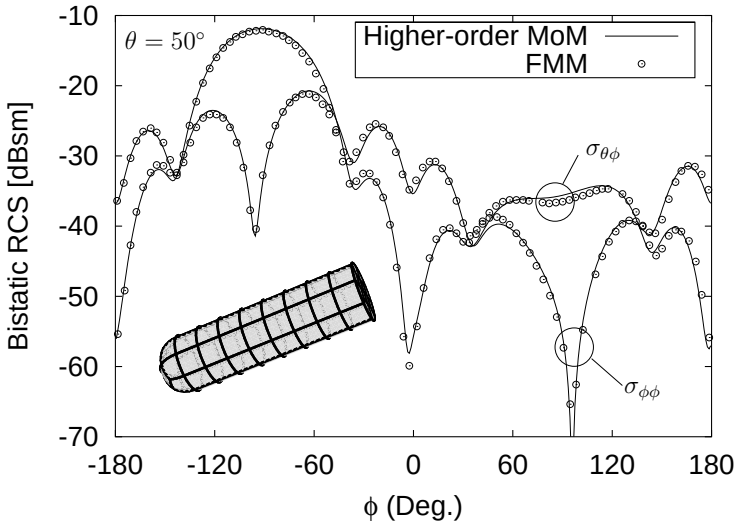

Figure 7.4: *RCS at 500 MHz in the cut* ($\theta = 60°$, $-180° < \phi < 180°$) *for* $\hat{\phi}^i$*-polarized plane wave incidence from the direction* ($\theta^i = 60°$, $\phi^i = 0°$). *The results obtained with the higher-order hierarchical MoM presented here and the FMM solution of [161] are compared.*

by FMM are taken into account. It is not possible to compare the CPU time of two implementations unless they run on the same computer. Instead, the memory usage can be compared and this quantity were reported for FMM and MLFMM in [160]. The curves shown in Figure 7.5 are reproduced from [160]. To facilitate a comparison, the memory usage is shown here as a function of the electrical surface area of the object. The memory usage of the higher-order hierarchical MoM solution presented here is also shown and compares favorably with the FMM and MLFMM. Naturally, the slope of the MoM curve is slightly higher than the slope of the two other curves to reflect the $O(N^2)$ computational complexity of MoM. The FMM and MLFMM computational complexities are $O(N^{1.5})$ and $O(N \log(N))$, respectively. By extrapolation, the MoM and MLFMM curves seem to meet at a memory usage close to 100 GByte. Thus, it is safe to say that MoM is the method of choice in comparison to the FMM and MLFMM implementations reported in [161, 160] for all computers with less than 10GByte memory. In fairness, it should be said that the results presented in [161, 160] appear somewhat over-discretized but the reason for this is not known.

The advantage of the higher-order hierarchical MoM is even greater if the object penetrates the interface between two half-spaces. Such an example is shown in Figure 7.3(b) where the UXO now has a tilt angle of $30°$ and is half-buried in Yuma soil with 20% water content. The high water content implies a high dielectric constant of $\epsilon_2 = 21.45\epsilon_0$. Hence, the wavelengths in the two half-spaces differ by a factor of 4.6 which can be accounted for in the hierarchical MoM by using a uniform mesh and adapting

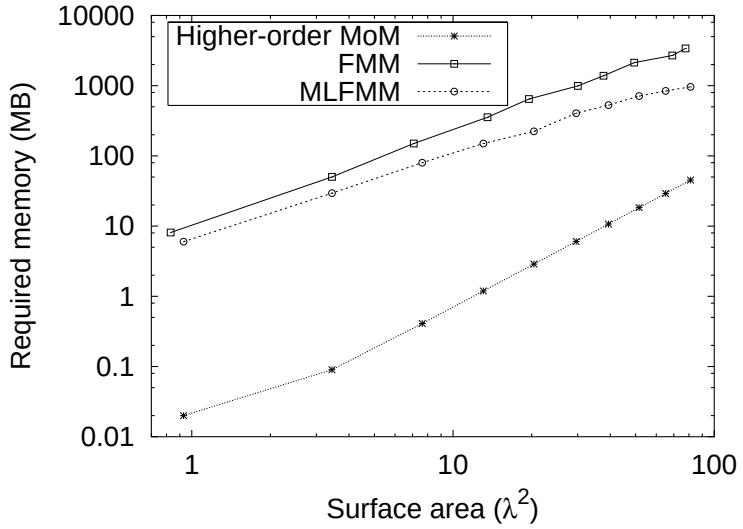

Figure 7.5: *Memory requirement versus electrical surface area of buried UXO. The FMM and MLFMM results are reproduced from [160].*

the expansion order to the electrical size of each patch measured in local wavelengths. For the present case, the maximum polynomial order above the interface is $M = 2$ and the maximum polynomial order below the interface is $M = 5$. This results in a total of $N = 2048$ unknowns. The bistatic RCS in the cut $(\theta = 40^\circ,\ -180^\circ < \phi < 180^\circ)$ is shown in Figure 7.6 and the magnitude of the surface current density is displayed in Figure 7.7. It is observed that the dominant part of the surface current is above the interface. There are no reference results available in the literature for this configuration but the memory usage of the FMM and MLFMM implementations can be found from Figure 7.5 by assuming that a uniform mesh is used and the basis function density is maintained. The electrical surface area of the upper part of the UXO is $2.7\lambda_1^2$ and the electrical surface area of the lower part is $66.0\lambda_2^2$. However, the uniform mesh must be based on the shortest wavelength which implies that a non-hierarchical method effectively sees a surface area of $124\lambda_2^2$. The MLFMM therefore needs more than 1 GByte of memory according to Figure 7.5. In contrast, the higher-order hierarchical MoM needs 34 MByte.

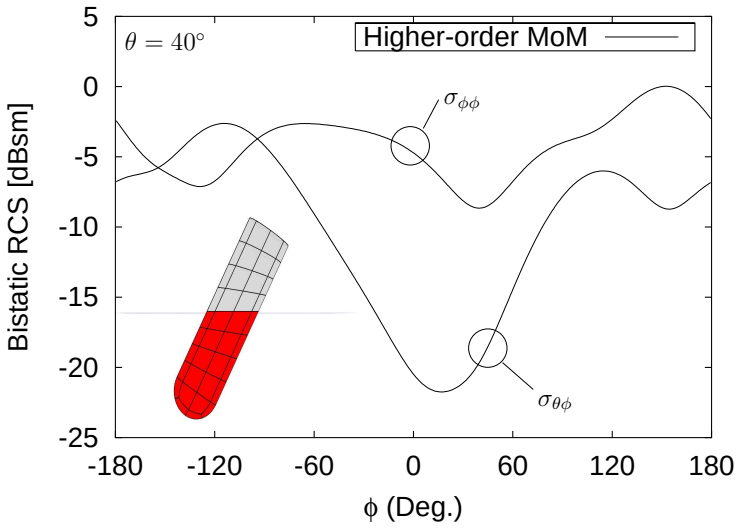

Figure 7.6: *RCS at 500 MHz in the cut* $(\theta = 40°, -180° < \phi < 180°)$ *for* $\hat{\phi}^i$*-polarized plane wave incidence from the direction* $(\theta^i = 60°, \phi^i = 0°)$.

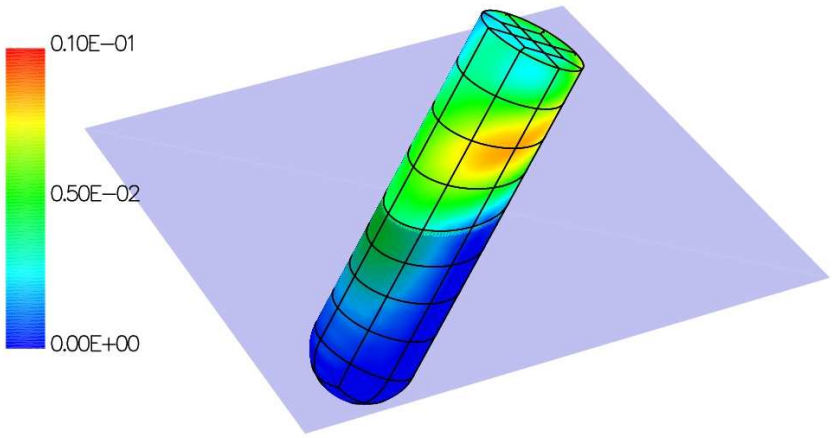

Figure 7.7: *Magnitude of surface current density* (A/m) *on half-buried inclined UXO.*

7.3 Summary

This chapter presented numerical results obtained by selecting the expansion order adaptively. A reflector antenna and its mounting structure were modeled by a combination of small and large patches employing basis functions between 1st and 10th order. Despite the use of 10th order basis functions in the relatively ill-conditioned EFIE, a matrix system with more than 20,000 unknowns was solved in 79 iterations with the iterative approach suggested in Chapter 4. A configuration involving a PEC object located at or below the interface between two dielectric half-spaces was modeled by adapting the expansion order to the size of each patch in terms of local wavelengths. This approach results in a very low number of unknowns in comparison to FMM and MLFMM implementations reported in the literature. This comparison indicated that the method presented in this work is preferable if the available computer memory is smaller than 10 GByte.

Chapter 8
Conclusions

In this study, higher-order integral equation methods for computational electromagnetics were investigated. The work has concentrated on improving the accuracy and efficiency of the MoM as applied to integral equations for arbitrary PEC surfaces.

Chapter 2 provided an overview of CEM. The advantages and disadvantages of integral- and differential-equation based methods were outlined. The most apparent difference is that the unknown in integral-equation based formulations is the source of the electromagnetic field rather than the field itself. This is advantageous for configurations involving homogeneous regions. A brief review of fundamental concepts in the area of integral equations and MoM was presented. Integral equations are derived by establishing a source-field relationship, employing the surface or volume equivalence principle, and subsequently enforcing a boundary condition. Further, the MoM was introduced as a discretization scheme for integral equations and two special cases, the method of least squares and the Galerkin method, were considered. The latter method is particularly attractive since it yields the most accurate far fields for a given set of basis functions [70]. Various types of basis functions were discussed. Particularly, a distinction was made between higher-order basis functions of interpolatory and hierarchical kinds. Hierarchical basis functions allow a flexible selection of the expansion order whereas interpolatory basis functions employ a fixed expansion order throughout the mesh. A brief explanation of the matrix condition number was given. Most importantly, the number of iterations required by iterative solution methods is proportional to the matrix condition number. Based on results available in the literature [59], it was argued that orthogonal basis functions are important for obtaining a low matrix condition number.

Chapter 3 presented the development of a new set of higher-order hierarchical Legendre basis functions. The new basis functions were constructed by using orthogonal Legendre polynomials and modifying them in a way that preserves almost perfect orthogonality. This modification allows continuity of the normal current component flowing between neighboring patches to be enforced. Apart from being near-orthogonal, the new higher-order basis functions have several other attractive features. They are easily implemented and computed for arbitrary expansion orders and owing to their hierarchical property they have all the advantages of both low-order and higher-order basis functions. Also, the basis functions applied for the surface currents implicitly provide an orthogonal expansion of the surface charge. The new basis func-

tions were developed for wires, surfaces, and volumes and numerical results were presented for second-order curved quadrilateral surface patches. These numerical results illustrated the benefit of using higher-order basis functions by comparing with exact results for a sphere. The error decays faster for higher expansion orders implying that much fewer unknowns are required to reach a certain accuracy. This comparison also revealed that the present method is more accurate than the higher-order MLFMM presented by Donepudi *et al.* [95]. The matrix condition number obtained with the new basis functions was compared to that obtained with the hierarchical basis functions of Kolundžija and Popović [6] and the interpolatory basis functions of Graglia *et al.* [7]. In contrast to the two existing formulations, the new basis functions yield only a modest increase of the condition number as the expansion order increases. Particularly, the new basis functions result in much lower condition numbers than the interpolatory basis functions. This is a remarkable result since the strongest argument for using interpolatory basis functions have been their favorable condition numbers.

Chapter 4 investigated iterative solution of higher-order MoM systems. An unsuccessful attempt of improving the convergence of the iterative solution was made by leaving currents and charges as independent unknowns in an augmented integral equation. However, this resulted in a very high matrix condition number and the standard EFIE and MFIE seem more feasible. Instead, four preconditioners were investigated: Two group preconditioners with or without overlapping domains, an ILU preconditioner, and an additive Schwarz preconditioner with polynomial space decomposition. This latter preconditioner was tailored to the higher-order hierarchical basis functions but did not perform well. Instead, the overlapping group preconditioner in conjunction with the GMRES solver provided the fastest convergence. Due to the overlapping domains employed in this preconditioner, it can be seen as an extension to many preconditioners found in existing works. The overlap is important when large patches are applied which is the case for higher-order basis functions. Numerical examples demonstrated that the order of the basis functions can be increased without increasing the number of iterations required for convergence. This important result is a consequence of the favorable condition numbers provided by the new basis functions presented in Chapter 3 in combination with the overlapping group preconditioner and the relatively robust GMRES algorithm.

Chapter 5 considered the problem of singular currents in the vicinity of edges. It was pointed out that the surface currents directed along as well as perpendicular to the edge involve a singular surface charge and that some of the singular terms exactly cancel. Three types of singular basis functions were constructed by adapting previous formulations by Kolundžija [29] and Benelli [134] to the new Legendre basis functions. Numerical experiments indicated that the edge singularity must be included in the basis functions directed along as well as perpendicular to the edge to allow for the above-mentioned charge cancellation. The preferred formulation was suggested by Kolundžija [29] but apparently never tested. For the present implementation it was found to be the most accurate as well as the fastest to evaluate. This latter conclusion differs from the conclusions reached by Kolundžija [29]. The singular higher-order basis functions yield a dramatic improvement of the surface current accuracy in the

vicinity of edges. The edge singularity is less critical for far fields but singular basis functions are still required if very high accuracy is desired. The smaller impact on the far field accuracy was explained by the characteristics of the Galerkin method discussed in Chapter 2. However, non-singular testing functions were applied in this work which facilitated a much simpler implementation. This method is not strictly Galerkin but can be seen as a quasi-Galerkin method. The possible absence of singularities discussed by Ufimtsev *et al.* [133] is believed to be a minor problem. The problem only occurs under very specific symmetry conditions and the singular basis functions represent non-singular currents with surprisingly good accuracy.

Chapter 6 dealt with hybrid PO-MoM techniques. A survey of existing works showed that the formulation by Jakobus and Landstorfer [31, 32] has been adopted by many authors. This method appears to be the most generally applicable and allows the coupling between the MoM and PO regions to be included. However, all existing works on this technique employed RWG basis functions and flat triangular patches to discretize both the MoM and PO currents. The existing low-order hybrid PO-MoM technique was extended to the case of higher-order hierarchical Legendre basis functions and curved patches. This extension involved the derivation of a projection operator that projects the PO currents onto the basis functions. This operator is particularly simple for the basis functions developed in Chapter 3 and does not require a linear system to be solved. In contrast, the corresponding projection operator for the higher-order basis functions proposed by Kolundžija and Popović [6] or Graglia *et al.* [7] would require a linear system to be solved for each patch. The number of unknowns in this linear system would be the total number of basis functions defined on each patch which can be rather large. The higher-order hierarchical hybrid PO-MoM technique has significant advantages compared to the existing techniques. Most importantly, the required memory and CPU time are reduced by approximately one order of magnitude. The curvilinear surface modeling provides better accuracy for curved surfaces and the new hierarchical Legendre basis functions allow fine geometrical details as well as large smooth regions to be handled efficiently. Furthermore, the large patches employed by the higher-order formulation simplify the bookkeeping significantly by allowing a MoM region which is just one patch wide. Numerical examples were presented to illustrate the accuracy of the hybrid method and the results were in good agreement with those obtained from a full MoM solution. However, the higher-order hybrid PO-MoM required much less memory and CPU time and is therefore applicable to problems where the computational requirements of MoM are prohibitively large.

Chapter 7 presented numerical results that fully exploited the hierarchical feature of the new Legendre basis functions. A reflector antenna and its mounting structure were discretized using patches of various sizes; large curved patches for the reflector surface and smaller patches for the sub-wavelength features of the mounting structure. Hierarchical basis functions between 1st and 10th order were applied by adapting the expansion order to the electrical size of each patch. The overlapping group preconditioner developed in Chapter 4 was used with the GMRES solver and a matrix system with more than 20,000 unknowns was solved in 79 iterations. The rapid convergence

was achieved although 10th order basis functions were applied in the relatively ill-conditioned EFIE. Further, a numerical example involving a PEC object located at the interface between two dielectric half-spaces was presented. The object was discretized with equally-sized patches and the expansion orders were adapted to the the size of each patch in terms of local wavelengths. This approach resulted in a very low number of unknowns and the required memory was compared to that of the FMM and MLFMM implementations reported by Geng *et al.* [160]. This comparison indicated that the method suggested here is more efficient than MLFMM for all problems that can be analyzed with less than 10 GByte of computer memory. In conclusion, the examples considered in Chapter 7 illustrated many important results of this work. Specifically, the new higher-order hierarchical basis functions are effective and flexible to apply, they yield favorable condition numbers even for high expansion orders, and the resulting MoM matrix system can be solved in few iterations using the overlapping group preconditioner.

The work presented in this thesis can be extended in many ways. Most importantly, the computer code should be developed further to allow homogeneous dielectric regions. This is a straightforward task by employing the new Legendre basis functions in the formulation presented by Kolundžija [18]. Also, a volume integral formulation for inhomogeneous media employing the volumetric basis functions presented in Chapter 3 is under development by Kim [42]. The initial results obtained by Kim indicate that the volumetric Legendre basis functions yield very favorable matrix condition numbers in comparison to other volumetric basis functions. Finally, the possibility of accelerating the iterative solution by means of a MLFMM procedure could be investigated. However, this approach might not be feasible unless the modifications discussed by Donepudi *et al.* [162] are applied.

Appendix A
Limiting Value of EFIE and MFIE Integrals

A.1 Integral in the EFIE

This appendix deals with the value of the integral

$$I = \nabla \int_S \rho_s(\mathbf{r}')(\mathbf{r}')G(r,r')dS' \,, \tag{A.1}$$

as the observation point $\mathbf{r}$ approaches the smooth surface S. This integral appears in some forms of the EFIE and in the CAEFIE considered in Section 4.2. It is safe to move the gradient operator inside the integral when the observation point is not on S. The quantity $\rho_s(\mathbf{r}')$ is constant with respect to the unprimed coordinates which implies

$$\nabla\left(\rho_s(\mathbf{r}')G(r,r')\right) = \rho_s(\mathbf{r}') \cdot \nabla G(r,r'). \tag{A.2}$$

The integral is separated into two integrals $I = I_{S\setminus\delta S} + I_{\delta S}$ where

$$I_{S\setminus\delta S} = \int\limits_{S\setminus\delta S} \rho_s(\mathbf{r}')\nabla G(r,r')dS' \,, \quad \mathbf{r} \notin S, \tag{A.3a}$$

$$I_{\delta S} = \int\limits_{\partial S} \rho_s(\mathbf{r}')\nabla G(r,r')dS' \,, \quad \mathbf{r} \notin S, \tag{A.3b}$$

Herein, ∂S is a small circular area with radius δ_0 and centered at a point $\mathbf{r}_0 \in S$. The smooth surface S, the circular area ∂S, and the unit normal $\hat{\mathbf{n}}$ at $\mathbf{r}_0$ are depicted in Figure A.1. The integral $I_{\partial S}$ is now considered further. The observation point is located an infinitesimal distance from the surface, i.e., $\mathbf{r} = \mathbf{r}_0 + \varepsilon\hat{\mathbf{n}}$, where $\varepsilon \ll 1$. The local cylindrical (δ, ϕ) coordinate system is introduced such that $\mathbf{r}' = \mathbf{r}_0 + \delta\cos\phi\hat{\mathbf{x}} + \delta\sin\phi\hat{\mathbf{y}}$ and $R = |\mathbf{r} - \mathbf{r}'| = \sqrt{\delta^2 + \varepsilon^2}$. When δ_0 is sufficiently small the approximation $\rho_s(\mathbf{r}') \approx \rho_s(\mathbf{r}_0)$ is reasonable. Evaluating ∇G and using $dS' = \delta d\phi\, d\delta$ yield

$$I_{\partial S} \approx -\frac{\rho_s(\mathbf{r}_0)}{4\pi} \int\limits_{\delta=0}^{\delta_0} \int\limits_{\phi=0}^{2\pi} \left(\frac{1}{R} + jk\right)(\mathbf{r} - \mathbf{r}')\,\frac{e^{-jkR}}{R^2}\delta d\phi\, d\delta \,. \tag{A.4}$$

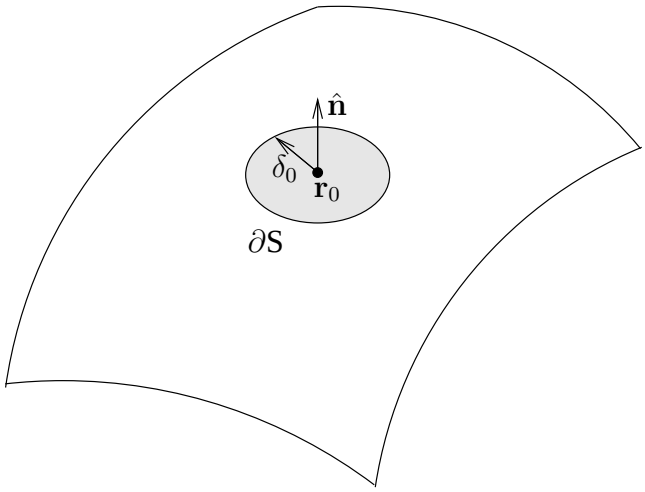

Figure A.1: *Smooth surface S with small circular area ∂S centered at the point $\mathbf{r_0}$.*

Using $kR \ll 1$ and $(\mathbf{r}-\mathbf{r}') = \varepsilon\hat{\mathbf{n}} - \delta\cos\phi\hat{\mathbf{x}} - \delta\sin\phi\hat{\mathbf{y}}$ lead to

$$I_{\partial S} \approx -\frac{\rho_s(\mathbf{r}_0)}{4\pi}\int_{\delta=0}^{\delta_0}\int_{\phi=0}^{2\pi}\frac{\varepsilon\hat{\mathbf{n}} - \delta\cos\phi\hat{\mathbf{x}} - \delta\sin\phi\hat{\mathbf{y}}}{(\delta^2+\varepsilon^2)^{\frac{3}{2}}}\delta d\phi\, d\delta, \tag{A.5}$$

The ϕ integral over the $\hat{\mathbf{x}}$ and $\hat{\mathbf{y}}$ components evaluate to zero. This leads to

$$\begin{aligned} I_{\partial S} &\approx -\hat{\mathbf{n}}\frac{\rho_s(\mathbf{r}_0)}{2}\int_{\delta=0}^{\delta_0}\frac{\varepsilon\delta}{(\delta^2+\varepsilon^2)^{\frac{3}{2}}}d\delta \\ &= \hat{\mathbf{n}}\frac{\rho_s(\mathbf{r}_0)}{2}\varepsilon\left(\frac{1}{\sqrt{\delta_0^2+\varepsilon^2}} - \frac{1}{\varepsilon}\right) \end{aligned} \tag{A.6}$$

For $\varepsilon \to 0$ ($\mathbf{r} \to \mathbf{r}_0$) this reduces to

$$I_{\partial S} \approx -\hat{\mathbf{n}}\frac{\rho_s(\mathbf{r}_0)}{2} \tag{A.7}$$

When $\delta_0 \to 0$, ∂S reduces to a single point. For an observation point on the surface, (A.1) can now be written as

$$I = -\hat{\mathbf{n}}\frac{\rho_s(\mathbf{r})}{2} + \barint_S \rho_s(\mathbf{r}')\nabla G(r,r')dS', \quad \mathbf{r}\in S\,, \tag{A.8}$$

where the bar on the integral sign indicates that the point $\mathbf{r}' = \mathbf{r}$ is excluded from the integration.

A.2 Integral in the MFIE

This appendix deals with the limiting value of the integral

$$I = \hat{\mathbf{n}} \times \left(\nabla \times \int_S \mathbf{J}_s(\mathbf{r}') G(r, r') dS' \right) , \tag{A.9}$$

as the observation point $\mathbf{r}$ approaches the smooth surface S. This integral appears in the MFIE. The derivation closely follows the derivation in Section A.1 and the same definitions apply. It is safe to move the curl operator inside the integral when the observation point is not on S. The quantity $\mathbf{J}_s(\mathbf{r}')$ is constant with respect to the unprimed coordinates which implies

$$\nabla \times (\mathbf{J}_s(\mathbf{r}') G(r, r')) = -\mathbf{J}_s(\mathbf{r}') \times \nabla G(r, r'). \tag{A.10}$$

The integral is separated into two integrals $I = I_{S \setminus \delta S} + I_{\delta S}$ where

$$I_{S \setminus \delta S} = -\hat{\mathbf{n}} \times \int\limits_{S \setminus \delta S} \mathbf{J}_s(\mathbf{r}') \times \nabla G(r, r') dS' , \quad \mathbf{r} \notin S, \tag{A.11a}$$

$$I_{\delta S} = -\hat{\mathbf{n}} \times \int\limits_{\partial S} \mathbf{J}_s(\mathbf{r}') \times \nabla G(r, r') dS' , \quad \mathbf{r} \notin S, \tag{A.11b}$$

The integral $I_{\partial S}$ is now considered further. When δ_0 is sufficiently small the approximation $\mathbf{J}_s(\mathbf{r}') \approx \mathbf{J}_s(\mathbf{r}_0)$ is reasonable. Evaluating ∇G and using $dS' = \delta d\phi \, d\delta$ yields

$$I_{\partial S} \approx \hat{\mathbf{n}} \times \left(\frac{\mathbf{J}_s(\mathbf{r}_0)}{4\pi} \times \int\limits_{\delta=0}^{\delta_0} \int\limits_{\phi=0}^{2\pi} \left(\frac{1}{R} + jk \right) (\mathbf{r} - \mathbf{r}') \, \frac{e^{-jkR}}{R^2} \delta d\phi \, d\delta \right) . \tag{A.12}$$

The integral appearing in this expression was already treated in (A.4). This directly leads to

$$I_{\partial S} \approx \hat{\mathbf{n}} \times \left(\frac{\mathbf{J}_s(\mathbf{r}_0)}{2} \times \hat{\mathbf{n}} \right) = \frac{\mathbf{J}_s(\mathbf{r}_0)}{2} \tag{A.13}$$

When $\delta_0 \to 0$, ∂S reduces to a single point. For an observation point on the surface, (A.9) can now be written as

$$I = \frac{\mathbf{J}_s(\mathbf{r})}{2} - \hat{\mathbf{n}} \times \barint_S \mathbf{J}_s(\mathbf{r}') \times \nabla G(r, r') dS', \quad \mathbf{r} \in S , \tag{A.14}$$

where the bar on the integral sign indicates that the point $\mathbf{r}' = \mathbf{r}$ is excluded from the integration.

Appendix B
Curvilinear Geometry Modeling

B.1 Quadrilateral Patches of Arbitrary Order

Higher-order integral equation methods require the surface of a given object to be subdivided into smaller pieces. These smaller pieces are referred to as patches. The patches that have been preferred in this work are generalized quadrilateral patches of arbitrary order. A standard quadrilateral is a plane polygon with four straight edges. A generalized quadrilateral is not necessarily plane and the edges are not necessarily straight. In the following, the term quadrilateral patch, or just patch, will be used for both standard quadrilaterals as well as generalized quadrilaterals. Each quadrilateral has an associated curvilinear parametric (u, v) coordinate system defined by $-1 \leq u, v \leq 1$ and the surface of the quadrilateral is approximated by interpolatory polynomials of order p. The quadrilateral surface is then in exact agreement with the actual surface at $(p+1)^2$ interpolation nodes but not necessarily in between. The expression for the pth order quadrilateral can be written as [52]

$$\mathbf{r}(u, v) = \sum_{i=0}^{p} \sum_{j=0}^{p} \mathbf{r}_{ij} \phi_i(p, u) \phi_j(p, v) \tag{B.1}$$

where $\mathbf{r}_{ij}$ are the interpolation nodes and $\phi_i(p, u)$ is the ith Lagrange polynomial of order p

$$\phi_i(p, u) = \prod_{\substack{k=0 \\ k \neq i}}^{p} \frac{u - u_k}{u_i - u_k}, \tag{B.2}$$

in which u_k is the parametric coordinate of the interpolation node. For practical reasons, the most commonly used patches are bilinear quadrilaterals defined by 4 interpolation nodes ($p = 1$), or curved biquadratic quadrilaterals defined by 9 nodes ($p = 2$). These two cases are illustrated in Figure B.1. Although it was stated as the final result in [52], the representation above is not suitable for implementation. In fact, the expression in (B.1) requires evaluation of $2(p+1)$ different Lagrange polynomials each time $\mathbf{r}$ is needed. The rest of this section is aimed at obtaining a more useful form.

The most natural choice of interpolation nodes is obtained by choosing $p + 1$

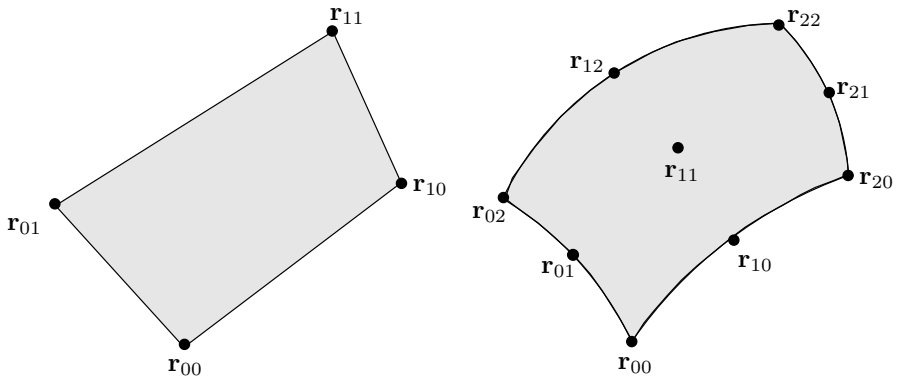

Figure B.1: *Bilinear quadrilaterals defined by 4 interpolation nodes (a), and bi-quadratic quadrilateral defined by 9 interpolation nodes (b).*

equidistant u_k's, i.e., $u_k = -1 + 2k/p$. Inserting this in (B.2) yields

$$\phi_i(p,u) = \prod_{\substack{k=0 \\ k\neq i}}^{p} \frac{\frac{p}{2}(u+1)-k}{i-k}\,. \tag{B.3}$$

An alternative representation of (B.1) that is more convenient for implementation and facilitates mixing patches of different orders in the same mesh is

$$\mathbf{r}(u,v) = \sum_{k=0}^{p}\sum_{l=0}^{p} \mathbf{r}_{u^k v^l} u^k\, v^l \tag{B.4}$$

where $\mathbf{r}_{u^k v^l}$ are constant vectors given by a linear combination of the interpolation nodes $\mathbf{r}_{ij}$ which can be identified by inserting (B.3) in (B.1). To simplify the notation, the geometrical center of the quadrilateral $\mathbf{r}_{u^0 v^0}$ is denoted by $\mathbf{r}_c$. Further, all subscripts with the exponent zero are left out. For a 4-node quadrilateral, (B.4) reduces to

$$\mathbf{r}(u,v) = \mathbf{r}_c + u\mathbf{r}_u + v\mathbf{r}_v + uv\mathbf{r}_{uv}\,. \tag{B.5}$$

Similarly, for a 9-node quadrilateral

$$\begin{aligned}\mathbf{r}(u,v) \;&= \mathbf{r}_c + u\mathbf{r}_u + v\mathbf{r}_v + uv\mathbf{r}_{uv} \\ &\quad + u^2\mathbf{r}_{u^2} + v^2\mathbf{r}_{v^2} + u^2 v\mathbf{r}_{u^2 v} + uv^2\mathbf{r}_{uv^2} + u^2v^2\mathbf{r}_{u^2v^2}\,.\end{aligned} \tag{B.6}$$

By comparing (B.5) and (B.6) the advantage of this representation is clear: Higher-order terms are simply added as the order of the quadrilateral increases. Further, evaluation of $\mathbf{r}$ requires just one polynomial to be evaluated. The geometrical information

should therefore be stored in the format defined by (B.4). As mentioned above, the vectors $\mathbf{r}_{u^k v^l}$ are linear combinations of the the interpolation nodes. Table B.1 gives the expressions for 4- and 9-node quadrilaterals.

	p=1	p=2
$\mathbf{r}_c$	$\frac{1}{4}(\mathbf{r}_{00}+\mathbf{r}_{10}+\mathbf{r}_{01}+\mathbf{r}_{11})$	$\mathbf{r}_{11}$
$\mathbf{r}_u$	$\frac{1}{4}(-\mathbf{r}_{00}+\mathbf{r}_{10}-\mathbf{r}_{01}+\mathbf{r}_{11})$	$\frac{1}{2}(\mathbf{r}_{21}-\mathbf{r}_{01})$
$\mathbf{r}_v$	$\frac{1}{4}(-\mathbf{r}_{00}-\mathbf{r}_{10}+\mathbf{r}_{01}+\mathbf{r}_{22})$	$\frac{1}{2}(\mathbf{r}_{12}-\mathbf{r}_{10})$
$\mathbf{r}_{uv}$	$\frac{1}{4}(\mathbf{r}_{00}+\mathbf{r}_{10}+\mathbf{r}_{01}+\mathbf{r}_{22})$	$\frac{1}{4}(\mathbf{r}_{00}-\mathbf{r}_{20}-\mathbf{r}_{02}+\mathbf{r}_{22})$
$\mathbf{r}_{u^2}$		$\frac{1}{2}(\mathbf{r}_{21}+\mathbf{r}_{01})-\mathbf{r}_{11}$
$\mathbf{r}_{v^2}$		$\frac{1}{2}(\mathbf{r}_{12}+\mathbf{r}_{10})-\mathbf{r}_{11}$
$\mathbf{r}_{u^2v}$		$\frac{1}{4}(-\mathbf{r}_{00}-\mathbf{r}_{20}+\mathbf{r}_{02}+\mathbf{r}_{22})$ $-\frac{1}{2}(\mathbf{r}_{12}-\mathbf{r}_{10})$
$\mathbf{r}_{uv^2}$		$\frac{1}{4}(-\mathbf{r}_{00}+\mathbf{r}_{20}-\mathbf{r}_{02}+\mathbf{r}_{22})$ $-\frac{1}{2}(\mathbf{r}_{21}-\mathbf{r}_{01})$
$\mathbf{r}_{u^2v^2}$		$\frac{1}{4}(\mathbf{r}_{00}+\mathbf{r}_{20}+\mathbf{r}_{02}+\mathbf{r}_{22})+\mathbf{r}_{11}$ $-\frac{1}{2}(\mathbf{r}_{10}+\mathbf{r}_{01}+\mathbf{r}_{21}+\mathbf{r}_{12})$

Table B.1: *Expressions for the vectors $\mathbf{r}_{u^k v^l}$ in (B.4) in terms of the vectors $\mathbf{r}_{ij}$ in (B.3) for $p = 1, 2$.*

B.2 Covariant and Contravariant Projections

The previous section described a possible way to parameterize a given surface by dividing it into generalized quadrilaterals and introducing a curvilinear (u, v) coordinate system on each quadrilateral. This section shows how a vector function, such as the electric surface current density, is represented in the curvilinear coordinate system. The general theory for a volumetric curvilinear coordinate systems were given by Stratton [163] and this section presents the simplified results for a surface.

It is assumed that a parametric representation of a surface is given by

$$\mathbf{r}(u,v) = \hat{\mathbf{x}} f_x(u,v) + \hat{\mathbf{y}} f_y(u,v) + \hat{\mathbf{z}} f_z(u,v), \quad -1 \leq u, v \leq 1\,, \tag{B.7}$$

where f_x, f_y, and f_z are continuous functions with continuous derivatives. A curve with constant v coordinate will be referred to as an u coordinate curve and vice versa. The so-called covariant unitary vectors defined by

$$\mathbf{a}_u = \frac{\partial \mathbf{r}}{\partial u} \quad , \quad \mathbf{a}_v = \frac{\partial \mathbf{r}}{\partial v}\,, \tag{B.8}$$

are tangential to the u and v coordinate curves, respectively. Using these covariant unitary vectors, a differential change in $\mathbf{r}$ can be written as

$$d\mathbf{r} = \mathbf{a}_u\, du + \mathbf{a}_v\, dv\,. \tag{B.9}$$

Note that the covariant unitary vectors in general are non-orthogonal and not of unit length. These vectors are convenient base vectors for representing a vector quantity in the curvilinear coordinate system. Alternatively, base vectors orthogonal to the u and v coordinate curves could be chosen. These vectors are the contravariant unitary vectors

$$\mathbf{a}^u = \nabla u \quad , \quad \mathbf{a}^v = \nabla v\,, \tag{B.10}$$

which are also non-orthogonal and not of unit length. From the definitions above, it is straightforward to show the relations

$$\mathbf{a}_u \cdot \mathbf{a}^u = 1 \quad , \quad \mathbf{a}_v \cdot \mathbf{a}^v = 1\,, \tag{B.11a}$$

$$\mathbf{a}_u \cdot \mathbf{a}^v = 0 \quad , \quad \mathbf{a}_v \cdot \mathbf{a}^u = 0\,. \tag{B.11b}$$

Let $\mathbf{F}$ be an arbitrary vector function defined on the curvilinear surface and assume that $\mathbf{F}$ is tangential to the surface. $\mathbf{F}$ is then written in terms of the covariant unitary vectors through the contravariant projection

$$\mathbf{F} = (\mathbf{F} \cdot \mathbf{a}^u)\, \mathbf{a}_u + (\mathbf{F} \cdot \mathbf{a}^v)\, \mathbf{a}_v\,. \tag{B.12}$$

Alternatively, $\mathbf{F}$ can be written in terms of the contravariant unitary vectors through the covariant projection

$$\mathbf{F} = (\mathbf{F} \cdot \mathbf{a}_u)\, \mathbf{a}^u + (\mathbf{F} \cdot \mathbf{a}_v)\, \mathbf{a}^v\,. \tag{B.13}$$

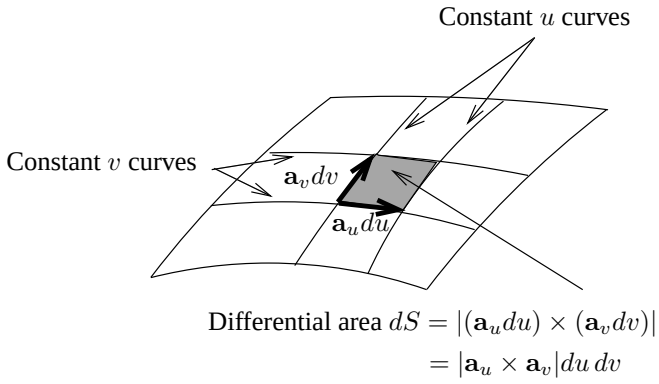

Figure B.2: *Differential area on curvilinear surface.*

The notation applied by Stratton [163] is adopted here. Consequently, F_u and F_v denote the covariant components of $\mathbf{F}$, i.e.,

$$F_u = \mathbf{F} \cdot \mathbf{a}_u \quad , \quad F_v = \mathbf{F} \cdot \mathbf{a}_v \,, \tag{B.14}$$

and F^u and F^v denote the contravariant components of $\mathbf{F}$

$$F^u = \mathbf{F} \cdot \mathbf{a}^u \quad , \quad F^v = \mathbf{F} \cdot \mathbf{a}^v \tag{B.15}$$

Note that this notation differs from the one used by Peterson *et al.* [52].

The differential area can be found as illustrated in Fig. B.2. The differential length vectors along the u- and v-coordinate curves are $\mathbf{a}_u du$ and $\mathbf{a}_v dv$, respectively. The differential area is the area of the parallelogram subtended by $\mathbf{a}_u du$ and $\mathbf{a}_v dv$, that is

$$dS = |\,(\mathbf{a}_u du) \times (\mathbf{a}_v dv)\,| = |\mathbf{a}_u \times \mathbf{a}_v|\, du\, dv = \mathcal{J}_s\, du\, dv \,, \tag{B.16}$$

where the surface Jacobian is defined by $\mathcal{J}_s = |\mathbf{a}_u \times \mathbf{a}_v|$.

The differential operators were derived by Stratton [163]. Specifically, the surface gradient, surface divergence, and curl are expressed as

$$\nabla_s \Phi = \mathbf{a}^u \frac{\partial \Phi}{\partial u} + \mathbf{a}^v \frac{\partial \Phi}{\partial v} \,, \tag{B.17a}$$

$$\nabla_s \cdot \mathbf{F} = \frac{1}{\mathcal{J}_s} \left(\frac{\partial}{\partial u}(\mathcal{J}_s F^u) + \frac{\partial}{\partial v}(\mathcal{J}_s F^v) \right) \,, \tag{B.17b}$$

$$\nabla \times \mathbf{F} = \frac{1}{\mathcal{J}_s} \left(\frac{\partial F_v}{\partial u} - \frac{\partial F_u}{\partial v} \right) \hat{\mathbf{n}} \,. \tag{B.17c}$$

Note that the divergence is expressed in terms of the contravariant components whereas the curl is expressed in terms of the covariant components. Naturally, the divergence can also be expressed in terms of the covariant components and the curl in terms of the

contravariant components but those expressions are more complicated than (B.17b) and (B.17c). In (B.17c), the unit normal vector $\hat{\mathbf{n}}$ is given by

$$\hat{\mathbf{n}} = \frac{\mathbf{a}_u \times \mathbf{a}_v}{|\mathbf{a}_u \times \mathbf{a}_v|} = \frac{\mathbf{a}_u \times \mathbf{a}_v}{\mathcal{J}_s} \,. \tag{B.18}$$

Finally, (B.11) and (B.18) can be used to derive

$$\mathbf{a}_u = \mathcal{J}_s \, \mathbf{a}^v \times \hat{\mathbf{n}} \,, \tag{B.19a}$$

$$\mathbf{a}_v = \mathcal{J}_s \, \hat{\mathbf{n}} \times \mathbf{a}^u \,, \tag{B.19b}$$

$$\mathbf{a}^u = \frac{1}{\mathcal{J}_s} \mathbf{a}_v \times \hat{\mathbf{n}} \,, \tag{B.19c}$$

$$\mathbf{a}^v = \frac{1}{\mathcal{J}_s} \hat{\mathbf{n}} \times \mathbf{a}_u \,. \tag{B.19d}$$

The latter two expressions also imply

$$|\mathbf{a}_v| = \mathcal{J}_s |\mathbf{a}^u| \,, \tag{B.20a}$$

$$|\mathbf{a}_u| = \mathcal{J}_s |\mathbf{a}^v| \,. \tag{B.20b}$$

B.3 Imposing Normal or Tangential Continuity

Assume that a surface is subdivided into curvilinear quadrilaterals as explained in Section B.1 and that some physical vector quantity $\mathbf{F}$ is represented through a covariant or a contravariant projection as in Section B.2. This section then explains how normal or tangential continuity of $\mathbf{F}$ can be imposed between neighboring quadrilaterals.

Consider the two quadrilaterals Q_a and Q_b shown in Figure B.3 and assume that tangential continuity is desired across the edge shared by Q_a and Q_b. The covariant and contravariant unitary vectors are shown at the point P on the edge. The unitary vectors are not the same in Q_a and Q_b and are drawn slightly displaced to make this clearly visible. In addition, the $\mathbf{b}$ is used to denote the unitary vectors in Q_b. The covariant unitary vectors $\mathbf{a}_v$ and $\mathbf{b}_v$ are identical since they are tangential to the common edge. Therefore, it is tempting to use a contravariant projection to represent $\mathbf{F}$ as

$$\mathbf{F}(\mathbf{r}) = \begin{cases} F_a^u \mathbf{a}_u + F_a^v \mathbf{a}_v, & \mathbf{r} \in Q_a \\ F_b^u \mathbf{b}_u + F_b^v \mathbf{b}_v, & \mathbf{r} \in Q_b \end{cases} \,, \tag{B.21}$$

and impose $F_a^v = F_b^v$. However, $\mathbf{a}_u$ and $\mathbf{b}_u$ also have tangential components along the edge. Consequently, enforcing tangential continuity actually puts a restriction on all four components, F_a^u, F_a^v, F_b^u, and F_b^v. Furthermore, the covariant unitary vectors in each quadrilateral have tangential components along three other edges. Enforcing tangential continuity is therefore next to impossible since F_a^u, F_a^v, F_b^u, and F_b^v are restricted by the continuity at all 4 edges of their respective quadrilaterals. Alternatively, $\mathbf{F}$ can be represented through the covariant projection

$$\mathbf{F}(\mathbf{r}) = \begin{cases} F_u^a \mathbf{a}^u + F_v^a \mathbf{a}^v, & \mathbf{r} \in Q_a \\ F_u^b \mathbf{b}^u + F_v^b \mathbf{b}^v, & \mathbf{r} \in Q_b \end{cases} \,. \tag{B.22}$$

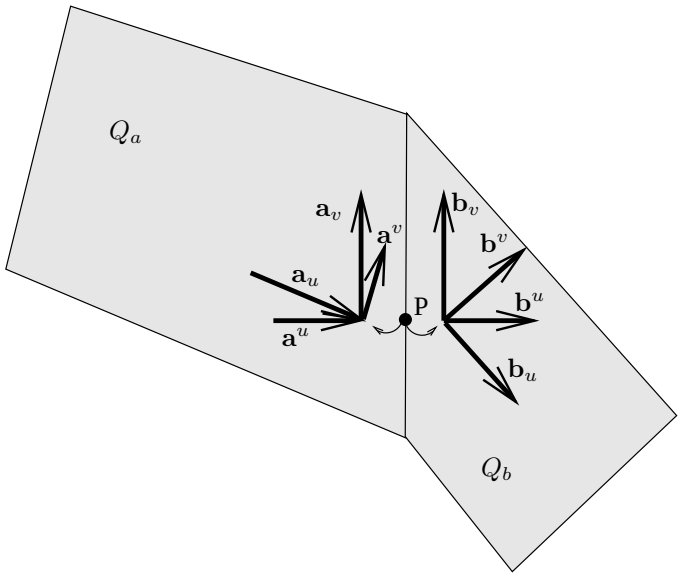

Figure B.3: *Two quadrilaterals Q_a and Q_b sharing a common edge. The covariant and contravariant unitary vectors at the point P are shown slightly displaced from P.*

The tangential continuity puts no restrictions on F_u^a and F_u^b since $\mathbf{a}^u$ and $\mathbf{b}^u$ are orthogonal to the edge. Furthermore, the tangential components of $\mathbf{F}$ are

$$F_v^a \mathbf{a}^v \cdot \frac{\mathbf{a}_v}{|\mathbf{a}_v|} = \frac{F_v^a}{|\mathbf{a}_v|}, \quad \text{in } Q_a, \tag{B.23}$$

$$F_v^b \mathbf{b}^v \cdot \frac{\mathbf{b}_v}{|\mathbf{b}_v|} = \frac{F_v^b}{|\mathbf{b}_v|}, \quad \text{in } Q_b. \tag{B.24}$$

Since $\mathbf{a}_v = \mathbf{b}_v$, tangential continuity can be imposed by enforcing

$$F_v^a = F_v^b. \tag{B.25}$$

Clearly, the covariant projection in (B.22) is the appropriate choice when tangential continuity is desired. Thus, this projection is often used in the vector Helmholtz equation or in a volumetric integral equation using the electric field $\mathbf{E}$ or the magnetic field $\mathbf{H}$ as the unknown.

In analogy with the considerations above, normal continuity can be imposed if the contravariant projection in (B.21) is chosen. Normal continuity puts no restrictions on F_a^v and F_b^v since $\mathbf{a}_v$ and $\mathbf{b}_v$ are parallel to the edge. Thus, the normal components of $\mathbf{F}$ are

$$F_a^u \mathbf{a}_u \cdot \frac{\mathbf{a}^u}{|\mathbf{a}^u|} = \frac{F_a^u}{|\mathbf{a}^u|} = \frac{\mathcal{J}_{sa} F_a^u}{|\mathbf{a}_v|}, \quad \text{in } Q_a, \tag{B.26}$$

$$F_b^u \mathbf{b}_u \cdot \frac{\mathbf{b}^u}{|\mathbf{b}^u|} = \frac{F_b^u}{|\mathbf{b}^u|} = \frac{\mathcal{J}_{sb} F_b^u}{|\mathbf{b}_v|}, \quad \text{in } Q_b. \tag{B.27}$$

Here, (B.20b) was used and $\mathcal{J}_{sa}$ and $\mathcal{J}_{sb}$ are the surface Jacobians in Q_a and Q_b, respectively. Since $\mathbf{a}_v = \mathbf{b}_v$, normal continuity can be imposed by enforcing

$$\mathcal{J}_{sa} F_a^u = \mathcal{J}_{sb} F_b^u \,. \tag{B.28}$$

Normal continuity is usually imposed when surface integral equations are solved. The unknown is then the electric or magnetic surface current densities, $\mathbf{J}_s$ or $\mathbf{M}_s$. For volume integral equations, normal continuity can be imposed on the electric flux density $\mathbf{D}$ or the magnetic flux density $\mathbf{B}$. The proper projection for these four cases is the contravariant projection in (B.21) and the condition to impose normal continuity is given in (B.28).

The results of this section are summarized in Table B.2 that lists the appropriate projections and conditions to impose on the unknown quantity in integral equations (for the volumetric cases, the projections in (B.21) and (B.22) must be extended with a third curvilinear coordinate, e.g., w.). The results presented here provide simple guidelines for choosing the appropriate projection and condition to impose.

Type of integral equation	Surface	Volume	
Unknown quantity	$\mathbf{J}_s$, $\mathbf{M}_s$	$\mathbf{E}$, $\mathbf{H}$	$\mathbf{D}$, $\mathbf{B}$
Projection	(B.21)	(B.22)	(B.21)
Condition to impose	(B.28)	(B.25)	(B.28)

Table B.2: The appropriate projections and conditions to impose on various unknown quantities in integral equations.

Appendix C
Mathematical Background Material

C.1 Definition of Inner Product Space

An inner product space is a space of functions equipped with an inner product and a norm. For two functions $\mathbf{f}$ and $\mathbf{g}$ belonging to the inner product space, the inner product is a scalar quantity defined to satisfy [52]

$$\begin{aligned} \langle \mathbf{f}, \mathbf{g} \rangle &= \langle \mathbf{f}, \mathbf{g} \rangle^{\dagger} && \text{(C.1a)} \\ \langle \alpha\mathbf{f}, \beta\mathbf{g} + \mathbf{c} \rangle &= \alpha^{\dagger}\beta\langle \mathbf{f}, \mathbf{g} \rangle + \alpha^{\dagger}\langle \mathbf{a}, \mathbf{c} \rangle && \text{(C.1b)} \\ \langle \mathbf{f}, \mathbf{f} \rangle &> 0, \quad \mathbf{f} \neq 0 && \text{(C.1c)} \\ \langle \mathbf{f}, \mathbf{f} \rangle &= 0, \quad \mathbf{f} = 0\,, && \text{(C.1d)} \end{aligned}$$

where † denotes complex conjugation. The norm is then defined as

$$\|\mathbf{a}\| = \sqrt{\langle \mathbf{f}, \mathbf{f} \rangle} \tag{C.2}$$

and the "distance" between two functions is

$$d(\mathbf{f}, \mathbf{g}) = \|\mathbf{f} - \mathbf{g}\|. \tag{C.3}$$

Unless otherwise specified the inner product used in this work is defined as

$$\langle \mathbf{f}, \mathbf{g} \rangle = \int_S \mathbf{f}^{\dagger} \cdot \mathbf{g}\, dS\,. \tag{C.4}$$

The following results on operators in inner product spaces are found in [57]. A linear operator maps functions in its domain D into functions in its range R and obeys

$$\mathcal{L}(\mathbf{f} + \mathbf{g}) = \mathcal{L}\mathbf{f} + \mathcal{L}\mathbf{g}. \tag{C.5}$$

A linear operator is bounded if there exists a constant $C \geq 0$ such that

$$\|\mathcal{L}\mathbf{f}\| \leq C\|\mathbf{f}\|, \quad \text{for all } \mathbf{f} \in D. \tag{C.6}$$

A linear operator is compact if

$$\mathcal{L}\mathbf{f}^N \to \mathcal{L}\mathbf{f} \quad \text{if} \quad \mathbf{f}^N \rightharpoonup \mathbf{f}, \quad \text{for } N \to \infty. \tag{C.7}$$

The symbol '$\rightharpoonup$' indicates weak convergence and $\mathbf{f}^N$ is a sequence of functions. Weak convergence is defined as

$$\mathbf{f}^N \rightharpoonup \mathbf{f} \quad \text{if} \quad \langle \mathbf{f}^N, \mathbf{g} \rangle \to \langle \mathbf{f}, \mathbf{g} \rangle, \quad N \to \infty \,, \tag{C.8}$$

for all $\mathbf{g}$. A linear operator is self-adjoint if

$$\langle \mathcal{L}\mathbf{f}, \mathbf{g} \rangle = \langle \mathbf{a}, \mathcal{L}\mathbf{g} \rangle \,, \tag{C.9}$$

and positive definite if

$$\langle \mathbf{f}, \mathcal{L}\mathbf{f} \rangle > 0 \quad \text{for all } \mathbf{f} \neq 0. \tag{C.10}$$

The eigensolutions of an operator equation are the solutions $\mathbf{e}$ to

$$\mathcal{L}\mathbf{e} = \Lambda \mathbf{e} \,, \tag{C.11}$$

where Λ is the pertinent eigenvalue. It follows directly from (C.6) that the eigenvalues of a bounded operator are also bounded. It can be shown that every compact operator is a bounded operator. The eigenvalues of a compact operator are therefore also bounded.

C.2 Least-Squares Polynomial Approximation

With reference to [164, 20.6-2], this section explains how to obtain a least-squares polynomial approximation of a known function $f(x)$ over a given finite interval $[a; b]$. We wish to approximate $f(x)$ as

$$f(x) \approx F(x) = \sum_{n=0}^{N} a_n f_n(x)\,, \tag{C.12}$$

where $a_n$are coefficients to be determined and $f_n(x)$ are known real polynomials that satisfy the orthogonality relation

$$\int_a^b w(x) f_m(x)\, f_n(x)\, dx = 0\,, \quad m \neq n\,. \tag{C.13}$$

The coefficients a_n are chosen to minimize the weighted mean-square error

$$e^2 = \int_a^b w(x)(F(x) - f(x))^2\, dx\,, \tag{C.14}$$

where $w(x)$ is a non-negative weighting function. Then, the coefficients can be found from

$$a_n = \frac{\int_a^b w(x)\, f(x)\, f_n(x)\, dx}{\int_a^b w(x)\, f_n^2(x)\, dx}\,. \tag{C.15}$$

C.3 Legendre Polynomials

The Legendre polynomials are used extensively in this work and possess a lot of interesting properties. This section describes a few of these as given in [165] and [166].

C.3.1 Legendre's Differential Equation

Legendre functions are solutions to Legendre's differential equation,

$$(1-x^2)f''(x) - 2x\,f'(x) + n(n+1)\,f(x) = 0. \tag{C.16}$$

Specifically, for $n = 0, 1, 2, ...$, solutions to Legendre's differential equation are Legendre polynomials

$$P_n(x) = \frac{1}{2^n\,n}\frac{d^n}{dx^n}(x^2-1)^n \quad , \quad -1 \le x \le 1\,. \tag{C.17}$$

The first few special cases are

$$P_0(x) = 1 \tag{C.18}$$
$$P_1(x) = x \tag{C.19}$$
$$P_2(x) = \frac{1}{2}(3x^2-1) \tag{C.20}$$
$$P_3(x) = \frac{1}{2}(5x^3-3x) \tag{C.21}$$
$$P_4(x) = \frac{1}{8}(35x^4-30x^2+3) \tag{C.22}$$
$$P_5(x) = \frac{1}{8}(63x^5-70x^3+15x) \tag{C.23}$$
$$P_6(x) = \frac{1}{16}(231x^6-315x^4+105x^2-5) \tag{C.24}$$
$$P_7(x) = \frac{1}{16}(429x^7-693x^5+315x^3-35x). \tag{C.25}$$

C.3.2 Orthogonality Relations and Basis Property

Legendre polynomials are orthogonal in $-1 \le x \le 1$, i.e.,

$$\int_{-1}^{1} P_m(x)\,P_n(x)\,dx = \frac{2}{2n+1}\delta_{mn}, \tag{C.26}$$

where δ_{mn} is the Kronecker delta defined as

$$\delta_{mn} = \begin{cases} 1 & m = n \\ 0 & m \neq n \end{cases}. \tag{C.27}$$

The orthogonality obviously implies that Legendre polynomials are linearly independent. Consequently, the set Legendre polynomials $P_0(x)$, $P_1(x)$, ..., $P_N(x)$ is a

basis of the polynomial space of order N. By using the results of Section C.2 with $w(x) = 1$ and the orthogonality in (C.26), a function $f(x)$ can be approximated in the interval $[-1; 1]$ as

$$f(x) \approx \sum_{n=0}^{N} a_n \, P_n(x) \, , \tag{C.28}$$

where the coefficients a_n are

$$a_n = \frac{2n+1}{2} \int_{-1}^{1} f(x) \, P_n(x) \, dx. \tag{C.29}$$

C.3.3 Recurrence Formulas

Several recurrence formulas exist for Legendre polynomials [165]. The following two are the most useful when computing the basis functions defined in Chapter 3.

$$P_{n+1}(x) = \frac{1}{n+1} \left((2n+1) x P_n(x) - n P_{n-1}(x) \right) \tag{C.30a}$$

$$P'_n(x) - P'_{n-2}(x) = (2n-1) P_{n-1}(x) \tag{C.30b}$$

C.3.4 Miscellaneous Special Results

From (C.26) we also find

$$\int_{-1}^{1} P_n(x) \, dx = 2\delta_{n0} \tag{C.31a}$$

$$\int_{-1}^{1} x P_n(x) \, dx = \frac{2}{3} \delta_{n1} \, . \tag{C.31b}$$

Consequently, all Legendre polynomials with $n > 1$ have two vanishing moments. Finally, we mention the special results

$$P_n(1) = 1 \, , \tag{C.32}$$

$$P_n(-1) = (-1)^n \, , \tag{C.33}$$

$$|P_n(x)| \leq 1 \, . \tag{C.34}$$

C.4 Numerical Integration

The task of numerically integrating a known function $f(x)$ is encountered in many engineering fields. This has led to the development of several advanced schemes to perform the integration efficiently on a computer. Most of these schemes require $f(x)$ to be evaluated at certain abscissas x_n, and assigned a certain weight w_n that depend on the particular integration scheme. The integral is then approximated as

$$\int_a^b f(x)\,dx \approx \sum_{n=1}^{N} w_n\, f(x_n) \tag{C.35}$$

The classical integration schemes apply equally spaced abscissas. The most well-known classical schemes are [167, 168]

1. The midpoint rule
2. The trapezoidal rule
3. Simpson's rule
4. Newton's $\frac{3}{8}$ rule
5. Bode's rule

According to [167], the classical schemes are *useless. They are museum pieces, but beautiful ones*. The limitation of these schemes lies in the fixed abscissas. Thus, an N point scheme only provides N degrees of freedom corresponding to the choice of N weights. As a consequence, even an optimal classical N point scheme only allows polynomials of degree N or less to be integrated exactly.

Higher accuracy can be achieved if additional degrees of freedom are incorporated into the integration scheme. This is the fundamental idea of Gaussian integration that do not use equally spaced abscissas which provides additional N degrees of freedom. In fact, an N point Gaussian integration rule allows polynomials of order $2N-1$ to be integrated exactly [168]. This impressing performance makes Gaussian integration the method of choice for most practical applications, including the one at hand. In addition, Gaussian integration is based on orthogonal polynomials. By choosing polynomials that are orthogonal with a certain weighting function $w(x)$ as in (C.13), we can even incorporate integrable singularities or other non-polynomial variations into the integration scheme. Table C.1 lists some of the classical orthogonal polynomials and their associated weighting functions [168]. However, Gaussian integration schemes can be derived even if the desired weighting function is not listed in Table C.1. The task is then to generate a set of orthogonal polynomials for the given weighting function. As an example, this allows to integrate functions with logarithmic singularities which are also encountered in CEM.

The general from of the Gaussian integration scheme is

$$\int_a^b w(x)\, f(x)\,dx \approx \sum_{n=1}^{N} w_n\, f(x_n)\,. \tag{C.36}$$

	$w(x)$	Interval
Legendre	1	$-1 < x < 1$
Tschebyscheff, 1st kind	$(1-x^2)^{-\frac{1}{2}}$	$-1 < x < 1$
Tschebyscheff, 2nd kind	$(1-x^2)^{\frac{1}{2}}$	$-1 < x < 1$
Jacobi	$(1-x)^{\alpha}(1+x)^{\beta},\ \alpha, \beta > -1$	$-1 < x < 1$
Generalized Laguerre	$x^{\alpha}e^{-x},\ \alpha > -1$	$0 < x < \infty$
Hermite	e^{-x^2}	$-\infty < x < \infty$

Table C.1: Classical orthogonal polynomials and their associated weighting functions $w(x)$.

Note that the value of the weighting function $w(x_n)$ is incorporated into the integration weights and should not be evaluated during the integration. Two specific variants of Gaussian integration are used in this work; Gauss-Legendre and Gauss-Jacobi. The first is used for smooth integrals that are well approximated by polynomials ($w(x) = 1$) and the latter is used in Section 5.3 for integrals involving singular basis functions for wedges. The weighting functions is then $(1-x)^{\alpha}(1+x)^{\beta}$ where the parameters α and β are chosen from the specific wedge under consideration.

The task of computing Gaussian abscissas and weights usually involves generating a set of orthogonal polynomials and solving a set of nonlinear equations using Newton's method. A computer code that performs this task for the weighting functions listed in Table C.1 can be found in [167]. Algorithms for finding quadrature rules for arbitrary weighting functions can be found in [169]. This latter reference also included some precomputed rules for logarithmic weighting functions. Quadrature rules for triangular domains are also commonly used in CEM and a survey of such integration rules can be found in [170].

Appendix D
Krylov Subspace Methods

This chapter briefly reviews some existing iterative solvers that all belong to the large class of methods known as Krylov subspace methods. These methods are

- Full orthogonalization method
- Conjugate gradient
- Biconjugate gradient
- Conjugate gradient squared
- Biconjugate gradient stabilized
- Generalized minimal residual
- Quasi minimal residual
- Transpose-free quasi minimal residual
- Conjugate gradient normal equations

This chapter should neither be seen as a mathematically stringent introduction to Krylov subspace methods nor as a detailed explanation of their implementation. The purpose is simply to provide an idea of the concepts used in such methods. The methods reviewed here were derived by various researchers but a unified and rigorous treatment can be found in the book by Saad [24]. Krylov subspace methods are introduced in the next section followed by the full orthogonalization method. This latter method is rarely used but is very intuitive and illustrates the fundamental concepts of all the above-mentioned solvers. The more advanced solvers perform equivalent steps in a more elegant but less intuitive way and are not treated in detail.

D.1 Theory of Krylov Subspace Methods

Krylov subspace methods are iterative methods aimed at finding an approximate solution of the linear system of equations

$$\bar{\mathbf{A}}\mathbf{x} = \mathbf{b}\,, \tag{D.1}$$

where $\bar{\mathbf{A}}$ is a $N \times N$ matrix. The initial guess is denoted $\mathbf{x}_0$ and the approximate solution after m iterations is denoted $\mathbf{x}_m$. Krylov subspace methods seek an approximate solution of the form

$$\mathbf{x}_m = \mathbf{x}_0 + \boldsymbol{\delta}, \quad \boldsymbol{\delta} \in \mathcal{K}_m(\bar{\mathbf{A}}, \mathbf{r}_0) \tag{D.2}$$

where $\mathcal{K}_m(\bar{\mathbf{A}}, \mathbf{r}_0)$ is the m-dimensional Krylov subspace

$$\mathcal{K}_m(\bar{\mathbf{A}}, \mathbf{r}_0) = span\{\mathbf{r}_0, \bar{\mathbf{A}}\mathbf{r}_0, \bar{\mathbf{A}}^2\mathbf{r}_0, \ldots, \bar{\mathbf{A}}^{m-1}\mathbf{r}_0\}\,. \tag{D.3}$$

Here, $\mathbf{r}_0$ is the initial residual $\mathbf{r}_0 = \mathbf{b} - \bar{\mathbf{A}}\mathbf{x}_0$. The approximate solution is found by imposing that the residual $\mathbf{r}_m$ is orthogonal to another subspace $\mathcal{L}_m$. In matrix form this is expressed as

$$\mathbf{r}_m = \mathbf{b} - \bar{\mathbf{A}}\mathbf{x}_m = \mathbf{b} - \bar{\mathbf{A}}(\mathbf{x}_0 + \boldsymbol{\delta}) = \mathbf{r}_0 - \bar{\mathbf{A}}\boldsymbol{\delta} \perp \mathcal{L}_m\,, \tag{D.4}$$

where $\perp$ indicates orthogonality and $\mathcal{L}_m$ is an m-dimensional subspace. This condition is known as the Petrov-Galerkin condition or in the special case $\mathcal{L}_m = \mathcal{K}_m(\bar{\mathbf{A}}, \mathbf{r}_0)$, the Galerkin condition[1]. Let $\bar{\mathbf{V}}_m$ be an $N \times m$ matrix whose column vectors form a basis of $\mathcal{K}_m$. This imply that $\boldsymbol{\delta}$ can be written as

$$\boldsymbol{\delta} = \bar{\mathbf{V}}_m \mathbf{y}_m\,, \tag{D.5}$$

where $\mathbf{y}_m$ is a vector with coefficients to be determined. The orthogonality condition in (D.4) is then expressed as

$$\left\langle \mathbf{r}_0 - \bar{\mathbf{A}}\bar{\mathbf{V}}_m\mathbf{y}_m, \mathbf{w} \right\rangle = 0 \quad \text{for all } \mathbf{w} \in \mathcal{L}_m\,, \tag{D.6}$$

where the inner product $\langle \cdot, \cdot \rangle$ is defined as

$$\langle \mathbf{f}, \mathbf{g} \rangle = \sum_{i=1}^{N} f_i g_i^{\dagger} \tag{D.7}$$

where † denotes complex conjugation. Let $\bar{\mathbf{W}}_m$ be an $N \times m$ matrix whose column vectors form a basis of $\mathcal{L}_m$. (D.6) then implies

$$\bar{\mathbf{W}}^H\bar{\mathbf{A}}\bar{\mathbf{V}}_m\mathbf{y}_m = \bar{\mathbf{W}}^H\mathbf{r}_0 \quad \Rightarrow \quad \mathbf{y}_m = (\bar{\mathbf{W}}^H\bar{\mathbf{A}}\bar{\mathbf{V}}_m)^{-1}\bar{\mathbf{W}}^H\mathbf{r}_0\,. \tag{D.8}$$

From (D.2), (D.5), and (D.8), the approximate solution is found as

$$\mathbf{x}_m = \mathbf{x}_0 + \bar{\mathbf{V}}_m\mathbf{y}_m = \mathbf{x}_0 + \bar{\mathbf{V}}_m(\bar{\mathbf{W}}^H\bar{\mathbf{A}}\bar{\mathbf{V}}_m)^{-1}\bar{\mathbf{W}}^H\mathbf{r}_0\,. \tag{D.9}$$

This expression is rarely used in practical implementations since most Krylov subspace methods do not need to generate the product $\bar{\mathbf{W}}^H\bar{\mathbf{A}}\bar{\mathbf{V}}_m$ explicitly. However,

[1]Note that a Krylov subspace method has some similarities with MoM. Both methods are projection methods that project an unknown quantity onto a finite-dimensional subspace by imposing orthogonality with some additional subspace. Consequently, when Galerkin testing is not used in MoM, it would be natural to use the term *Petrov-Galerkin testing*.

the iterative process is now easy to understand. The approximate solution after m iterations is simply a vector that belongs to the m-dimensional Krylov subspace $\mathcal{K}_m$ and chosen to ensure that the residual vector is orthogonal to $\mathcal{L}_m$. These conditions are enforced by choosing the approximate solution as in (D.9).

There is an alternative interpretation of the solution obtained by the Krylov subspace methods. It is clear from (D.3) that the approximate solution is of the form

$$\mathbf{x}_m = \mathbf{x}_0 + p_{m-1}(\bar{\mathbf{A}})\mathbf{r}_0\,, \tag{D.10}$$

where $p_{m-1}(\bar{\mathbf{A}})$ is a polynomial of order $m-1$. If the initial guess is zero, this implies

$$\mathbf{x}_m = p_{m-1}(\bar{\mathbf{A}})\mathbf{b} \approx \bar{\mathbf{A}}^{-1}\mathbf{b}\,. \tag{D.11}$$

Thus, the Krylov subspace methods approximate $\bar{\mathbf{A}}^{-1}$ by the polynomial $p_{m-1}(\bar{\mathbf{A}})$.

The various Krylov subspace methods correspond to different choices of $\mathcal{L}_m$. The common choices are $\mathcal{L}_m = \mathcal{K}_m(\bar{\mathbf{A}}, \mathbf{r}_0)$, $\mathcal{L}_m = \bar{\mathbf{A}}\mathcal{K}_m(\bar{\mathbf{A}}, \mathbf{r}_0)$, and $\mathcal{L}_m = \mathcal{K}_m(\bar{\mathbf{A}}^H, \mathbf{r}_0)$, where ^{H} denotes the complex conjugate of the transposed matrix. In addition, the bases of $\mathcal{K}_m(\bar{\mathbf{A}}, \mathbf{r}_0)$ and $\mathcal{L}_m$ can be generated in different ways, giving rise to some additional methods. All these methods generate different polynomials p_{m-1} and consequently different approximations. Unfortunately, it is generally not possible to determine the most efficient method for a given problem. In fact, according to [171], for any of the methods CG, BICG, CGS, and GMRES, *there is a class of problems for which a given method is the winner and another one is the loser*. The choice of method is therefore nearly always based on experience.

The iterative solution process is stopped when a certain error criterion is met but different criterions exist in the literature. Throughout this work, the error criterion is based on the relative error defined as

$$e_m = \frac{\|\mathbf{r}_m\|}{\|\mathbf{b}\|}, \tag{D.12}$$

where $\|\cdot\|$ denotes the 2-norm. Consequently, the iterative algorithm is terminated when e_m drops below a certain predefined level.

D.1.1 Arnoldi's Procedure

The so-called Arnoldi Procedure generates an orthogonal basis of the Krylov subspace $\mathcal{K}_m(\bar{\mathbf{A}}, \mathbf{v}_1)$ and is a basic building block in Krylov subspace methods.

1. Choose v_1 such that $\|\mathbf{v}_1\| = 1$
2. For $j = 1, 2, \ldots, m$ do:
3. $\quad h_{ij} = \langle \bar{\mathbf{A}}\mathbf{v}_j, \mathbf{v}_i \rangle$, $i = 1, 2, \ldots, j$
4. $\quad \mathbf{v}_{j+1} = \bar{\mathbf{A}}\mathbf{v}_j - \sum_{i=1}^{j} h_{ij}\mathbf{v}_i$
5. $\quad h_{j+1,j} = \|\mathbf{v}_{j+1}\|$

6. $\mathbf{v}_{j+1} = \mathbf{v}_{j+1}/h_{j+1,j}$
7. End do

The steps 3-6 are just a standard Gramm-Schmidt procedure which ensures that $\mathbf{v}_j$, $j = 1, 2, \ldots, m$, are orthonormal. Step 4 defines the next vector in the basis set $\mathbf{v}_{j+1}$, and it its seen that this vector is one order higher in terms of $\bar{\mathbf{A}}$ than $\mathbf{v}_j$. Thus, $\mathbf{v}_1$, $\mathbf{v}_2$, $\ldots$, $\mathbf{v}_m$ form a basis of the Krylov subspace

$$\mathcal{K}_m(\bar{\mathbf{A}}, \mathbf{v}_1) = span\{\mathbf{v}_1, \bar{\mathbf{A}}\mathbf{v}_1, \bar{\mathbf{A}}^2\mathbf{v}_1, \ldots, \bar{\mathbf{A}}^{m-1}\mathbf{v}_1\}\,. \tag{D.13}$$

The h_{ij}'s computed in the Arnoldi procedure define an $m \times m$ matrix $\bar{\mathbf{H}}_m$ whose elements satisfy $h_{ij} = 0$ if $i > j + 1$. It can be shown that

$$\bar{\mathbf{H}}_m = \bar{\mathbf{V}}_m^H \bar{\mathbf{A}} \bar{\mathbf{V}}_m\,. \tag{D.14}$$

D.2 Overview of Krylov Subspace Methods

D.2.1 Full Orthogonalization Method (FOM)

The FOM chooses $\mathcal{L}_m = \mathcal{K}_m(\bar{\mathbf{A}}, \mathbf{r}_0)$ in (D.4). This allows (D.8) to be simplified to

$$\mathbf{y}_m = (\bar{\mathbf{V}}_m^H \bar{\mathbf{A}} \bar{\mathbf{V}}_m)^{-1} \bar{\mathbf{V}}_m^T \mathbf{r}_0 = \bar{\mathbf{H}}_m^{-1} \bar{\mathbf{V}}_m^T \mathbf{r}_0,\,. \tag{D.15}$$

The solution $\mathbf{x}_m$ in the m-dimensional Krylov subspace is then found from (D.9) by using the Arnoldi procedure to generate $\bar{\mathbf{V}}_m$ and $\bar{\mathbf{H}}_m$. The FOM algorithm is then

1. Choose $\mathbf{r}_0 = \mathbf{b} - \bar{\mathbf{A}}\mathbf{x}_0$ and $\mathbf{v}_1 = \mathbf{r}_0/\|\mathbf{r}_0\|$
2. For $j = 1, 2, \ldots, m$ do:
3. Use Arnoldi's procedure to compute $\bar{\mathbf{V}}_m$ and $\bar{\mathbf{H}}_m$
4. Compute $\mathbf{y}_m = \bar{\mathbf{H}}_m^{-1} \bar{\mathbf{V}}_m^T \mathbf{r}_0$
5. Compute $\mathbf{x}_m = \mathbf{x}_0 + \bar{\mathbf{V}}_m \mathbf{y}_m$
6. End do

The accuracy of the approximate solution improves as the dimension m of the subspace increases. In practical situations, the required value of m is not known in advance. However, for a given m, the Arnoldi procedure does not need to go through the time-consuming task of computing $\bar{\mathbf{V}}_m$ and $\bar{\mathbf{H}}_m$ from the beginning. Instead, the procedure just performs one matrix-vector product, adds one column to $\bar{\mathbf{V}}_{m-1}$, and one column and one row to $\bar{\mathbf{H}}_m$. Naturally, the exact solution is reached after $m = N$ iterations since the dimension of the Krylov subspace is then equal to that of $\bar{\mathbf{A}}$. However, due to computer rounding errors, convergence is not guaranteed for practical problems. In addition, the memory requirement grows linearly with m due to the need for storing $\bar{\mathbf{V}}_m$ and $\bar{\mathbf{H}}_m$. Thus, m should be kept low which is usually done by restarting the algorithm after $m = M$ iterations. The solution $\mathbf{x}_M$ is then used as initial guess $\mathbf{x}_0$ and the procedure is repeated. The restarted FOM thus requires much less memory but convergence is not guaranteed, even if computer rounding errors are not present.

D.2.2 Conjugate Gradient (CG)

The CG algorithm is mathematically equivalent to FOM but requires that $\bar{\mathbf{A}}$ is symmetric and positive definite. Thus, the CG algorithm also use the choice $\mathcal{L}_m = \mathcal{K}_m(\bar{\mathbf{A}}, \mathbf{r}_0)$. However, the symmetry of $\bar{\mathbf{A}}$ allows for significant simplifications leading to a much more elegant algorithm. Most importantly, it eliminates the need for storing $\bar{\mathbf{V}}_m$ and $\bar{\mathbf{H}}_m$ which implies that memory requirements do not increase with m. Consequently, the CG converges in no more than N iterations if no rounding errors are present. For practical implementations, it might converge very slow or even diverge due to buildup of rounding errors. The CG uses just one matrix-vector multiplication per iteration and its simplicity has made it immensely popular.

D.2.3 Biconjugate Gradient (BICG)

The biconjugate gradient (BiCG) is similar to CG, except that $\mathcal{L}_m$ in (D.4) is chosen as

$$\mathcal{L}_m = span\{\mathbf{w}_1, \bar{\mathbf{A}}^H\mathbf{w}_1, (\bar{\mathbf{A}}^H)^2\mathbf{w}_1, \ldots, (\bar{\mathbf{A}}^H)^{m-1}\mathbf{w}_1\}\,, \tag{D.16}$$

where $\mathbf{w}_1$ is usually taken as $\mathbf{r}_0$. BICG then employs biorthogonalization instead of the orthogonalization used in CG, i.e., it generates the biorthogonal vectors

$$\langle \mathbf{v}_i, \mathbf{w}_j \rangle = 0, \quad i \neq j, \quad i, j = 1, 2, \ldots, m. \tag{D.17}$$

Compared to CG, BICG has the advantage that it works for non-symmetric $\bar{\mathbf{A}}$. However, BICG requires two matrix-vector products per iteration, one with $\bar{\mathbf{A}}$ and one with $\bar{\mathbf{A}}^H$. In fact, BICG solves a dual system with $\bar{\mathbf{A}}^H$ as a byproduct. The relative error e_m may not decrease monotonically since the residual vector is made orthogonal to $\mathcal{K}_m(\bar{\mathbf{A}}^H, \mathbf{r}_0)$, not $\mathcal{K}_m(\bar{\mathbf{A}}, \mathbf{r}_0)$. The memory requirements are modest.

D.2.4 Conjugate Gradient Squared (CGS)

The conjugate gradient squared (CGS) [98] is a variant of BICG that eliminates the need for the transpose matrix-vector product. Thus, CGS also uses the choice $\mathcal{L}_m = \mathcal{K}_m(\bar{\mathbf{A}}^H, \mathbf{r}_0)$ in (D.4). The algorithm is based on the observation that the residual vector after m BICG iterations can be written as a m-th order polynomial in $\bar{\mathbf{A}}$ and that this polynomial appears squared. It is then possible to establish a recurrence formula for this squared polynomial. Compared to BICG, the CGS algorithm still requires two matrix-vector products per iteration but should converge twice as fast. However, if BICG diverges, CGS diverges twice as fast. CGS is very fast for some problems but usually exhibits irregular convergence behavior and is very sensitive to buildup of rounding errors.

D.2.5 Biconjugate Gradient Stabilized (BICGSTAB)

The Biconjugate Gradient Stabilized (BICGSTAB) [99] is based on CGS but attempts to smoothen the irregular convergence. This is done by multiplying the CGS polynomial with an additional polynomial $\psi_m(\bar{\mathbf{A}})$ defined by the recurrence $\psi_{m+1}(\bar{\mathbf{A}}) =$

$(\bar{\mathbf{I}} - \omega_m \bar{\mathbf{A}})\psi_m(\bar{\mathbf{A}})$ where ω_m is a factor determined in each iteration and $\bar{\mathbf{I}}$ is the identity matrix. The resulting algorithm is more stable and provides much smoother convergence than CGS. However, the error is generally not decaying monotonically. BICGSTAB requires two matrix-vector products per iteration.

D.2.6 Generalized Minimal Residual (GMRES)

The generalized minimal residual (GMRES) [97] chooses $\mathcal{L}_m = \bar{\mathbf{A}}\mathcal{K}_m(\bar{\mathbf{A}}, \mathbf{r}_0)$ in (D.4). This choice implies that the error e_m is minimized in each step[2]. The procedure is similar to the FOM, except that step 4 in section D.2.1 is replaced with a least-squares problem. The drawback of GMRES is the need for storing $\bar{\mathbf{V}}_m$ and $\bar{\mathbf{H}}_m$. The storage requirement grows as $Nm + m^2$ and may become prohibitively large if many iterations are needed. To avoid this, the GMRES is often restarted after relatively few iterations. The algorithm is then referred to as GMRES(M) where M is the number of iterations before each restart. The error decays monotonically with the number of iterations. However, buildup of rounding errors can cause the algorithm to stagnate.

D.2.7 Quasi-Minimal Residual (QMR)

The quasi-minimal residual (QMR) algorithm is similar to GMRES, except that bi-orthogonalization is used instead of orthogonalization. This implies that the basis vectors $\bar{\mathbf{V}}_m$ are not orthogonal to $\bar{\mathbf{A}}\mathcal{K}_m(\bar{\mathbf{A}}, \mathbf{r}_0)$ but is still makes sense to minimize the residual as in the GMRES, hence the name quasi-minimal residual. The QMR method has the significant advantage that the large memory requirement of GMRES is avoided. However, it requires two matrix-vector products per iteration, one with $\bar{\mathbf{A}}$ and one with $\bar{\mathbf{A}}^H$.

D.2.8 Transpose-Free QMR (TFQMR)

The TFQMR method [100] is derived from CGS but imposes a quasi-minimal residual as QMR. However, the matrix-vector product with $\bar{\mathbf{A}}^H$ is not needed which speeds up the solution considerably. The convergence is often considerably smoother than CGS but the error does not decay monotonically. Loosely speaking, TFQMR almost minimizes the residual but does not require the additional storage and least square solution of GMRES.

D.2.9 CG Normal Equations (CGNR)

The CGNR algorithm exploits that $\bar{\mathbf{A}}^H\bar{\mathbf{A}}$ is always symmetric and positive definite. Thus, the standard CG algorithm can be used to solve the system

$$\bar{\mathbf{A}}^H\bar{\mathbf{A}}\mathbf{x} = \bar{\mathbf{A}}^H\mathbf{b}\,, \tag{D.18}$$

which has the same solution as (D.1). The expression in (D.18) is referred to as the normal equation and CGNR is similar to GMRES in the sense that e_m is minimized at

[2]Note the similarities of GMRES and the least-square variant of MoM described in Subsection 2.3.1

each step. This does not imply that $\mathbf{x}_m$ are the same with the two methods because the bases of the Krylov subspaces are chosen in a different way. In fact, the convergence of the CGNR is governed by the matrix $\bar{\mathbf{A}}^H \bar{\mathbf{A}}$. The condition number of this matrix is the square of the condition number of $\bar{\mathbf{A}}$. Thus, it is almost always better to use another method [167]. In addition, it is generally hard to find a good preconditioner for $\bar{\mathbf{A}}^H \bar{\mathbf{A}}$ without computing the product explicitly.

Appendix E
Description of Computer Codes

In the course of this work, a software package for analysis of electromagnetic scattering and radiation from 3-D conducting objects has been developed. The package was named HOPES which is an acronym for Higher-Order Parallel Electromagnetic Simulator. HOPES consists of a simulation core, an OpenGL-based 3-D graphical viewer, and various utility programs. This appendix gives a short description of the HOPES simulation core and the viewer.

E.1 The HOPES Core

HOPES can solve the following types of integral equations:

- EFIE
- MFIE
- CFIE
- EFIE/MFIE or EFIE/CFIE on objects with both open and closed parts
- Hybrid EFIE/PO

A very efficient solution is obtained by employing higher-order hierarchical Legendre basis functions of arbitrary order that were designed to keep the matrix condition number low. The expansion order is automatically adapted to the electrical size of each element which allows both large smooth surfaces and small geometrical details to be handled efficiently. The elements that are supported by HOPES are listed in Table E.1. General 3-D objects can be analyzed by supplying the core with a mesh file defining the object as a combination of elements. The mesh file can be obtained in different ways:

- HOPES is compatible with the commercial meshing tools MSC-Patran [172] and GiD [173]. This open the possibility of meshing structures defined in various CAD formats.
- HOPES has its own simple format for defining objects. This allows the user to specify objects by hand. Alternatively, the user can develop scripts or programs that perform the task.

	Order	Number of vertices
Bilinear quadrilateral	1st	4
Curved quadrilateral	2nd	9
Flat triangle	1st	3
Curved triangle	2nd	7
Straight wire	1st	2
Curved wire	2nd	3

Table E.1: *Geometrical elements used in HOPES.*

- Several utility functions provide meshing capabilities of simple structures, such as boxes, spheres, tubes, cylinders, discs, or plates.

HOPES processes the supplied mesh file and subdivides the elements until no edge or wire is longer than a predefined limit, usually around 2.5λ. If more than two surface elements have a common edge, or more than two wires have a common vertex, a junction is formed. The core detects this and enforces continuity of currents at the junction. If a wire element has a vertex on a surface element, a wire-surface junction is formed and current continuity enforced. This type of junction is handled with the generalized localized junction model [15].

Currently, HOPES works with electric surface currents only. Thus, the objects that can be analyzed are limited to perfectly conducting bodies or objects that can be treated with an impedance boundary condition. The surface impedance can be specified separately for each element of the mesh.

By default HOPES assumes that the object is located in an infinite homogeneous medium and the constitutive parameters of the medium can be specified, including losses. However, the user can supply a routine with a dyadic Green's function for other media. This implies that HOPES can be used to analyze objects located in multilayered media or other environments, e.g., waveguides or cavities. The results presented in Subsection 7.2 were obtained with a dyadic Green's function included in this way.

HOPES can solve both scattering and radiation problems and supports various types of excitations:

- Plane waves
- Impressed infinitesimal electric or magnetic currents (arbitrary number)
- Line voltage generators on edges between patches (arbitrary number)
- Point voltage generators at wire nodes (arbitrary number)
- General measured or simulated fields as a user-supplied set of spherical wave coefficients (see [96] for the definition of the coefficients.).

HOPES supports both direct and iterative equation solvers:

- Direct LU decomposition algorithm for serial execution or parallel execution on shared memory machines.

- Direct Block-LU decomposition algorithm for parallel execution on distributed memory systems.

- Iterative solvers for serial execution or parallel execution on shared memory machines. Usually, the restarted GMRES is recommended. BICGSTAB and TFQMR may also be competitive for some configurations.

The iterative solvers employ various efficient preconditioners; Overlapping group, non-overlapping group, incomplete LU, and additive Schwarz preconditioner with polynomial space decomposition.

HOPES can operate at a single frequency or perform a frequency sweep. At each frequency, an expansion of the electric surface current density on the object is obtained. From this current density, several types of outputs can be calculated:

- Surface current density along any piecewise straight curve on the object, including wires.

- Surface current density as 3-D color plots viewable by the HOPES viewer

- Monostatic or bistatic radar cross section (available as theta- or phi cuts, or max-min dynamic spread curves)

- Far fields as theta- or phi cuts, or max-min dynamic spread curves. Normalization to obtain directivity is possible.

- Near fields along any piecewise linear curve or as theta- or phi cuts at a specified distance.

- Radiated and delivered power.

- Generator input impedance.

- 3-D view of active regions in antenna configurations (using farfield analysis of radiating sources (FARS) [174]).

Furthermore, HOPES stores the calculated current as well as other relevant parameters in a binary file. This file can be read by HOPES to calculate additional outputs without the need for solving the problem again. The binary file can also be read by the HOPES viewer.

HOPES can be executed in parallel on both distributed and shared memory systems. The code is highly portable and has currently been tested on the hardware platforms listed in Table E.2.

	Operating sys.	Maximum CPUs tested
Intel Pentium SMP	Linux	2
Intel Pentium Cluster	Linux	16
Intel Pentium	Windows	1
Intel Itanium SMP	Linux	4
SUN Ultrasparc III	SUN OS	32
SGI Origin 2000	Unix	2

Table E.2: *Hardware platforms and operating systems where HOPES has been tested.*

E.2 The HOPES Viewer

The HOPES viewer is an OpenGL-based graphical tool for visualizing meshes and calculated surface currents in 3-D. This provides a convenient way to inspect meshes both before and after the processing done by the HOPES core. The viewer has options for visualizing surface elements, surface normal vectors, element edges, external element edges, wires, external wire nodes, wire-surface junctions, PO regions, and the groups used by the preconditioners. Basic manipulations such as rotating, translating, and scaling are supported. The input can be in the form of a mesh file (MSC-Patran, GiD, or HOPES format) as well as binary output files from the HOPES core. In this latter case, the calculated surface current can be shown. It is possible to show separate cartesian components of the current, the surface charge density, or the active regions as calculated by FARS. The viewable output can be saved to a file for inclusion into documents which was used to generate many of the figures shown in this thesis.

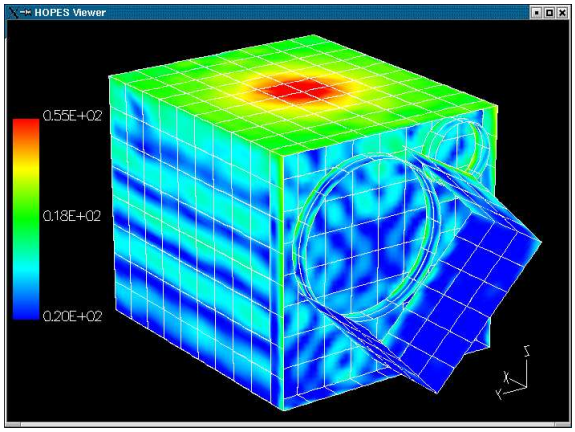

Figure E.1: *Screen capture of the HOPES viewer visualizing the induced current on a simple model of the Danish Rømer satellite.*

Bibliography

[1] **R. F. Harrington**, *Field Computation by Moment Methods*, Macmillan, New York, 1968.

[2] **A. W. Glisson and D. R. Wilton**, Simple and efficient methods for problems of electromagnetic radiation and scattering from surfaces, *IEEE Trans. Antennas Propagat.*, vol. AP-28, no. 4, pp. 593–603, Sep. 1980.

[3] **S. M. Rao, D. R. Wilton, and A. W. Glisson**, Electromagnetic scattering by surfaces of arbitrary shape, *IEEE Trans. Antennas and Propagation*, vol. AP-30, no. 3, pp. 409–418, May 1982.

[4] **J. C. Nedelec**, Mixed finite element in R^3, *Numer. Mathem.*, vol. 35, pp. 315–341, 1980.

[5] **S. Wandzura**, Electric current basis functions for curved surfaces, *Electromagnetics*, vol. 12, pp. 77–91, 1992.

[6] **B. M. Kolundžija and B. D. Popović**, Entire-domain Galerkin method for analysis of metallic antennas and scatterers, *IEE Proceedings-H*, vol. 140, no. 1, pp. 1–10, Feb. 1993.

[7] **R. D. Graglia, D. R. Wilton, and A. F. Peterson**, Higher order interpolatory vector bases for computational electromagnetics, *IEEE Trans. Antennas Propagat.*, vol. 45, no. 3, pp. 329–342, March 1997.

[8] **B. D. Popović and B. M. Kolundžija**, *Analysis of Metallic Antennas and Scatterers*, The Institution of Electrical Engineers, London, UK, 1994.

[9] **L. R. Hamilton, P. A. Macdonald, M. A. Stalzer, R. S. Turley, J. L. Visher, and S. M. Wandzura**, Electromagnetic scattering computations using high-order basis functions in the method of moments, *Proc. of the 1994 IEEE Antennas Propagat. Soc. Int. Symp.*, vol. IV, pp. 2166–2169, Ann Arbor, MI, USA, July 1994.

[10] **K. R. Aberegg, A. Taguchi, and A. F. Peterson**, Application of higher-order vector basis functions to surface integral equation formulations, *Radio Science*, vol. 31, no. 5, pp. 1207–1213, Sep.-Oct. 1996.

[11] **B. M. Notaroš and B. D. Popović**, General entire-domain method for analysis of dielectric scatterers, *IEE Proc.-Microw. Antennas Propag.*, vol. 143, no. 6, pp. 498–504, Dec. 1996.

[12] **W. Cai, T. Yu, H. Wang, and Y. Yu**, High-order mixed RWG basis functions for electromagnetic applications, *IEEE Trans. om Microwave Theory and Techniques*, vol. 49, no. 7, pp. 1295–1303, July 2001.

[13] **B. M. Notaroš, B. D. Popović, J. P. Weem, R. A. Brown, and Z. Popović**, Efficient large-domain MoM solution to electrically large EM problems, *IEEE Trans. om Microwave Theory and Techniques*, vol. 49, no. 1, pp. 151–159, Jan. 2001.

[14] **M. Djordević and B. M. Notaroš**, Three types of higher-order MoM basis functions automatically satisfying current continuity conditions, *Proc. of the 2002 IEEE Antennas Propagat. Soc. Int. Symp.*, vol. IV, pp. 610–613, San Antonio, TX, USA, June 2002.

[15] **B. M. Kolundžija and B. D. Popović**, Generalized localized junction model in the analysis of wire-to-plate junctions, *IEE Proceedings-H*, vol. 141, no. 1, pp. 1–7, Feb. 1994.

[16] **B. M. Kolundžija**, On the locally continous formulation of surface doublets, *IEEE Trans. Antennas Propagat.*, vol. 46, no. 12, pp. 1879–1883, Dec. 1998.

[17] —, Accurate solution of square scatterer as benchmark for validation of electromagnetic modeling of plate structures, *IEEE Trans. Antennas Propagat.*, vol. 46, no. 7, pp. 1009–1014, July 1998.

[18] —, Electromagnetic modeling of composite metallic and dielectric structures, *IEEE Trans. Antennas Propagat.*, vol. 47, no. 7, pp. 1021–1032, July 1999.

[19] **R. Coifman, V. Rokhlin, and S. Wandzura**, The fast multipole method for the wave equation: A pedestrian prescription, *IEEE Ant. Propagat. Magazine*, vol. 35, no. 3, pp. 7–12, June 1993.

[20] **B. Kolundžija and T. Sarkar**, Iterative solvers in frequency analysis of complex structures based on MoM solution of surface integral equations, *Proceedings of the 2001 IEEE Antennas and Propagation Soc. Int. Symp.*, vol. 2, pp. 588–591, Boston, MA, July 2001.

[21] **T. K. Sarkar, K. R. Siarkiewicz, and R. F. Stratton**, Survey of numerical methods for solution of large systems of linear equations for electromagnetic field problems, *IEEE Trans. Antennas Propagat.*, vol. AP-29, no. 6, pp. 847–856, Nov. 1981.

[22] **T. K. Sarkar and E. Arvas**, On a class of finite step iterative methods (conjugate directions) for the solution of an operator equation arising in electromagnetics, *IEEE Trans. Antennas Propagat.*, vol. AP-33, no. 10, pp. 1058–1066, Oct. 1985.

[23] **A. F. Peterson and R. Mittra**, Convergence of the conjugate gradient method when applied to matrix equations representing electromagnetic scattering problems, *IEEE Trans. Antennas and Propagation*, vol. AP-34, no. 12, pp. 1447–1454, Dec. 1986.

[24] **Y. Saad**, *Iterative Methods for Sparse Linear Systems*, PWS Publishing Company, Boston, MA., 1996, Second edition freely available from http://www-users.cs.umn.edu/˜saad/books.html.

[25] **J. Van Bladel**, *Singular Electromagnetic Fields and Sources*, Clarendon Press, Oxford, UK, 1991.

[26] **T. Andersson**, Moment-method calculations of scattering by a square plate using singular basis functions and a multipole expansion, *Jour. of Electromagnetic Waves and Applications*, vol. 7, no. 1, pp. 93–121, 1993.

[27] —, Moment-method calculations on apertures using singular basis functions, *IEEE Trans. Antennas Propagat.*, vol. 41, no. 12, pp. 1709–1716, Jan. 1993.

[28] **D. R. Wilton and S. Govind**, Incorporation of edge conditions in moment method solutions, *IEEE Trans. Antennas Propagat.*, vol. AP-25, no. 6, pp. 845–850, Nov. 1977.

[29] **B. M. Kolundžija**, On the inclusion of edge effects into surface vector basis functions, *Proceedings of the 1998 AP-S Symposium*, pp. 282–285, July 1998.

[30] **R. D. Graglia and G. Lombardi**, Vector functions for singular fields on curved triangular elements, truly defined in the parent space, *Proceedings of the 2002 IEEE Antennas and Propagation Soc. Int. Symp.*, vol. 1, pp. 62–65, San Antonio, TX, July 2002.

[31] **U. Jakobus and F. M. Landstorfer**, Improved PO-MM hybrid formulation for scattering from three-dimensional perfectly conducting bodies of arbitrary shape, *IEEE Trans. Antennas Propagat.*, vol. 43, no. 2, pp. 162–169, Feb. 1995.

[32] —, Improvement of the PO-MoM hybrid method by accounting for effects of perfectly conducting wedges, *IEEE Trans. Antennas Propagat.*, vol. 43, no. 10, pp. 1123–1129, Oct. 1995.

[33] **E. Jørgensen, J. L. Volakis, P. Meincke, and O. Breinbjerg**, Higher-order hierarchical legendre basis functions for electromagnetic modeling, submitted to IEEE Transactions on Antennas and Propagation, Feb. 2003.

[34] —, Higher order hierarchical Legendre basis functions for iterative integral equation solvers with curvilinear surface modeling, *2002 IEEE Antennas Propagat. Soc. Int. Symp.*, vol. IV, pp. 618–621, San Antonio, TX, USA, June 2002.

[35] —, Divergence-conforming higher order hierarchical basis functions and preconditioning strategies for boundary integral operators, *6th Int. Workshop on Finite Elements in Microw. Eng.*, p. 63, Chios, Greece, May 2002.

[36] **E. Jørgensen, P. Meincke, and O. Breinbjerg**, A hybrid PO - higher-order hierarchical MoM formulation using curvilinear geometry modeling, Accepted for publication at 2003 Int. Symp. on Antennas and Propagation, Columbus, OH, USA, June 2003.

[37] —, An improved hybrid physical optics - moment method technique using higher-order basis functions, Accepted for publication at PIERS 2003, Honolulu, Hawai, USA, Oct. 2003.

[38] **E. Jørgensen, O. Kim, P. Meincke, and O. Breinbjerg**, Higher-order hierarchical discretization scheme for surface integral equations for layered media, submitted to IEEE Geoscience and Remote Sensing, Feb. 2003.

[39] **J. L. Volakis, K. Sertel, E. Jørgensen, and R. W. Kindt**, Hybrid finite element and volume integral methods for scattering using parametric geometry, submitted to CMES - Computer Modeling in Engineering and Sciences, July 2002.

[40] **O. S. Kim, E. Jørgensen, P. Meincke, and O. Breinbjerg**, Efficient CFIE-MoM analysis of 3-D PEC scatterers in layered media, *Conference Proceedings, 2002 International Conference on Mathematical Methods in Electromagnetic Theory, MMET*02*, vol. 2, pp. 476–478, Kiev, Ukraine, Sep. 2002.

[41] —, Analysis of PEC objects in layered media using higher-order hierarchical basis functions, *Proceedings of the 19th Annual Review of Progress in Applied Computational Electromagnetics*, pp. 351–356, Monterey, CA, USA, March 2003.

[42] —, Solution of volume integral equations using higher-order hierarchical Legendre basis functions, Accepted for publication at PIERS 2003, Honolulu, Hawai, USA, Oct. 2003.

[43] **J. L. Volakis, A. Chatterjee, and L. C. Kempel**, *Finite Element Method for Electromagnetics*, IEEE Press, New York, USA, 1998.

[44] **A. Taflove and S. C. Hagness**, *Computational Electrodynamics: The Finite-Difference Time-Domain Method*, Artech House, Norwood, MA, USA, 2 edn., 2000.

[45] **C. Christopoulos**, *Transmission-Line Modeling Method: TLM*, IEEE Press, New York, USA, 1995.

[46] **L. M. Delves and J. Walsh**, *Numerical Solution of Integral Equations*, Oxford University Press, Oxford, UK, 1974.

[47] **J. Strain**, Locally-corrected multidimensional quadrature rules for singular functions, *SIAM J. Sci. Comput.*, vol. 16, no. 4, pp. 992–1017, 1995.

[48] **C. Hafner**, *The Generalized Multipole Technique for Computational Electromagnetics*, Artech House, Norwood, MA, USA, 1990.

[49] **D. I. Kaklamani and H. T. Anastassiu**, Aspects of the method of auxiliary sources (MAS) in computational electromagnetics, *IEEE Antennas Propagat. Magazine*, vol. 44, no. 3, pp. 48–64, June 2002.

[50] **D. P. Bouche, F. A. Molinet, and R. Mittra**, *Asymptotic Methods in Electromagnetics*, Springer-Verlag, Berlin, Germany, 1997.

[51] **K. Sertel and J. L. Volakis**, Comparison of finite element-boundary integral and volume integral equation methods for modeling inhomogeneous targets, *6th Int. Workshop on Finite Elements in Microw. Eng.*, p. 70, Chios, Greece, May 2002.

[52] **A. F. Peterson, S. C. Ray, and R. Mittra**, *Computational Methods for Electromagnetics*, IEEE Press, New York, USA, 1998.

[53] **J. L. Volakis**, Alternative field representations and integral equations for modeling inhomogeneous dielectrics, *IEEE Trans. Microwave Theory Tech.*, vol. 40, no. 3, pp. 604–608, Mar. 1991.

[54] **A. Herschlein, J. v. Hagen, and W. Wiesbeck**, Methods for the evaluation of regular, weakly singular, and strongly singular surface reaction integrals arising in method of moments, *Applied Computational Electromagnetics Society (ACES) Journal*, vol. 17, no. 1, pp. 63–73, Mar. 2002.

[55] **T. K. Sarkar**, A note on the choice of weighting functions in the method of moments, *IEEE Trans. Antennas Propagat.*, vol. AP-33, no. 4, pp. 436–441, April 1985.

[56] **G. C. Hsiao and R. E. Kleinman**, Mathematical foundations for error estimation in numerical solutions of integral equations in electromagnetics, *IEEE Trans. Antennas Propagat.*, vol. 45, no. 3, pp. 316–328, March 1997.

[57] **B. L. Moiseiwitsch**, *Integral Equations*, Longman, London, UK, 1977.

[58] **A. W. Maue**, Toward formulation of a general diffraction problem via an integral equation, in **E. K. Miller, L. Medgyesi-Mitschang, and E. H. Newman** (eds.), *Computational Electromagnetics, Frequency-Domain Method of Moments*, pp. 7–14, IEEE Press, New York, USA, 1992, article appeared earlier in *Zeitschrift für Physik* (in German), vol 126, 1949.

[59] **A. F. Peterson, C. F. Smith, and R. Mittra**, Eigenvalues of the moment-method matrix and their effect on the convergence of the conjugate gradient algorithm, *IEEE Trans. Antennas and Propagation*, vol. 36, no. 8, pp. 1177–1179, Aug. 1988.

[60] **L. Marin**, Natural mode representation of transient scattered fields, *IEEE Trans. Antennas Propagat.*, vol. AP-21, no. 6, pp. 809–818, Nov. 1973.

[61] **A. D. Yaghjian**, Augmented electric- and magnetic-field integral equations, *Radio Science*, vol. 16, no. 6, pp. 987–1001, Nov.-Dec. 1981.

[62] **A. F. Peterson**, The ”interior resonance” problem associated with surface integral equations of electromagnetics: Numerical consequences and a survey of remedies, *Electromagnetics*, vol. 10, no. 3, pp. 293–312, 1990.

[63] **J. R. Mautz and R. F. Harrington**, H-field, E-field, and combined field solutions for bodies of revolution, Tech. Rep. TR-77-2, Dep. of Electrical and Computer Eng., Syracuse University, Syracuse, New York, USA, Feb. 1977.

[64] **W. C. Chew, J.-M. Jin, E. Michielssen, and J. Song (eds.)**, *Fast and Efficient Algorithms in Computational Electromagnetics*, Artech House, Norwood, MA, 2001.

[65] **J. R. Mautz and R. F. Harrington**, A combined-source formulation for radiation and scattering from a perfectly conducting body, *IEEE Trans. Antennas Propagat.*, vol. AP-27, no. 7, pp. 445–454, July 1979.

[66] **M. B. Woodworth and A. D. Yaghjian**, Multiwavelength three-dimensional scattering with dual-surface integral equations, *Journal of the Optical Society of America A*, vol. 11, no. 4, pp. 1399–1413, April 1994.

[67] **D. G. Dudley**, Error minimization and convergence in numerical methods, *Electromagnetics*, vol. 15, no. 1, pp. 89–97, Jan.-Feb. 1985.

[68] **R. F. Harrington**, Origin and development of the method of moments for field computation, in **E. K. Miller, L. Medgyesi-Mitschang, and E. H. Newman** (eds.), *Computational Electromagnetics, Frequency-Domain Method of Moments*, pp. 43–47, IEEE Press, New York, USA, 1992.

[69] **V. H. Rumsey**, Reaction concept in electromagnetic theory, in **E. K. Miller, L. Medgyesi-Mitschang, and E. H. Newman** (eds.), *Computational Electromagnetics, Frequency-Domain Method of Moments*, pp. 15–23, IEEE Press, New York, USA, 1992, article appeared earlier in *The Physical Review*, no. 6, 1954.

[70] **S. Wandzura**, Optimality of Galerkin method for scattering computations, *Microwave and Optical Technology Letters*, vol. 4, no. 5, pp. 199–200, April 1991.

[71] **K. F. Warnick and W. C. Chew**, On the spectrum of the electric field integral equation and the convergence of the moment method, *Int. J. Numer. Meth. Engineering*, vol. 51, pp. 31–56, 2001.

[72] **A. F. Peterson, D. R. Wilton, and R. E. Jorgenson**, Variational nature of galerkin and non-galerkin moment method solutions, *IEEE Trans. Antennas and Propagation*, vol. 44, no. 4, pp. 500–503, April 1996.

[73] **T. K. Sarkar, A. R. Djordević, and E. Arvas**, On the choice of expansion and weighting functions in the numerical solution of operator equations, *IEEE Trans. Antennas Propagat.*, vol. AP-33, no. 9, pp. 988–996, Sep. 1985.

[74] **A. F. Peterson**, Accuracy of currents produced by the locally-corrected Nyström method and the method of moments when used with higher-order representations, *Applied Computational Electromagnetics Society (ACES) Journal*, vol. 17, no. 1, pp. 74–83, Mar. 2002.

[75] **L. Gürel, K. Sertel, and I. K. Şendur**, On the choice of basis functions to model surface electric current densities in computational electromagnetics, *Radio Science*, vol. 34, no. 6, pp. 1373–1387, Nov.-Dec. 1999.

[76] **M. I. Aksun and R. Mittra**, Choices of expansion and testing functions for the method of moments applied to a class of electromagnetic problems, *IEEE Trans. om Microwave Theory and Techniques*, vol. 41, no. 3, pp. 503–509, Mar. 1993.

[77] **L. F. Canino, J. J. Ottusch, M. A. Stalzer, J. L. Visher, and S. M. Wandzura**, Numerical solution of the Helmholtz equation in 2D and 3D using a high-order Nyström discretization, *Journal of Computational Physics*, vol. 146, no. 2, pp. 627–663, 1998.

[78] **R. Kress**, Numerical solution of boundary integral equations in time-harmonic electromagnetic scattering, *Electromagnetics*, vol. 10, no. 1, pp. 1–20, Jan.-Feb. 1990.

[79] **J. J. Ottusch, J. L. Visher, and S. M. Wandzura**, Fast, high-order scattering code for solving practical RCS problems, *16th Annual Review of Progress in Applied Computational Electromagnetics (ACES 2000)*, vol. 2, pp. 867–873, Monterey, CA, USA, March 2000.

[80] **S. D. Gedney**, High-order method-of-moments solution of the scattering by three-dimensional PEC bodies using quadrature-based point matching, *Microwave and Optical Technology Letters*, vol. 29, no. 5, pp. 303–309, June 2001.

[81] **S. D. Gedney and C. Lu**, High-order integral equation solution based on a hybrid volume/surface formulation, *Proceedings of the 19th Annual Review of Progress in Applied Computational Electromagnetics*, pp. 328–333, Monterey, CA, USA, March 2003.

[82] **C. Klein and R. Mittra**, Stability of matrix equations arising in electromagnetics, *IEEE Trans. Antennas Propagat.*, vol. AP-21, no. 6, pp. 902–905, Nov. 1973.

[83] **L. S. Andersen and J. L. Volakis**, Development and application of a novel class of hierarchical tangential vector finite elements for electromagnetics, *IEEE Trans. Antennas Propagat.*, vol. 47, no. 1, pp. 112–120, Jan. 1999.

[84] **B. M. Notaroš**, personal communications, June 2002.

[85] **G. Kang, J. Song, W. C. Chew, K. C. Donepudi, and J.-M. Jin**, A novel grid-robust higher order basis function for the method of moments, *IEEE Trans. Antennas Propagat.*, vol. 49, no. 6, pp. 908–915, June 2001.

[86] **J. P. Webb**, Hierarchical vector basis functions of arbitrary order for triangular and tetrahedral finite elements, *IEEE Trans. Antennas Propagat.*, vol. 47, no. 8, pp. 1244–1253, Aug. 1999.

[87] **M. I. Sancer, R. L. McClary, and K. J. Glover**, Electromagnetic computation using parametric geometry, *Electromagnetics*, vol. 10, pp. 85–103, Jan.-June 1990.

[88] **G. E. Antilla and N. G. Alexopoulos**, Scattering from complex three-dimensional geometries by a curvilinear hybrid finite-element-integral equation approach, *Jour. Opt. Soc. Am. A*, vol. 11, no. 4, pp. 1445–1457, April 1994.

[89] **J. M. Song and W. C. Chew**, Moment method solutions using parametric geometry, *Jour. of Electromagnetic Waves Appl.*, vol. 9, pp. 71–83, 1995.

[90] **R. D. Graglia**, The use of parametric elements in the moment method solution of static and dynamic volume integral equations, *IEEE Trans. Antennas Propagat.*, vol. 36, no. 5, pp. 636–646, May 1988.

[91] **L. Valle, F. Rivas, and M. F. Cátedra**, Combining the moment method with geometrical modelling by NURBS surfaces and Bézier patches, *IEEE Trans. Antennas Propagat.*, vol. 42, no. 3, pp. 373–381, Mar. 1994.

[92] **J. Van Bladel**, *Electromagnetic Fields*, McGraw-Hill, New York, USA, 1964.

[93] **M. G. Duffy**, Quadrature over a pyramid or cube of integrands with a singularity at a vertex, *SIAM J. Numer. Anal.*, vol. 19, no. 6, pp. 1260–1262, Dec. 1982.

[94] **K. Sertel and J. L. Volakis**, Method of moments solution of volume integral equations using parametric geometry, *Radio Science*, vol. 37, no. 1, pp. 1–7, Jan.-Feb. 2002.

[95] **K. C. Donepudi, J.-M. Jin, S. Velamparambil, J. Song, and W. C. Chew**, A higher order parallelized multilevel fast multipole algorithm for 3-D scattering, *IEEE Trans. Antennas Propagat.*, vol. 49, no. 7, pp. 1069–1078, July 2001.

[96] **J. E. Hansen (ed.)**, *Spherical Near-Field Measurements*, Peter Peregrinus Ltd., London, 1988.

[97] **Y. Saad and M. H. Schultz**, GMRES: a generalized minimal residual algorithm for solving nonsymmetric linear systems, *SIAM Journal on Scientific and Statistical Computing*, vol. 7, no. 3, pp. 856–69, 1986.

[98] **P. Sonneveld**, CGS, a fast Lanczos-type solver for nonsymmetric linear systems, *SIAM Journal on Scientific and Statistical Computing*, vol. 10, no. 1, pp. 36–52, 1989.

[99] **H. A. Van Der Vorst**, Bi-CGSTAB: A fast and smoothly converging variant of Bi-CG for the solution of nonsymmetric linear systems, *SIAM Journal on Scientific and Statistical Computing*, vol. 13, no. 2, pp. 631–644, 1992.

[100] **R. W. Freund**, A transpose-free quasi-minimal residual algorithm for non-Hermitian linear systems, *SIAM Journal on Scientific Computing*, vol. 14, no. 2, pp. 470–482, 1993.

[101] **A. I. Nosich**, The method of analytical regularization in wave-scattering and eigenvalue problems: Foundations and review of solutions, *IEEE Antennas Propagat. Magazine*, vol. 41, no. 3, pp. 34–49, June 1999.

[102] **R. J. Adams and G. S. Brown**, Stabilisation procedure for electric field integral equation, *Electron. Letters*, vol. 35, no. 23, pp. 2015–2016, Nov. 1999.

[103] **H. Contopanagos, B. Dembart, M. Epton, J. J. Ottusch, V. Rokhlin, J. L. Visher, and S. M. Wandzura**, Well-conditioned boundary integral equations for three-dimensional electromagnetic scattering, *IEEE Trans. Antennas Propagat.*, vol. 50, no. 12, pp. 1824–1830, Dec. 2002.

[104] **D. B. Davidson and D. A. McNamara**, Comparisons of the application of various conjugate-gradient algorithms to electromagnetic radiation from conducting bodies of revolution, *Microwave and Optical Technology Letters*, vol. 1, no. 7, pp. 243–246, Sep. 1988.

[105] **G. Bürger, H.-D. Brüns, and H. Singer**, Advanced method of moments based on iterative equation system solvers, *IEEE Int. Symp. on Electromagnetic Compatibility*, pp. 236–241, Aug. 1997.

[106] **J. von Hagen and W. Wiesbeck**, Physics-based preconditioner for iterative algorithms in multi-scatterer and multi-boundary method of moments formulations, *Int. J. Numer. Meth. Engineering*, vol. 54, no. 3, pp. 317–329, 2002.

[107] —, Physics-based preconditioner for iterative algorithms in MoM-problems, *IEEE Trans. Antennas Propagat.*, vol. 50, no. 9, pp. 1315–1316, Sep. 2002.

[108] **J.-R. Poirier, P. Borderies, R. Mittra, and V. Varadarajan**, Numerically efficient solution of dense linear system of equations arising in a class of electromagnetic scattering problems, *IEEE Trans. Antennas and Propagation*, vol. 46, no. 8, pp. 1169–1175, Aug. 1998.

[109] **M. R. Pino, F. Obelleiro, J. L. Rodriguez, and R. J. Burkholder**, A multiblock generalized forward-backward method, *Radio Science*, vol. 36, no. 1, pp. 19–29, Jan.-Feb. 2001.

[110] **A. D. Yaghjian**, Banded-matrix preconditioning for electric-field integral equations, *1997 IEEE Antennas Propagat. Soc. Int. Symp.*, vol. 3, pp. 1806–1809, July 1997.

[111] **Y. Xie, J. He, A. Sullivan, and L. Carin**, A simple preconditioner for electric-field integral equations, *Microwave and Optical Technology Letters*, vol. 30, no. 1, pp. 51–54, July 2001.

[112] **A. H. Heldring, J. M. Rius, and L. Ligthart**, New block ILU preconditioner scheme for numerical analysis of very large electromagnetic problems, *IEEE Trans. Magnetics*, vol. 38, no. 2, pp. 337–340, March 2002.

[113] **V. V. S. Prakash and R. Mittra**, Multi-frontal preconditioners for iterative solvers, *2001 IEEE Antennas Propagat. Soc. Int. Symp.*, vol. 3, pp. 12–15, Boston, MA, USA, July 2001.

[114] —, An efficient technique for the iterative solution of lerge dense matrices arising in the method of moments simulation of MMIC problems, *2002 MTT-S Int. Microwave Symp. Digest*, vol. 3, pp. 2041–2044, June 2002.

[115] **K. Sertel and J. L. Volakis**, Incomplete LU preconditioner for FMM implementation, *Microwave and Opt. Tech. Letters*, vol. 26, no. 4, pp. 265–267, Aug. 2000.

[116] **M. Brüning, P. Benner, A. Bunse-Gerstner, R. Bunger, J. Reiter, and J. Ritter**, A sparse approximate inverse preconditioner for the method of moments accelerated with the multilevel fast multipole method, *Proc. of the 2002 IEEE Antennas Propagat. Soc. Int. Symp.*, vol. 2, pp. 602–605, San Antonio, TX, June 2002.

[117] **J. Rahola**, Iterative solution of dense linear systems in electromagnetic scattering calculations, *14th Annual Review of Progress in Applied Computational Electromagnetics (ACES 1998)*, vol. 2, pp. 1126–1123, Monterey, CA, USA, March 1998.

[118] **G. Alléon, M. Benzi, and L. Giraud**, Sparse approximate inverse preconditioning for dense linear systems arising in computational electromagnetics, *Numerical Algorithms*, vol. 16, no. 1, pp. 1–15, 1997.

[119] **J. Zhang, J. Lee, and C.-C. Lu**, Robust preconditioning techniques for electromagnetic wave scattering problems, *Proceedings of the 19th Annual Review of Progress in Applied Computational Electromagnetics*, pp. 347–350, Monterey, CA, USA, March 2003.

[120] **F. X. Canning and J. F. Scholl**, Diagonal preconditioners for the EFIE using a wavelet basis, *IEEE Trans. Antennas Propagat.*, vol. 44, no. 9, pp. 1239–1246, Sep. 1996.

[121] **H. Deng and H. Ling**, An efficient preconditioner for electromagnetic integral equations using predefined wavelet packet basis, *IEEE Trans. Antennas Propagat.*, vol. 50, no. 11, pp. 1633–1640, Nov. 2002.

[122] **E. P. Stephan and T. Tran**, Domain decomposition algorithms for indefinite hypersingular integral equations: The h and p versions, *SIAM J. Sci. Comput.*, vol. 19, no. 4, pp. 1139–1153, July 1998.

[123] **N. Heuer**, Additive Schwarz method for the p-version of the boundary element method for the single layer potential operator on a plane screen, *Numerische Mathematik*, vol. 88, pp. 485–511, 2001.

[124] —, Schwarz method for systems of boundary integral equations, *Appl. Num. Math.*, vol. 33, pp. 447–453, 2000.

[125] **J. L. Volakis and M. I. Sancer**, personal communications, Dec. 2001.

[126] **R. Dyczij-Edlinger and O. Biro**, A joint vector and scalar potential formulation for driven high frequency problems using hybrid edge and nodal finite elements, *IEEE Trans. om Microwave Theory and Techniques*, vol. 44, no. 1, pp. 15–23, Jan. 1996.

[127] **J. Gopalakrishnan and J. E. Pasciak**, Overlapping Schwarz preconditioners for indefinite time harmonic Maxwell equations, *Mathematics of Computation*, vol. 72, no. 241, pp. 1–16, 2003.

[128] **E. Anderson, Z. Bai, C. Bischof, S. Blackford, J. Demmel, J. Dongarra, J. Du Croz, A. Greenbaum, S. Hammarling, A. McKenney, and D. Sorensen**, *LAPACK Users' Guide*, SIAM, Philadelphia, PA, USA, 3rd edn., 1999, available at http://www.netlib.org/lapack.

[129] **M. D. Pocock and S. P. Walker**, The complex bi-conjugate gradient solver applied to large electromagnetic scattering problems, computational costs, and cost scalings, *IEEE Trans. Antennas Propagat.*, vol. 45, no. 1, pp. 140–146, Jan. 1997.

[130] **J. H. Richmond**, On the edge mode in the theory of TM scattering by a strip or strip grating, *IEEE Trans. Antennas Propagat.*, vol. AP-28, no. 6, pp. 883–887, Nov. 1980.

[131] **D. I. Kaklamani and N. K. Uzunoglu**, Scattering from a conductive rectangular plate covered by a thick dielectric layer and excited from a dipole source or a plane wave, *IEEE Trans. Antennas and Propagation*, vol. 42, no. 8, pp. 1065–1076, Aug. 1994.

[132] **W. J. Brown and D. R. Wilton**, Singular basis functions and curvilinear triangles in the solution of the electric field integral equation, *IEEE Trans. Antennas Propagat.*, vol. 47, no. 2, pp. 347–353, Feb. 1999.

[133] **P. Ya. Ufimtsev, B. Khayatian, and Y. Rahmat-Samii**, Singular edge behavior: To impose or not impose - that is the question, *Microwave and Optical Technology Letters*, vol. 24, no. 4, pp. 218–223, Feb. 2000.

[134] **G. Benelli**, *Higher Order Expansion Functions for Two Dimensional Scatterers with Edges*, Master's thesis, Ørsted-DTU, Technical University of Denmark, Lyngby, Denmark, Sep. 2002.

[135] **J. Meixner**, The behavior of electromagnetic fields at edges, *IEEE Trans. Antennas Propagat.*, vol. AP-20, no. 4, pp. 442–446, July 1972.

[136] **J. J. Bowman, T. B. A. Senior, and P. L. E. Uslenghi** (eds.), *Electromagnetic and Acoustic Scattering by Simple Shapes*, North-Holland Pub. Co., Amsterdam, The Netherlands, 1969.

[137] **G. A. Thiele and T. H. Newhouse**, A hybrid technique for combining the moment methods with a geometrical theory of diffraction, *IEEE Trans. Antennas Propagat.*, vol. AP-23, no. 1, pp. 62–69, Jan. 1975.

[138] **G. A. Thiele**, Overview of selected hybrid methods in radiating system analysis, *Proceedings of the IEEE*, vol. 80, no. 1, pp. 66–78, Jan. 1992.

[139] **D. P. Bouche, F. A. Molinet, and R. Mittra**, Asymptotic and hybrid techniques for electromagnetic scattering, *Proceedings of the IEEE*, vol. 81, no. 12, pp. 1658–1684, Dec. 1993.

[140] **L. N. Medgyesi-Mitschang and J. M. Putman**, Hybrid formulation for arbitrary 3-D bodies, *10th Annual Review of Progress in Applied Computational Electromagnetics (ACES 1994)*, vol. 2, pp. 267–274, Monterey, CA, USA, March 1994.

[141] **R. E. Hodges and Y. Rahmat-Samii**, An iterative current-based hybrid method for complex structures, *IEEE Trans. Antennas Propagat.*, vol. 45, no. 2, pp. 265–276, Feb. 1997.

[142] **M. Kaye, P. K. Murthy, and G. A. Thiele**, An iterative method for solving scattering problems, *IEEE Trans. Antennas Propagat.*, vol. AP-33, no. 11, pp. 1272–1279, Nov. 1985.

[143] **P. K. Murthy, K. C. Hill, and G. A. Thiele**, A hybrid-iterative method for scattering problems, *IEEE Trans. Antennas Propagat.*, vol. AP-34, no. 10, pp. 1173–1180, Oct. 1986.

[144] **J. M. Taboada and F. Obelleiro**, Including multibounce effects in the moment-method physical-optics (MMPO) method, *Microwave and Optical Technology Letters*, vol. 33, no. 6, pp. 435–439, March 2002.

[145] **M. A. Abdel Moneum, Z. Shen, J. L. Volakis, and O. Graham**, Hybrid PO-MoM analysis of large axi-symmetric radomes, *IEEE Trans. Antennas Propagat.*, vol. 49, no. 12, pp. 1657–1666, Dec. 2001.

[146] **Y. Shifman and Y. Leviatan**, Scattering by a groove in a conducting plane – a PO-MoM hybrid formulation and wavelet analysis, *IEEE Trans. Antennas Propagat.*, vol. 49, no. 12, pp. 1807–1811, Dec. 2001.

[147] **D.-H. Han, A. C. Polycarpou, and C. A. Balanis**, Hybrid analysis of reflector antennas including higher order interactions and blockage effects, *IEEE Trans. Antennas Propagat.*, vol. 50, no. 11, pp. 1514–1524, Nov. 2002.

[148] **C. Pochini, G. Toso, G. Pelosi, and A. Roederer**, A comparison between two hybrid techniques for the scattering from finite frequency-selective sufaces, *Microwave and Optical Technology Letters*, vol. 31, no. 4, pp. 248–252, Nov. 2001.

[149] **D. Kwon, R. J. Burkholder, and P. H. Pathak**, Efficient method of moments formulation for large PEC scattering problems using asymptotic phasefront extraction (APE), *IEEE Trans. Antennas Propagat.*, vol. 49, no. 4, pp. 583–591, April 2001.

[150] **F. Obelleiro, J. M. Taboada, J. L. Rodríguez, J. O. Rubiños, and A. M. Arias**, Hybrid moment-method physical optics formulation for modeling the electromagnetic behavior of on-board antennas, *Microwave and Opt. Tech. Letters*, vol. 27, no. 2, pp. 88–93, Oct. 2000.

[151] **F. Obelleiro, J. M. Taboada, J. L. Rodríguez, and J. M. Bértolo**, HEMCUVI: A software package for the electromagnetic analysis and design of radiating systems on board real platforms, *IEEE Antennas and Propagation Magazine*, vol. 44, no. 5, pp. 44–61, Oct. 2002.

[152] **U. Jakobus**, Extension of the MoM/PO hybrid method to homogeneous dielectric bodies, *Proceedings of the 14th Annual Review of Progress in Applied Computational Electromagnetics*, vol. 2, pp. 920–927, Mar. 1998.

[153] **U. Jakobus, A. Buchau, and F. M. Landstorfer**, Extending a MoM/PO/UTD hybrid method by an automatic selection of the computational methods based on neural networks, *Proceedings of the 15th Annual Review of Progress in Applied Computational Electromagnetics*, vol. 1, pp. 455–462, Mar. 1999.

[154] **J. M. Taboada, F. Obelleiro, and J. L. Rodríguez**, Improvement of the hybrid moment method - physical optics method through a novel evaluation of the physical optics operator, *Microwave and Opt. Tech. Letters*, vol. 30, no. 5, pp. 357–363, Sep. 2001.

[155] **GRASP8 General Relector Analysis Program**, TICRA, Læderstræde 34, Copenhagen, Denmark.

[156] **T. B. A. Senior and J. L. Volakis**, *Approximate Boundary Conditions in Electromagnetics*, The Institution of Electrical Engineers, London, UK, 1995.

[157] **A. G. P. Boswell and D. C. Brewster**, Some electrical properties of CFRP reflector antennas, *Fourth International Conference on Antennas and Propagation, ICAP 85*, pp. 358–361, Coventry, UK, April 1985.

[158] **K. A. Michalski and D. Zheng**, Electromagnetic scattering and radiation by surfaces of arbitrary shape in layered media, *IEEE Trans. Antennas Propagat.*, vol. 38, no. 3, pp. 335–344, March 1990.

[159] **B. D. Popović and D. Ž. Djurdjević**, Entire-domain analysis of thin-wire antennas near or in lossy ground, *IEE Proceedings, Microw. Antennas and Propag.*, vol. 142, no. 3, pp. 213–219, June 1995.

[160] **N. Geng, A. Sullivan, and L. Carin**, Multilevel fast-multipole algorithm for scattering from conducting targets above or embedded in a lossy half space, *IEEE Trans. Geoscience and Remote Sensing*, vol. 38, no. 7, pp. 1561–1573, July 2000.

[161] —, Fast multipole method for scattering from an arbitrary PEC target above or buried in a lossy half space, *IEEE Trans. Antennas Propagat.*, vol. 49, no. 5, pp. 740–748, May 2001.

[162] **K. C. Donepudi, J. Song, J. M. Jin, G. Kang, and W. C. Chew**, A novel implementation of multilevel fast multipole algorithm for higher-order Galerkin's method, *IEEE Trans. Antennas Propagat.*, vol. 48, no. 8, pp. 1192–1197, Aug. 2000.

[163] **J. A. Stratton**, *Electromagnetic Theory*, McGraw-Hill, New York, USA, 1941.

[164] **G. A. Korn and T. M. Korn**, *Mathematical Handbook for Scientists and Engineers*, McGraw-Hill, New York, USA, 2nd edn., 1968.

[165] **M. R. Spiegel**, *Mathematical Handbook of Formulas and Tables*, Schaum's Outline Series, McGraw-Hill, New York, USA, 1968.

[166] **M. Abramowitz and I. A. Stegun** (eds.), *Handbook of Mathematical Functions*, National Bureau of Standards, U.S. Government Printing Office, Washington D. C., USA, 3rd edn., 1965.

[167] **W. H. Press, S. A. Teukolsky, W. T. Vetterling, and B. P. Flannery**, *Numerical Recipies in Fortran 77*, Cambridge University Press, Cambridge, USA, 2nd edn., 1992.

[168] **P. J. Davis and P. Rabinowitz**, *Methods of Numerical Integration*, Academic Press, New York, USA, 1975.

[169] **J. Ma, V. Rokhlin, and S. Wandzura**, Generalized Gaussian quadrature rules for systems of arbitrary functions, *SIAM J. Numer. Anal.*, vol. 33, no. 3, pp. 971–996, June 1996.

[170] **J. S. Savage and A. F. Peterson**, Quadrature rules for numerical integration over triangles and tetrahedra, *IEEE Antennas and Propagation Magazine*, vol. 38, pp. 100–102, June 1996.

[171] **R. Barrett, M. Berry, T. F. Chan, J. Demmel, J. Donato, J. Dongarra, V. Eijkhout, R. Pozo, C. Romine, and H. Van der Vorst**, *Templates for the Solution of Linear Systems: Building Blocks for Iterative Methods*, SIAM, Philadelphia, USA, 2nd edn., 1994.

[172] **MSC software**, MSC.Patran, available at http://www.mscsoftware.com.

[173] **International Center for Numerical Methods in Engineering**, GiD, the personal pre and post processor, available at http://gid.cimne.upc.es.

[174] **E. K. Miller**, PCs for AP and other EM reflections, *IEEE Antennas Propagat. Magazine*, vol. 41, no. 3, pp. 83–88, June 1999.